

# **Two-Body and Three-Body Dynamics in Atom-Ion Experiments**

Dissertation

zur Erlangung des akademischen Grades  
Doktor der Naturwissenschaften (Dr. rer. nat.)

eingereicht an der  
Fakultät für Naturwissenschaften  
der  
Universität Ulm

von  
Arne Härter  
aus  
Göttingen

Betreuer der Dissertation: Johannes Hecker Denschlag

Februar 2013



Amtierender Dekan: Prof. Dr. Joachim Ankerhold  
Erstgutachter: Prof. Dr. Johannes Hecker Denschlag  
Zweitgutachter: Prof. Dr. Tommaso Calarco  
Tag der mündlichen Prüfung: 15. Mai 2013

Die in dieser Dissertation beschriebenen Arbeiten wurden durchgeführt an der

Universität Innsbruck  
Institut für Experimentalphysik  
Technikerstrasse 25  
A-6020 Innsbruck

und an der

Universität Ulm  
Institut für Quantenmaterie  
Albert-Einstein-Allee 45  
D-89069 Ulm



## Abstract

During the last few decades, the two fields of ultracold neutral atoms and of single trapped ions have undergone an amazing development. The incorporation of both these systems into a single experiment exploits the complementary physical properties of the subsystems and opens up novel lines of research.

In this thesis, I present experimental results obtained in one of the first hybrid atom-ion trap setups accessing the cold regime. Single  $^{138}\text{Ba}^+$ ,  $^{87}\text{Rb}^+$  or  $^{87}\text{Rb}_2^+$  ions are brought to interaction with ultracold thermal or Bose-condensed samples of  $^{87}\text{Rb}$  atoms. The collision energies are set by heating mechanisms in the Paul trap and typically are on the order of  $\text{mK}\cdot k_{\text{B}}$ . Due to the polarizing effect that the excess charge of the ion has on the atoms, interactions are generally strong and long-ranged. We observe elastic atom-ion scattering in the semi-classical energy regime in which the cross section depends on the collision energy and favors scattering at small angles. Making use of our control over the atomic samples we were able to obtain a general good understanding of atom-ion two-body collisions. We observed sympathetic cooling of the ion over four orders of magnitude in energy through collisions with the ultracold atoms. Further, we utilized atom-ion scattering events to develop a novel and effective method to compensate excess ion micromotion, the primary source of ion heating in our experiments.

Due to the long-range character of the interaction, three-body collisions between two atoms and the ion play an important role. We identified these processes through the large amounts of energy that they release. This makes them detectable despite their suppression with respect to two-body collisions. We also clearly showed that atom-atom-ion three-body collisions become more prominent as the collision energy decreases.

Finally, we employed our atom-ion apparatus to gain novel insights into three-body recombination between ultracold atoms. In these experiments the ion trap acts as an extremely sensitive ion detector with essentially no background events. Through three-body recombination a  $\text{Rb}_2$  molecule is formed and can undergo resonance-enhanced multi-photon ionization by absorbing photons from a strong narrow-linewidth laser. By scanning the frequency of the ionization laser we obtained a molecular spectrum and identified the population of molecular levels with different vibrational, rotational, electronic and nuclear spin quantum numbers. This indicates that three-body recombination leads to a relatively broad distribution of final states.



## Zusammenfassung

In den letzten Jahrzehnten haben die zwei Forschungsfelder der ultrakalten neutralen Atome sowie der einzelnen gefangenen Ionen eine beeindruckende Entwicklung genommen. Die Zusammenführung dieser beiden Systeme in ein einziges Experiment nutzt die sich ergänzenden physikalischen Eigenschaften der Teilsysteme aus und eröffnet Möglichkeiten für neuartige Forschung.

Die in dieser Arbeit vorgestellten Ergebnisse wurden an einer der ersten das kalte Regime erreichenden hybriden Atom-Ionen Fallen erzielt. Einzelne  $^{138}\text{Ba}^+$ ,  $^{87}\text{Rb}^+$  oder  $^{87}\text{Rb}_2^+$  Ionen werden mit ultrakalten thermischen oder Bose-kondensierten  $^{87}\text{Rb}$  Atomen zur Wechselwirkung gebracht. Die Kollisionsenergien werden durch Heizmechanismen in der Paulfalle bestimmt und liegen typischerweise im Bereich von  $\text{mK}\cdot k_{\text{B}}$ . Aufgrund des polarisierenden Effekts, den die überschüssige Ladung des Ions auf die Atome ausübt, sind die Wechselwirkungen im Allgemeinen stark und langreichweitig. Wir beobachten elastische Atom-Ionen Streuung im semi-klassischen Energie-Regime, in welchem der Wechselwirkungsquerschnitt von der Kollisionsenergie abhängt und Streuung unter kleinen Winkeln bevorzugt. Indem wir unsere Kontrolle über die atomaren Proben nutzten, waren wir in der Lage uns ein gutes allgemeines Verständnis der Atom-Ionen Zweikörper-Stöße zu erarbeiten. Wir beobachteten sympathethische Kühlung des Ions über vier Größenordnungen in Energie durch Stöße mit den ultrakalten Atomen. Außerdem nutzten wir Atom-Ionen Streuereignisse, um eine neuartige und effektive Methode zu entwickeln, um Mikrobewegung, die Hauptursache für das Heizen des Ions in unseren Experimenten, zu kompensieren.

Aufgrund der langreichweiten Wechselwirkung spielen Dreikörper-Stöße zwischen zwei Atomen und dem Ion eine wichtige Rolle. Wir identifizierten diese Prozesse durch die großen Mengen an Energie, die sie freisetzen. Dies macht sie messbar, obwohl sie im Vergleich zu Zweikörper-Stößen unterdrückt sind. Wir zeigten weiterhin deutlich, dass Atom-Atom-Ionen Dreikörper-Stöße zunehmen, wenn die Kollisionsenergie abnimmt.

Schließlich setzten wir unsere Atom-Ionen Apparatur ein, um neuartige Einsichten in Drei-Körper-Rekombination zwischen ultrakalten Atomen zu gewinnen. In diesen Experimenten fungiert die Ionenfalle als ein extrem empfindlicher Ionen-detektor, der im Grunde keine Hintergrundereignisse registriert. Durch Drei-Körper-Rekombination bildet sich ein  $\text{Rb}_2$  Molekül und kann resonant verstärkte Multiphotonen-Ionisation durchlaufen, indem es Photonen eines starken schmalbandigen Lasers

absorbiert. Durch Variieren der Frequenz des Ionisationslasers erhielten wir ein Molekülspektrum und identifizierten die Bevölkerung von molekularen Zuständen mit verschiedenen Quantenzahlen der Vibration, Rotation, sowie elektronischem Spin und Kernspin. Dies deutet darauf hin, dass Drei-Körper-Rekombination zu einer relativ breiten Verteilung der Endzustände führt.

# Contents

<b>1</b>	<b>Introduction</b>	<b>13</b>
1.1	The atom-ion interaction potential . . . . .	15
1.2	Experimental setting and implications . . . . .	19
1.2.1	Paul traps . . . . .	20
1.2.2	Atom traps . . . . .	22
1.3	Prospects of cold and ultracold atom-ion interactions . . . . .	24
1.3.1	Molecule formation in interstellar chemistry . . . . .	24
1.3.2	Feshbach control over elastic and inelastic atom-ion scattering	25
1.3.3	Charge transport at ultralow temperatures . . . . .	25
1.3.4	Strong coupling polarons . . . . .	26
1.3.5	Mesoscopic molecular ions . . . . .	27
1.3.6	Trap-induced atom-ion resonances and quantum information applications . . . . .	28
1.3.7	Mutual sensitive probing of atomic and ionic systems . . . . .	29
1.4	Overview of the thesis . . . . .	29
1.5	Publications . . . . .	30
<b>2</b>	<b>An apparatus for immersing trapped ions into an ultracold gas of neutral atoms</b>	<b>31</b>
2.1	Introduction . . . . .	32
2.2	The vacuum apparatus . . . . .	34
2.2.1	Lower section: BEC apparatus . . . . .	35
2.2.2	Upper section: Science chamber . . . . .	38
2.3	Ion trapping . . . . .	38
2.3.1	Linear Paul trap . . . . .	38
2.3.2	Loading and laser cooling of ions . . . . .	40
2.3.3	Micromotion . . . . .	42
2.3.4	Imaging methods . . . . .	43

2.4	Preparation and delivery of ultracold atomic samples . . . . .	43
2.4.1	MOT loading and magnetic trap . . . . .	44
2.4.2	Magnetic transport and QUIC trap . . . . .	44
2.4.3	Optical transport of ultracold atoms . . . . .	46
2.4.4	Adjusting the lattice transport distance . . . . .	49
2.4.5	Loading of the crossed dipole trap and evaporative cooling .	50
2.4.6	Fine alignment of the crossed dipole trap . . . . .	51
2.5	Summary . . . . .	52
<b>3</b>	<b>Dynamics of a cold trapped ion in a Bose-Einstein condensate</b>	<b>54</b>
3.1	Introduction . . . . .	54
3.2	Experimental setup . . . . .	56
3.3	Measurements of ion-induced atom loss . . . . .	58
3.4	Simple model to estimate the ion energy . . . . .	59
3.5	Inelastic processes . . . . .	61
3.6	The ion as a local density probe for atomic samples . . . . .	61
<b>4</b>	<b>Improved view on atom-ion dynamics and atom-based compensation of ion micromotion</b>	<b>64</b>
4.1	Improved model of ion micromotion . . . . .	65
4.2	The differential atom-ion interaction cross section . . . . .	69
4.3	Simulation of ion dynamics in an atom cloud . . . . .	71
4.3.1	Simulation of the ion energy evolution . . . . .	73
4.3.2	Simulation of the effect on the atomic sample . . . . .	75
4.4	Excess micromotion compensation measurements . . . . .	79
4.4.1	Compensation of radial excess micromotion . . . . .	81
4.4.2	Compensation of axial micromotion . . . . .	85
4.4.3	Comparison with established compensation methods . . . . .	87
4.5	Long-term drifts of compensation voltages . . . . .	90
4.6	The role of inherent micromotion in atom-ion interactions . . . . .	94
<b>5</b>	<b>Single Ion as a Three-Body Reaction Center in an Ultracold Atomic Gas</b>	<b>96</b>
5.1	Introduction . . . . .	97
5.2	Experimental Setup . . . . .	97
5.3	Evidence for Atom-Ion Three-Body Interaction . . . . .	98
5.4	Direct Measurement of the Energy released in the Recombination Events	102

5.5	Measurement of the Energy Dependence of the Three-Body Coefficient	105
5.6	Supplemental Material . . . . .	106
<b>6</b>	<b>Shedding Light on Three-Body Recombination in an Ultracold Atomic Gas</b>	<b>110</b>
6.1	Introduction . . . . .	111
6.2	Experimental scheme . . . . .	113
6.3	Dependence of the ion production on atomic density, laser frequency and laser intensity . . . . .	114
6.3.1	Density dependence . . . . .	114
6.3.2	Dependence on laser frequency - REMPI spectrum . . . . .	114
6.3.3	Dependence on laser intensity . . . . .	117
6.4	Assignment of observed resonances to molecular transitions . . . . .	119
6.5	Conclusion . . . . .	122
6.6	Methods . . . . .	122
6.6.1	Dipole trap and REMPI configuration . . . . .	122
6.6.2	Paul trap configuration . . . . .	123
6.6.3	Ion detection methods . . . . .	123
6.7	Supplementary Information . . . . .	124
6.7.1	Ion detection method 1 . . . . .	124
6.7.2	Ion detection method 2 . . . . .	126
<b>7</b>	<b>Outlook</b>	<b>128</b>
7.1	Towards ultracold atom-ion experiments . . . . .	128
7.2	An optical dipole trap for Ba <sup>+</sup> ions and Rb atoms . . . . .	129
7.3	An ideal choice of species . . . . .	132



# Chapter 1

## Introduction

In the course of any scientific advancement, a profound understanding of the system under investigation is the first and most important step. Building upon this understanding, the system can then be controlled, expanded and used in novel and more complex contexts. Over the last decades, such a development has taken place in the trapping and manipulation of both charged and neutral atomic particles. Positively charged atomic ions confined in Paul traps had been investigated for more than 20 years until the preparation of single ions in the motional ground state of the trap was realized [1]. This control of the particles on the single quantum level has sparked a vibrant development of the field and facilitated the conception [2] and experimental realization of quantum gates [3], the construction of atomic clocks with unprecedented accuracy [4] and the successful application of trapped ion systems for quantum simulations [5]. In parallel to this progress in the control of charged particles, spectacular advances were achieved in the work on neutral atomic ensembles. A decisive step was made through the realization of Bose-Einstein condensation [6, 7], a striking and long-sought quantum many-body phenomenon. It took only a few years until control over the inter-particle interactions was gained [8] and Bose-Einstein condensates were used as starting points to implement tailored quantum systems [9] that are now on the way to become universal quantum simulators impacting condensed matter and even high energy physics.

In light of the similarity of the overlying theoretical goals and experimental challenges it seems surprising that the research lines on trapped ions and neutral atoms had been largely detached over decades. The two systems exhibit complementary experimental advantages. While ion trapping and imaging can readily be achieved on the single particle level, large ensembles of millions of atoms are routinely produced in standard lab setups. Through evaporative cooling methods they can therefore be cooled to

extremely low temperatures on the nK scale. The very tight and deep ion traps, on the other hand, enable preparation of ions in defined trap energy levels and allow for exceedingly long storage times reaching up to several weeks.

The scattering between atoms and ions was described classically by Paul Langevin more than 100 years ago [10]. However, the basis to understand the interactions well into the  $\mu$ K energy regime [11] was established using a semiclassical approach in the year 2000 by Robin Côté and coworkers. Further results from this group also showed possible applications of such systems for fundamental investigations of charge transport mechanisms [12] and novel mesoscopic quantum objects [13]. Experimental realizations of atom-ion setups were delayed due to the intimidating experimental challenges imposed mainly by the strong perturbations of the atomic cooling methods through the high-voltage radiofrequency (rf) fields required for ion trapping. In 2009, the group of Vladan Vuletić was the first to realize a combined magneto-optical and Paul trap [14]. They studied near-resonant charge transfer processes using different Yb isotopes and successfully described the respective cross section with a classical Langevin model. The collision energy was varied over three orders of magnitude with a lower bound of about  $k_B \cdot 35$  mK set by the difficulty of compensating ion excess micromotion. About a year later, full-fledged hybrid atom-ion setups featuring Rb Bose-Einstein condensates (BEC) interacting with single  $\text{Yb}^+$  [15],  $\text{Ba}^+$  and  $\text{Rb}^+$  ions [16] became operational. In the experiments with  $\text{Yb}^+$  ions performed by the group of Michael Köhl in Cambridge, sympathetic cooling of the ion through collisions with the atoms was shown. The experiments using  $\text{Ba}^+$  and  $\text{Rb}^+$  conducted in our group in Innsbruck provided a direct comparison of the cross sections of the two species. Very similar atom-ion collision rates were measured as could be expected in the semiclassical energy regime in which the internal structure of the collision partners has negligible effect. A further result of this work was the successful local probing of atomic density distributions using a single ion. Both the experiments in Innsbruck and Cambridge also investigated charge transfer processes and found them to be strongly suppressed for  $\text{Yb}^+$  as well as for  $\text{Ba}^+$  colliding with Rb. The experiments were limited in the atom-ion collision energies to roughly tens of mK due to the heating induced by excess micromotion. In the following, the effects of ion micromotion in an environment of an ultracold buffer gas were investigated in more detail and were found to give rise to rather involved ion dynamics [17]. The source of this dynamics is the interruption of the coherently driven micromotion through the collision with an atom at a random phase of the micromotion oscillation. This mechanism and the resulting importance of the atom-ion mass ratio was originally

discovered more than forty years ago by Major and Dehmelt [18]. It was further worked out by DeVoe in 2009 [19] and applied to the cold atom-ion systems by the Köhl group [20]. The improved model of atom-ion collision dynamics presented in ref. [17] also highlighted the relevance of glancing collisions and their signature in the evolution of the atomic sample.

A series of experiments was carried out by the groups in Basel [21, 22], Los Angeles [23, 24] and Cambridge [25] to investigate the dependence of charge transfer on the electronic states of the collision partners. These studies included reactions of atomic and molecular ions with atomic gases and have revealed rich dynamics which are not yet fully described within a theoretical model. The experiments from ref. [25] additionally demonstrated quenching of electronic excitations via atom-ion collisions.

During the last few years, the interest in cold atom-ion experiments has been increasing dynamically and more than a dozen groups are now active in this field (see Fig. 1.1). Several experiments are currently being set up targeting the usage of ultracold atomic samples with different combinations of atomic and ionic species (Schmidt-Kaler, Ozeri and Urabe groups). Interesting results can also be expected from collisions of cold atoms with polar diatomic molecules (Hudson) or a setup without an ion trap in which ions can drift freely through an ultracold gas (Raithel). These advances promise to broaden the scope of the research field and will further accelerate the general dynamics of atom-ion investigations.

## 1.1 The atom-ion interaction potential

The interaction between an atom and an ion is governed by the separation of charges induced in the atom through the electric field surrounding the ion. This polarization interaction is ubiquitous in nature and actually is observable on a macroscopic scale in everyday life, e.g. when a charged rod attracts scraps of paper or when electric fields produced in thunderstorms make human hair stand on end. A purely classical description is also sufficient to obtain a full qualitative understanding of the underlying physics even in the microscopic case. The electric field of the ion is essentially that of a point charge

$$E(r) = \frac{e}{4\pi\epsilon_0 r^2} \quad (1.1)$$

with  $e$  the elementary charge,  $\epsilon_0$  the vacuum permittivity and  $r$  the separation between atom and ion. This field induces a dipole moment  $p(r) = 4\pi\epsilon_0\alpha E(r)$  in the atom whose magnitude depends on the atomic polarizability  $\alpha$ . As a result, the

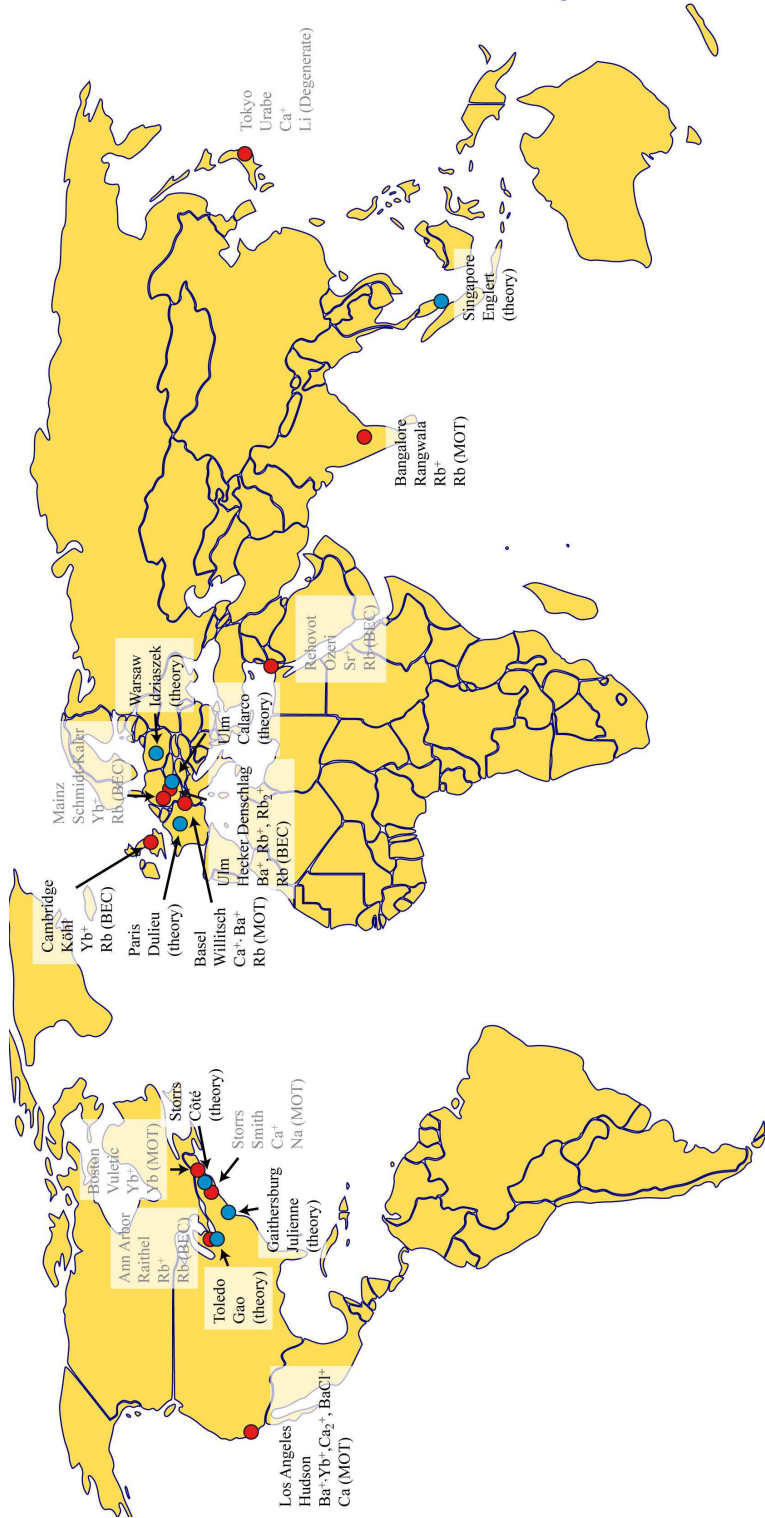


Figure 1.1: Overview of current research on cold atom-ion interactions. For the experimental groups (red dots) the ionic and atomic species are indicated. Grey text refers to experiments currently being set up or not operated anymore. Figure partly adapted from [26].

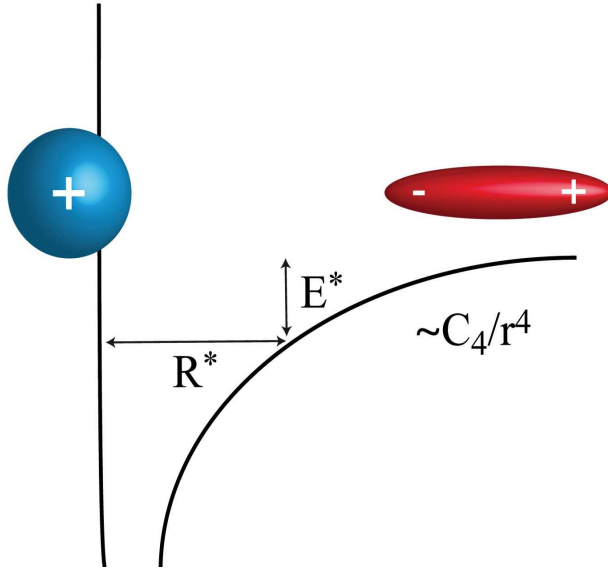


Figure 1.2: Illustration of the  $1/r^4$  polarization potential governing atom-ion interactions. The characteristic length scale  $R^*$  and energy scale  $E^*$  are indicated.

atom-ion interaction is described by the polarization potential

$$V(r) = -\frac{1}{2}p(r)E(r) = -\frac{C_4}{r^4} \quad (1.2)$$

with  $C_4 = \frac{\alpha e^2}{8\pi\epsilon_0}$  (see Fig. 1.2). It is convenient to define a typical length scale for the potential

$$R^* = \sqrt{\frac{\mu C_4}{\hbar^2}}, \quad (1.3)$$

where  $\mu$  is the reduced mass of the atom-ion system. At this separation of the particles we can assign a characteristic energy scale

$$E^* = \frac{\hbar^2}{2\mu R^{*2}}. \quad (1.4)$$

For the two atom-ion combinations most relevant to this work, we get  $R_{\text{BaRb}}^* = 295 \text{ nm}$ ,  $E_{\text{BaRb}}^* = 50 \text{ } k_{\text{B}} \cdot \text{nK}$  in the heteronuclear case ( $^{138}\text{Ba}^+$  and  $^{87}\text{Rb}$ ) and  $R_{\text{RbRb}}^* = 266 \text{ nm}$ ,  $E_{\text{RbRb}}^* = 80 \text{ } k_{\text{B}} \cdot \text{nK}$  in the homonuclear case.

The polarization potential exhibits a pronounced long-range character. A consequence of this fact is the contribution of many partial waves in atom-ion scattering even at collision energies in the  $\mu\text{K}$  regime. For the homonuclear case of  $\text{Rb}^+$  colliding with its parent atom we can directly compare atom-ion scattering to atom-atom

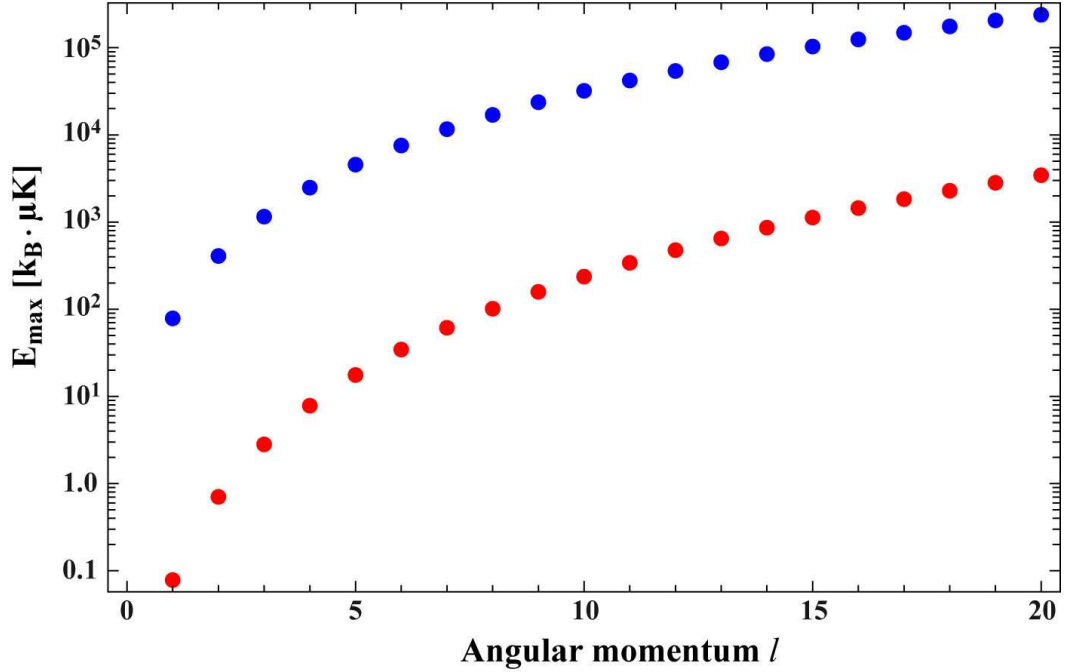


Figure 1.3: Height of the centrifugal barrier as a function of the angular momentum  $l$  for atom-atom (blue) and atom-ion scattering (red).

scattering between two neutral Rb atoms. To illustrate the differences we consider the height of the centrifugal barriers  $E_{\max}$  in both cases as a function of the angular momentum quantum number  $l$  (see Fig. 1.3). In atom-ion scattering, the values of  $E_{\max}$  are about three orders of magnitude lower than in neutral atom scattering. Thus, at typical collision energies attained in our experiments on the order of mK, more than ten partial waves will contribute to the scattering cross section.

The atom-ion scattering processes are well described using a semiclassical calculation as given in ref. [11]. An analytical expression for the elastic atom-ion scattering cross section  $\sigma_{\text{ai}}$  can be derived and written as

$$\sigma_{\text{ai}} \approx 5.08 \left( \frac{\mu C_4^2}{\hbar^2} \right)^{1/3} E_{\text{col}}^{-1/3}, \quad (1.5)$$

where  $E_{\text{col}}$  denotes the collision energy. Obviously, in contrast to s-wave scattering between ultracold neutrals, the atom-ion cross section in the relevant energy regime is energy-dependent and increases as the energy is decreased. At a collision energy of  $1 \text{ mK} \cdot k_{\text{B}}$ , we get a cross section of  $\sigma_{\text{ai}} \approx 2 \cdot 10^{-14} \text{ m}^2$ , a value roughly comparable to  $R_{\text{RbRb}}^{*2}$ . Compared to the s-wave cross section of two neutral Rb atoms we find  $\sigma_{\text{ai}}$  to be larger by about two orders of magnitude. It follows that atom-ion interactions

will typically be strong and three-body reactions involving the ion can be expected at moderate atomic densities. A further important consequence of the characteristics of atom-ion interactions is the preferred scattering in forward directions, in what is often termed glancing collisions. More details on the differential atom-ion cross section will be given in section 4.2 and can be found in refs. [27] and [20].

In addition to elastic collisions, atom-ion systems also allow for inelastic reactions in which the charge is transferred from the ion to the atom. This type of interaction usually requires a close encounter of the two nuclei and will not occur in a glancing collision. The charge transfer cross section  $\sigma_{ct}$  is thus generally significantly smaller than  $\sigma_{ai}$  and its scaling behavior can be estimated over a large energy range by the classical Langevin formula [10, 11]

$$\sigma_{ct} = \epsilon_{ct}\pi\sqrt{2C_4}E_{col}^{-1/2}, \quad (1.6)$$

where  $\epsilon_{ct}$  is the fraction of Langevin collisions resulting in charge transfer. For the case of  $\text{Ba}^+$  colliding with  $\text{Rb}$  at  $E_{col} = 1 \text{ mK}\cdot k_B$  we get  $\sigma_{ct}/\epsilon_{ct} \approx 4 \cdot 10^{-15} \text{ m}^2$ . In this atom-ion system, charge transfer is exothermic by about 1 eV and will predominantly take place via the emission of a photon. This radiative process is experimentally found to yield slow charge transfer with  $\epsilon_{ct} \approx 10^{-4}$  (see [16] and chapter 3) in agreement with theoretical predictions [28]. Resonant charge transfer occurs in the homonuclear case and is in principle indistinguishable from elastic scattering. We can thus expect  $\epsilon_{ct}^{\text{res}} = 1/2$ , in agreement with the observations from ref. [14].

## 1.2 Experimental setting and implications

The possibilities of a field of research depend crucially on the available technological means. Quantum optics has been continuously driven by the development and incorporation of improved lasers, optics and computer technology. Often enough, the technological development was done by scientific researchers themselves and was subsequently adopted into commercial products. The motivation, however, comes from challenges imposed by fundamental physical questions and successful laboratory setups usually rely on simple and thus reliable technological solutions.

In all current hybrid atom-ion traps the ions are confined by electric forces in Paul traps. The atoms, on the other hand, are trapped by magnetic or optical forces. The general goal is to attain flexible experimental conditions with as little technical restrictions as possible. I will give a brief account of the commonly employed trapping techniques and their ramifications for the exploration of atom-ion physics.

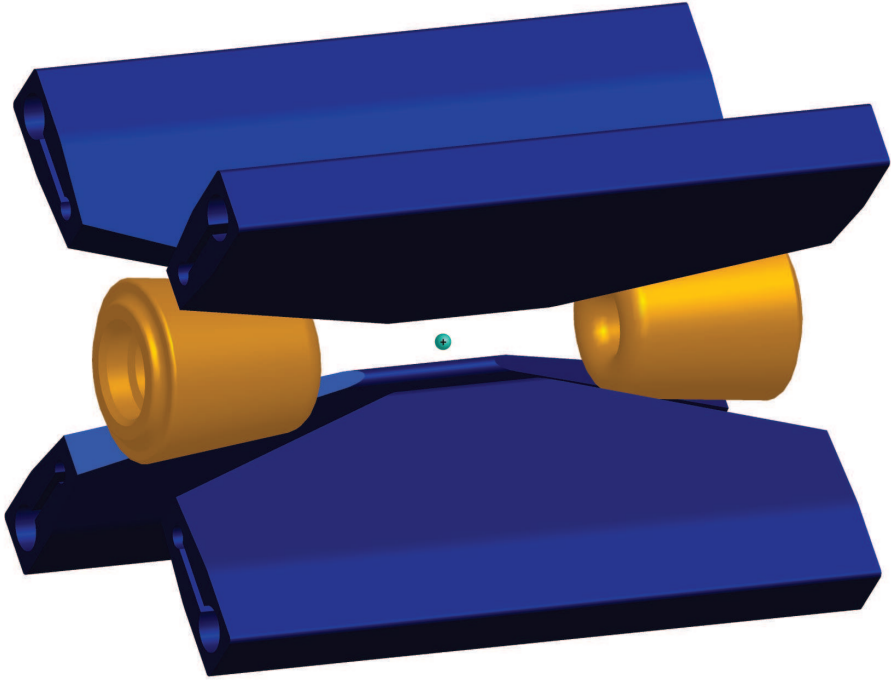


Figure 1.4: Linear Paul trap. Four radiofrequency electrodes (blue) create a radial confining potential while two endcap electrodes (gold) provide static axial confinement.

### 1.2.1 Paul traps

Ions are confined in Paul traps by a combination of oscillating and static electric fields (see, e.g. [29–31]). In the case of a linear Paul trap, as is used in our experiments, oscillating voltages on four rf electrodes establish a radial trapping potential (see Fig. 1.4). The remaining dimension is plugged by applying static voltages to two endcap electrodes. The effective potential generated in this way is essentially that of a three-dimensional harmonic oscillator with cylindrical symmetry. The attainable potential depths for atomic ions are typically on the order of electron volts so that ions far above room temperature can be easily contained. Another implication of the enormous trap depths are commonly reached storage times on the order of many days or even weeks. Experimentally, this is a huge advantage for the operation of atom-ion experiments as it offers the opportunity to work with one and the same ion for almost arbitrarily many production cycles of ultracold atom clouds. Further, the deep ion traps facilitate the investigation of atom-ion interactions over about six orders of magnitude in energy. This has proven especially useful in the observation of exothermic chemical reactions [17, 32]. Such processes may preferably take place at collision energies below 1 mK and release energies on the order of thousands of

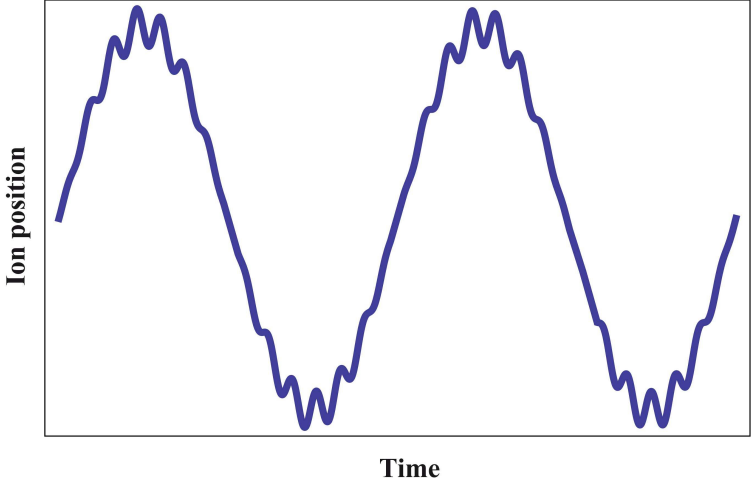


Figure 1.5: Illustration of a one-dimensional trajectory of an ion in a Paul trap. The slow secular oscillation is superposed with the fast micromotion.

Kelvin. A Paul trap of sufficient depth allows to contain these highly energetic particles and read out their final kinetic energy. In addition to their large depth, Paul trap potentials also feature high trapping frequencies of typically hundreds of kHz and correspondingly tight ionic confinement. As a result, ions can be placed into a well-defined region of an atomic sample and probe or manipulate atoms locally. High trapping frequencies also allow for rapid transport of ions with small heating effects [33]. Finally, Paul traps rely solely on the charge of the trapped particles and are thus almost independent of the species used. Geometrical considerations usually restrict the usage to a range of ionic masses spanning about one order of magnitude.

Despite the numerous convenient properties of Paul traps, they do entail some experimental issues in the context of atom-ion experiments. The most prominent challenges arise due to the presence of ion micromotion (see Fig. 1.5). This motion is driven by the radiofrequency supplying the electrodes of the trap and is commonly divided into inherent micromotion and excess micromotion. The inherent part is directly linked to the so-called secular motion of the ion in the effective potential of the Paul trap. Excess micromotion is generated by experimental imperfections that lead to a shift of the ion's position away from the trap center or to a difference in rf phase between the two pairs of rf electrodes. The success of the experiments performed on isolated ions in Paul traps has hinged on the decoupling of secular and excess micromotion degrees of freedom when performing laser cooling schemes. Thus, ions can be cooled into the ground state of the effective potential [34] while undergoing significant amounts of micromotion oscillations. Put in other words, laser

cooling addresses one mode of ionic motion while leaving the other mode almost untouched. The cooling of trapped ions by collisions with ultracold atoms relies on vastly different mechanisms. Let us suppose an ion collides head-on with an atom of equal mass initially at rest. This will extract the ion's kinetic energy and transfer it to the atom. However, the oscillating electric fields will quickly (in a time comparable to a micromotion oscillation period, typically in the nanosecond regime) reinstall an ion velocity determined by the position of the temporarily stopped ion. If the collision occurs close to the center of the trap, energy will be extracted from the secular mode and the ion is cooled. If the collision takes place close to the turning point of the secular oscillation, the interruption and almost immediate replenishment of the micromotion oscillation is equivalent to an increase of secular energy. The ion is heated although it was temporarily stopped. In a simple picture, this shows how ionic secular motion is connected to all degrees of micromotion as soon as collisional partners become available. Further discussion of the dynamics of a trapped ion in an ultracold buffer gas will be given in chapter 4 and can be found in [18–20]. The most important consequence of the described coupling between micromotion and secular motion is that the energy scale of the atom-ion experiments will be determined by the amount of ionic micromotion and will be ultimately limited through the specific trap setup and the atom-ion mass ratio [35]. For the combinations of atomic and ionic species relevant to this work, reaching collision energies below  $100 \mu\text{K}\cdot k_{\text{B}}$  in our Paul trap may not be possible. An experimentally favorable consequence of the coupling between micromotion and secular motion is the simple and precise tunability of the average collision energies via the adjustment of excess micromotion amplitudes, usually done by applying static electric fields.

### 1.2.2 Atom traps

Three different types of atom traps have been used in atom-ion experiments, namely magnetic, magneto-optical and optical dipole traps.

#### 1. Magnetic traps

Currently, only the Köhl group is performing atom-ion experiments using a magnetic trap. In principle, magnetic traps seem ideally suited for this task as they are typically highly stable, reliable and have only comparatively small impact on the ion. One drawback of these traps is the fact that they usually do not allow for a precise adjustment of magnetic offset fields. This may be detrimental for certain schemes in which ionic internal quantum states are

addressed. The main issue, however, arises from geometrical considerations. Typically both Paul traps and the coils required for magnetic trapping are of similar dimensions. It is therefore difficult to find a configuration that does not have significant downsides for one of the two trap setups. The Köhl group has coped with this issue by designing relatively large magnetic coils resulting in comparatively low atomic trapping frequencies making rf evaporation slow.

## 2. Magneto-optical traps (MOTs)

Several groups are running atom-ion setups which feature a MOT. Their main advantages are the simplicity of the setup and the possibility of continuous operation without the need to reproduce atomic samples within an experimental cycle. An important disadvantage is the usage of resonant laser radiation for trapping so that the atoms spend significant amounts of time in electronically excited levels. This opens up further chemical reaction channels which may often be undesirable. In addition, the attainable atomic densities in such setups are typically limited to about  $10^9 \text{ cm}^{-3}$ .

## 3. Optical dipole traps

Our setup and the one in the Köhl group can trap atoms in a far off-resonant optical dipole trap. In both cases, the atoms are precooled in magnetic traps to allow for optical trapping with manageable laser powers. In terms of experimental flexibility and compatibility with ion trapping, dipole traps seem an ideal choice. One issue can arise at high atomic densities where neutral molecules will form at considerable rates through three-body recombination. As is detailed in chapter 6 , the rich level structure of these molecules can lead to resonant interaction with the strong laser light needed for optical trapping. This can lead to unwanted ionization events. The wavelength of the dipole trap laser should thus be chosen carefully and broadband laser sources may be problematic.

In summary, while some compromises must be made, the general compatibility of atom and ion trapping is surprisingly good. There are little direct impacts of the atom traps on the ion or vice versa. Indirect effects like the complex collision dynamics in a Paul trap may not be solely negative as they also open up novel routes of research, e.g. the compensation of micromotion via interaction with ultracold atoms (see chapter 4).

## 1.3 Prospects of cold and ultracold atom-ion interactions

Experimental efforts including the work presented in this thesis are still aiming at deepening the general understanding of the hybrid atom-ion experiments at hand. The control over experimentally relevant parameters has not yet reached the level that is routinely available in ultracold neutral atomic systems or in ion trap setups. Nonetheless, the progress made so far is very encouraging and the increasing dynamics of the research field raises hopes that significant advancements will continue to be made. There are several intriguing goals that are driving researchers to work on the control of atom-ion systems. I will give a short overview of some of these prospects and discuss the possibilities for their experimental realization.

### 1.3.1 Molecule formation in interstellar chemistry

The chemistry in interstellar clouds is of significant fundamental interest to physicists and chemists alike. Specifically, it has been observed that molecules are formed under the dilute (density  $< 10^6 \text{ cm}^{-3}$ ) and cold (temperature  $\sim 10 \text{ K}$ ) conditions of interstellar clouds [36, 37]. A closer analysis shows that these molecule formation reactions proceed dominantly via interaction of positive ions with neutral atoms and molecules. As an example, hydrogen may be ionized by highly energetic cosmic radiation and then undergo a series of reactions with neutral partners to form closed-shell  $\text{H}_3\text{O}^+$ . This molecular ion then dissociatively recombines with a free electron and  $\text{H}_2\text{O}$  is formed. Laboratory data on such reactions has provided important information for the understanding of these processes and has enabled successful theoretical modelling [38]. Still, a number of questions are yet unanswered and require further investigations. Studying chemical reactions of the above type at sub-Kelvin temperatures can lead to new insights into the field because of the much higher degree of control. Endothermic reactions at these very low temperatures will be completely eliminated for most reactions of interest.

Our group along with the groups in Los Angeles, Basel and Cambridge have shown results on different chemical reactions in hybrid atom-ion setups. The measurements were performed between atomic or diatomic ions reacting with neutral atoms. It will be interesting to expand these investigations to reactions with more complex molecular collision partners.

### 1.3.2 Feshbach control over elastic and inelastic atom-ion scattering

While the semiclassical description of atom-ion collisions is well-suited for the experiments presented in this thesis, it is an important aspect of the polarization potential that pure s-wave scattering is achievable at temperatures that are attainable in ultracold atomic ensembles. A comprehensive overview over such ultracold atom-ion interactions is given in refs. [39] and [40]. In this regime, magnetic Feshbach resonances become relevant and allow for the tuning of the atom-ion interaction strength. Such control can then be exploited to realize systems with the desired properties for specific experimental tasks. In most atom-ion systems several Feshbach resonances appear at relatively low magnetic fields ( $< 100 \text{ G}$ ), a feature that can be traced back to the high density of bound states close to threshold in the atom-ion interaction potential. While this multitude of available resonances is experimentally encouraging, the very low collision energies required to reach the s-wave regime (typically  $\lesssim 100 \text{ nK} \cdot k_B$ ) make experimental investigations of Feshbach resonances in elastic atom-ion scattering seem distant.

It is interesting and promising for experimentalists that Feshbach resonances also occur in the radiative charge transfer processes that take place, e.g. in the  $\text{Ba}^+ \text{-Rb}$  system. In contrast to the case of elastic scattering, the resonances in the charge transfer cross section persist even at energies much higher than the s-wave threshold. In scattering of  $\text{Ba}^+$  and Rb, clear resonant signatures can thus be expected even at collision energies on the order of tens of  $\mu\text{K}$  [41]. A further reduction of the currently technically limited collision energies could therefore lead to the control of charge transport on the single particle level through the appropriate tuning of magnetic fields.

### 1.3.3 Charge transport at ultralow temperatures

In ref. [12] a transition in the charge transport mechanism is predicted in an ultracold gas doped with ionic impurities. At high temperatures charge transport occurs by collisions of the ions with their parent atoms as was briefly described in section 1.1. When the temperature is lowered to a few  $\mu\text{K}$ , the de Broglie wavelength of the particles increases and allows electrons which are bound to the atoms to delocalize over hundreds of nm. Further, the charge transfer radius  $r_{\text{ct}} = \sqrt{\sigma_{\text{ct}}/\pi}$  at these temperatures becomes much larger than the interatomic s-wave scattering length (ref. [12] performs calculations for the  $\text{Na}^+ \text{-Na}$  system, similar arguments also apply

to Rb). The gas can be viewed as frozen with negligible atomic motion on short enough timescales. However, due to the large charge transfer radius, electrons can hop from atoms to ions or, equivalently, positively charged holes can be transferred from ions to atoms. This results in a diffusion of charge through the ultracold gas and the system exhibits a drastic increase in the charge mobility when the temperature is reduced below the critical value necessary for the electron hopping conductivity. An experimental test of the proposed transition from an insulating to a conducting gas requires excellent control of external electric fields to allow for an effectively free diffusion of charge through the gas. Also, ion trapping would need to be switched off in at least one dimension and excellent spatially resolved ion detection is required. Depending on the density of the gas, transition temperatures between  $1 \mu\text{K}$  and tens of  $\mu\text{K}$  can be expected, about one to two orders of magnitude below the currently accessible temperature ranges. The realization of such a system would be a great testing ground for conductivity in solid state systems under well-defined conditions.

### 1.3.4 Strong coupling polarons

From solid state physics the concept of a polaron as a quasi-particle formed by an impurity interacting with its environment is well known (see, e.g., ref. [42]). Ultracold gases have recently received considerable attention in the context of polaron physics due to the excellent tunability of the relevant parameters. In degenerate Fermi gases, attractive [43] and repulsive [44, 45] polarons have been observed. Experimental realizations of such phenomena in BECs are missing but several theoretical studies are available [46–49]. Depending on the interaction strength between the impurity and its surrounding, it is useful to distinguish between weak, intermediate and strong coupling regimes. The latter case is of special interest as it leads to a localization of the impurity induced by its own polarizing effect on the bosonic gas. Following the notation from ref. [46] the key parameter is

$$\beta = \sqrt{\pi} \left( 1 + \frac{m_B}{m_I} \right) \left( 1 + \frac{m_I}{m_B} \right) \cdot \sqrt{n_{\text{at}} \frac{a_{IB}^4}{a_{BB}^4}}, \quad (1.7)$$

with  $m_B$  and  $m_I$  the boson and impurity masses,  $n_{\text{at}}$  the atomic density and  $a_{IB}$  and  $a_{BB}$  the impurity-boson and boson-boson scattering lengths. For  $\beta > 4.7$  the polaron coupling becomes so strong that self-localization occurs. The resulting bound state

is called the strong coupling or Fröhlich polaron. Its typical energy scale is given by

$$E_0 = 8\pi^2 \hbar^2 a_{IB}^4 n_{at}^2 \cdot \frac{(m_I + m_B)^4}{m_I^3 m_B^2}. \quad (1.8)$$

As an example, I will consider a  $\text{Ba}^+$  ion in a Rb BEC. Assuming an atom-ion scattering length of  $a_{IB} = 100$  nm and an atomic density  $n_{at} = 10^{14} \text{ cm}^{-3}$  we obtain  $\beta \approx 10$ . The atom-ion system would therefore exhibit strong coupling behavior which has neither been realized in neutral gases nor in solid state phase. At large coupling parameters  $\beta \gtrsim 20$  the polaron binding energy converges to  $E_b \approx 0.32 E_0 \approx 1.5 \mu\text{K} \cdot k_B$  in the Ba-Rb system. Obviously, the scattering length  $a_{IB}$  is crucial to the character and magnitude of the polaron effects. The value of 100 nm seems a conservative estimate when comparing to the range determined from the semiclassical cross section  $\sigma_{ai}$  at ultralow energies. Polaron binding energies on the order of  $10 \mu\text{K}$  may therefore be realistic. Polaronic states may be observable at ion energies below this threshold. However, it should be kept in mind that several partial waves will contribute to the interaction at these energies and the theoretical treatment of the polaron would have to be expanded accordingly. Also, the detection of polarons in the described system may be severely hampered by atom-ion three-body recombination.

Although experimental obstacles exist, the exploration of polaron physics seems a central application of atom-ion systems. The availability of single charged impurities that strongly interact with the neutral environment provides an ideal starting point for these investigations.

### 1.3.5 Mesoscopic molecular ions

A fascinating novel many-body bound state has been predicted to form in an ultracold atom-ion setting [13]. The neutral atoms are promoted into loosely bound states of the  $1/r^4$  polarization potential surrounding the ion. The binding energy of the most loosely bound level is given by  $E_b = \frac{\hbar^2}{2\mu a_{ai}^2}$ , where  $\mu$  and  $a_{ai}$  denote the reduced mass and the scattering length of the atom-ion system. For typical parameters, this energy is on the order of 100 nK. The capture of atoms into these states can occur either by spontaneous or stimulated processes. Spontaneous capture requires a third collision partner to carry away the released binding energy. Under typical conditions, this will proceed via simple three-body recombination whereas phonon assisted transitions become important at extremely high condensate densities. As the population of more deeply bound levels is predicted to be strongly suppressed, the resulting molecular ion can be pictured as being "hollow" with loosely bound

atoms orbiting the ionic core at a distance comparable to  $a_{\text{ai}}$ . The total number of atoms bound by a single ion can be on the order of 1000 so that the entire object grows to mesoscopic dimensions. An upper limit for the number of bound atoms is reached when thermal fluctuations of the system become comparable to the binding energy of the last bound level. Again, temperatures around 100 nK can be expected to be necessary to attain sizable effects. The mesoscopic ion can also be populated by driving stimulated transitions into the bound states via lasers. This method may provide a way to rapid formation of the molecular state within microseconds and could help avoid detrimental effects of atom-ion three-body recombination.

### 1.3.6 Trap-induced atom-ion resonances and quantum information applications

The tunability of the details of the trapping potentials and the possibility to tightly confine both atoms and ions may be exploited for the realization of controlled collisions [50]. While tight ionic confinement is usually easily realized, reaching atomic trapping frequencies well into the kHz regime often requires the loading of atoms into optical lattices. By doing so, large numbers of atoms can be initially prepared in the ground states of the individual lattice sites constituting a quantum register. An ion may then be used to transport information between different sites. As a prerequisite, the collision of a single ion with a single atom, both in the ground state of their respective trapping potentials, must be understood. A special situation arises here due to the long-range atom-ion interaction potential in combination with the tight trapping potentials. Depending on the distance  $d$  between atom and ion, this can lead to trap-induced shape resonances (for  $d \sim R^*$ ) or confinement-induced resonances ( $d \rightarrow 0$ ). In both cases, vibrational states become equal in energy to molecular states giving rise to avoided crossings. A very precise control of the trap positions may therefore be used to employ controlled atom-ion collisions by traversing the avoided crossings either diabatically or adiabatically. In a next step, this can be exploited to implement atom-ion quantum gates [51].

Apart from the high level of control over atomic and ionic degrees of freedom, the above scheme also requires ion energies close to the ground state of the ion trap. In addition, ion micromotion severely complicates the atom-ion collisional processes [52]. Nonetheless, the regime in which the length scales of the external confinement and the interaction potential are similar in magnitude is reachable with present day technology. First experimental tests of the implications on atom-ion scattering properties could therefore be devised.

### 1.3.7 Mutual sensitive probing of atomic and ionic systems

As a final point, I want to mention a more general notion of why it is interesting to propel the studies of atom-ion systems. As was detailed in the beginning of this chapter, both trapped ions and atoms have been intensely investigated over the last few decades. Consequently, extensive experimental toolboxes are available for the two systems. By setting up hybrid traps and exploiting the atom-ion interaction, these toolboxes can now be used, to some degree, to extract information on the respective other system. In this way, novel effects can be detected which previously were either not observable or not expected. Our work on compensating ion micromotion by using solely atomic signals demonstrates the probing of a trapped ion via its interaction with atoms (see chapter 4). On the other hand, three-body recombination of neutral atoms can be investigated by ionizing and trapping the molecules that are formed (see chapter 6). As the understanding and control of the atom-ion interactions increases, many more examples of such mutual probing experiments can be expected to further deepen our knowledge of atomic and ionic systems.

## 1.4 Overview of the thesis

This thesis is structured as follows.

*Chapter 2* gives an account of the experimental apparatus used. Experimental issues and their solutions in the context of hybrid atom-ion traps are discussed.

*Chapter 3* reports first experimental results obtained by immersing single ions into BECs of Rb atoms. Charge transfer reactions, elastic scattering and the relevance of ion micromotion are highlighted and a first rough framework for atom-ion dynamics is established. The successful local probing of atom clouds using a single ion is also shown.

*Chapter 4* focusses on elastic atom-ion scattering fully taking into account the implications of the micromotion in a Paul trap. The differential atom-ion scattering cross section is derived and used for the implementation of Monte Carlo simulations of the collision dynamics. It is demonstrated that the back-action of the ion on the atomic samples can be exploited to perform micromotion compensation via atomic signals alone. Further, long-term measurements of the drift of the optimal micromotion compensation voltages are shown and discussed.

*Chapter 5* covers the topic of three-body recombination between a single ion and two of its parent atoms. The process is found to release large amounts of energy making it detectable by analyzing atom number statistics. It is shown that atom-

ion three-body interactions become increasingly important as the collision energy is lowered.

*Chapter 6* shows how our hybrid atom-ion apparatus can be used as an extremely sensitive detector for the products of three-body recombination between neutral atoms. By photoionizing and trapping the molecules formed in these reactions, we demonstrate a novel method accessing the final states populated in three-body recombination.

*Chapter 7* provides a short outlook on possible future developments of atom-ion experiments, especially in the direction of truly ultracold atom-ion interaction.

## 1.5 Publications

The following articles were published in the course of this thesis:

- S. Schmid, A. Härtter, and J. Hecker Denschlag, "Dynamics of a Cold Trapped Ion in a Bose-Einstein Condensate", *Phys. Rev. Lett.* **105**, 133202 (2010)  
(congruent with chapter 3)
- S. Schmid, A. Härtter, A. Frisch, S. Hoinka, and J. Hecker Denschlag, "An apparatus for immersing trapped ions into an ultracold gas of neutral atoms", *Rev. Sci. Instrum.* **83**, 053108 (2012)  
(congruent with chapter 2)
- A. Härtter, A. Krükow, A. Brunner, W. Schnitzler, S. Schmid, and J. Hecker Denschlag, "Single Ion as a Three-Body Reaction Center in an Ultracold Atomic Gas", *Phys. Rev. Lett.* **109**, 123201 (2012)  
(congruent with chapter 5)
- A. Härtter, A. Krükow, M. Deiß, B. Drews, E. Tiemann and J. Hecker Denschlag, "Shedding Light on Three-Body Recombination in an Ultracold Atomic Gas", *arXiv:1301.5518* (2013) (online preprint)  
(congruent with chapter 6)

# Chapter 2

## An apparatus for immersing trapped ions into an ultracold gas of neutral atoms

Review of Scientific Instruments **83**, 053108 (2012)

Stefan Schmid<sup>1,2</sup>, Arne Härter<sup>1,2</sup>, Albert Frisch<sup>2</sup>, Sascha Hoinka<sup>1,3</sup>,  
and Johannes Hecker Denschlag<sup>1,2</sup>

<sup>1</sup>*Institut für Quantenmaterie und Center for Integrated Quantum Science and  
Technology IQ<sup>ST</sup>, Universität Ulm, 89069 Ulm, Germany*

<sup>2</sup>*Institut für Experimentalphysik und Zentrum für Quantenphysik, Universität  
Innsbruck, 6020 Innsbruck, Austria*

<sup>3</sup>*ARC Centre of Excellence for Quantum-Atom Optics, Centre for Atom Optics and  
Ultrafast Spectroscopy, Swinburne University of Technology, Melbourne 3122,  
Australia*

We describe a hybrid vacuum system in which a single ion or a well defined small number of trapped ions (in our case Ba<sup>+</sup> or Rb<sup>+</sup>) can be immersed into a cloud of ultracold neutral atoms (in our case Rb). This apparatus allows for the study of collisions and interactions between atoms and ions in the ultracold regime. Our setup is a combination of a Bose-Einstein condensation (BEC) apparatus and a linear Paul trap. The main design feature of the apparatus is to first separate the production locations for the ion and the ultracold atoms and then to bring the two species together. This scheme has advantages in terms of stability and available

access to the region where the atom-ion collision experiments are carried out. The ion and the atoms are brought together using a moving 1-dimensional optical lattice transport which vertically lifts the atomic sample over a distance of 30 cm from its production chamber into the center of the Paul trap in another chamber. We present techniques to detect and control the relative position between the ion and the atom cloud.

## 2.1 Introduction

In recent years, both the fields of cold trapped ions and of neutral, ultracold atomic gases have experienced an astonishing development. Full control has been gained over the respective systems down to the quantum level. Single ions can be selectively addressed and their quantum states can be coherently manipulated and read out [31]. The collective behavior of neutral atomic quantum gases can be mastered by controlling the particle-particle interactions, temperature, and physical environment [53].

Over the last two decades increasing efforts have been made to study cold collisions between ions and neutral particles. One approach is to study collisions in a cold He buffer gas (see for example [38, 54–56]). Another approach for collisions in the regime of a few K uses neutral, velocity-selected particles from a beam of molecules to collide with trapped ions [57]. In recent years collisions between atoms in a magneto-optical trap (MOT) and trapped ions trap have been observed [14, 21, 24, 58–60]. In 2010, in parallel to the group of M. Köhl [15, 17, 61], our group has finally demonstrated immersing trapped ions in a BEC of Rb atoms at nK temperatures [16].

Here we describe the hybrid apparatus used for our atom-ion collision experiments in detail. A central design concept of our setup is the spatial separation of the BEC apparatus - where the ultracold atoms (or a BEC) are produced - from the ion-trapping region, where the atom-ion collision experiments are performed. This way we gain valuable optical access to the atom-ion interaction region, that is necessary for trapping, manipulating, and detecting the atoms and ions. Furthermore, the separation and isolation of the production sites ensures that any mutual disturbance between the radiofrequency (rf) Paul trap and the rf used for forced evaporative cooling of the atomic sample is minimized. To transport the atoms over 30 cm from their place of production to the trapped ions, we employ a moving 1-dimensional (1-d) optical lattice.

As demonstrated in a first set of experiments [16] the apparatus enables us to

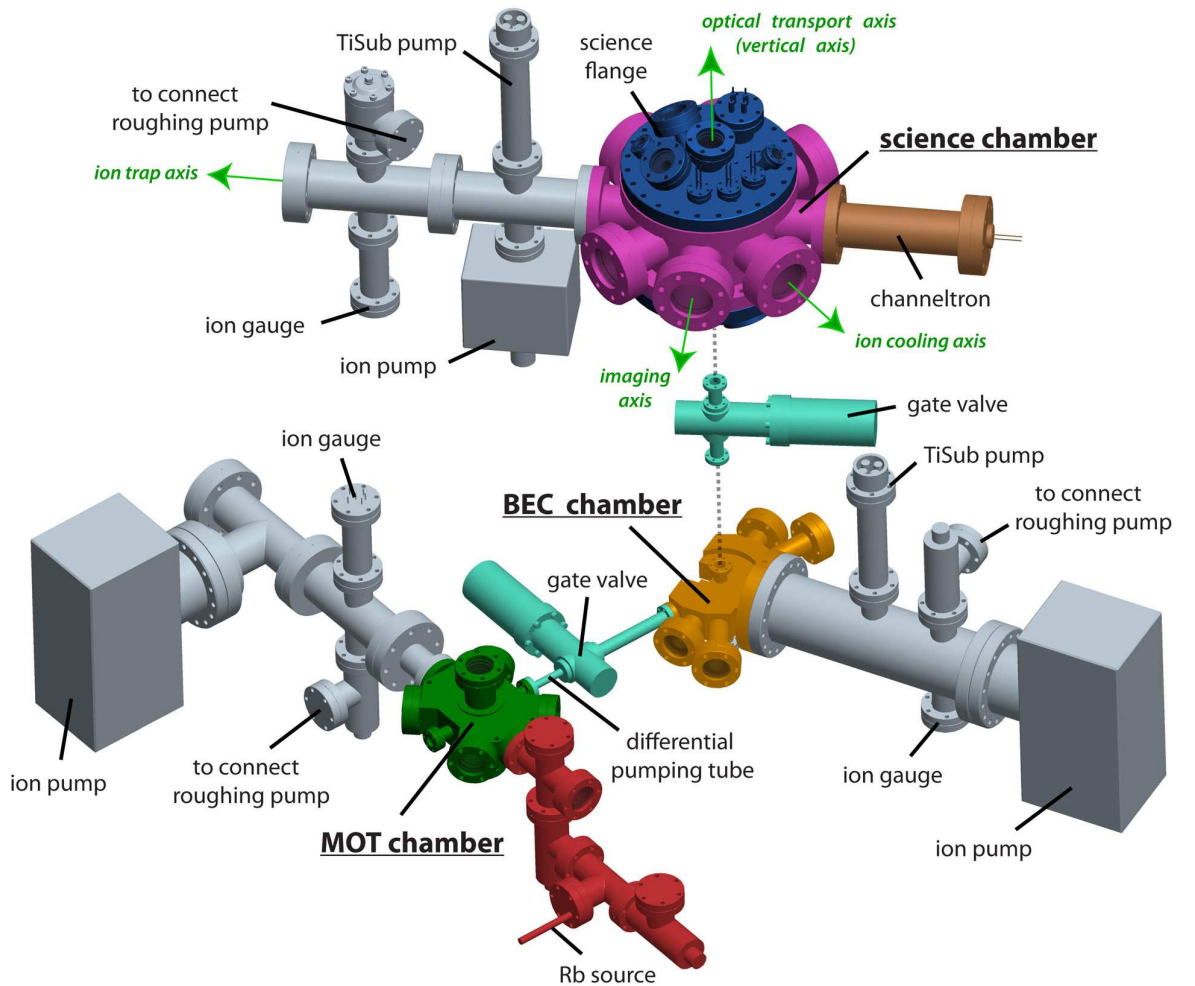


Figure 2.1: Layout of the vacuum apparatus in a partially exploded view: The science chamber (upper section) is connected to the BEC chamber (in the lower section) via a differential pumping stage (turquoise) along the dashed vertical axis. The MOT chamber (green) and the BEC chamber (red) which form the lower section are also connected via a differential pumping stage (turquoise). The science chamber exhibits a large DN200CF flange (blue) on top, the “science flange”, onto which the ion trap (not shown here) is mounted. A channeltron detector (brown) is connected along the axis of the linear ion trap. All three chambers are evacuated by their own pumping sections (grey). (Note: For better visibility the upper section is rotated clockwise by 90° around the dashed vertical axis.)

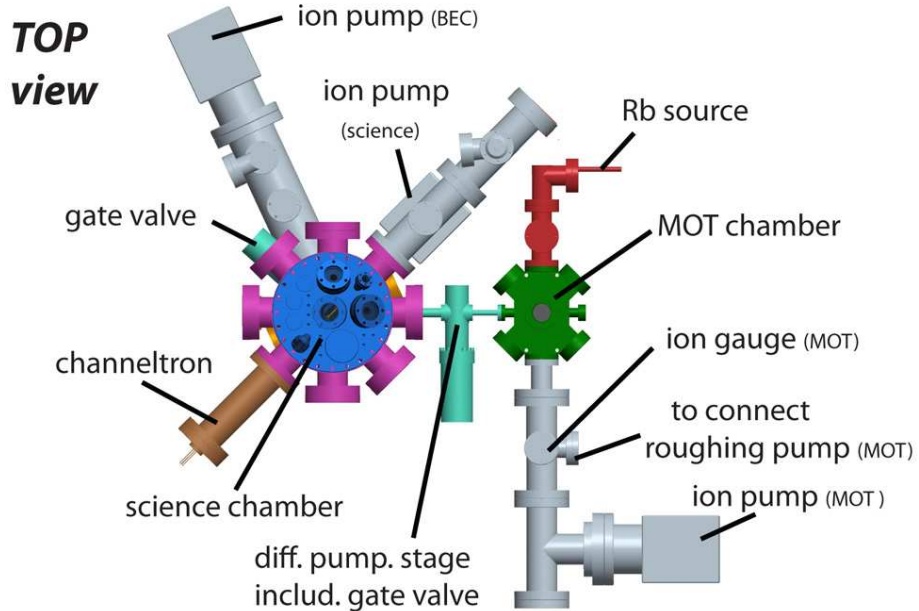


Figure 2.2: Top view of the vacuum system: The science chamber (magenta), covers up the BEC chamber (not visible).

study elastic and inelastic atom-ion collisions in the ultracold regime [12,39]. We plan to investigate cold chemical reactions and the controlled formation of cold molecular ions, topics which recently gained considerable interest (see for example [62,63]). Furthermore, the apparatus allows for carrying out other interesting lines of research. There are proposals to study the dynamics of charged impurities in a quantum degenerate gas [46,47,64], charge transport in a gas in the ultracold domain [12], or the formation of a mesoscopic molecular ion [13].

The article is organized as follows: Section II describes the layout of the multi-chamber vacuum apparatus. In Sec. III, the design and the operation of the ion trap are discussed. Section IV addresses the preparation of the ultracold atom cloud in the BEC apparatus and its optical transport into the science chamber, in which the ion trap is located. In particular, we describe an experimental procedure based on atom-ion collisions used to precisely position the atom cloud with respect to the ion.

## 2.2 The vacuum apparatus

The vacuum apparatus consists of three main building blocks. A MOT chamber for trapping and laser cooling Rb atoms. A BEC chamber for evaporative cooling of

the Rb atoms. A “science chamber” that houses the ion trap and where the ion-atom collision experiments take place. The apparatus has two floors: MOT chamber and BEC chamber form the lower section. The science chamber, forming the upper section, is located 30 cm above the BEC chamber (see Figure 2.1 and 2.2). The three vacuum chambers are connected via two differential pumping stages, each consisting of a differential pumping tube as well as a gate valve. If necessary, the vacuum chambers can be separated from each other by closing the gate valves. A series of vacuum gauges, pumps, and valves is used to evacuate the system and to determine the pressure. By baking out the setup at temperatures between 180°C and 250°C, ultrahigh vacuum (UHV) conditions are established in all three chambers. When in operation, the pressures are approximately  $10^{-9}$  mbar in the MOT chamber and  $10^{-11}$  mbar in the BEC chamber and the science chamber.

### 2.2.1 Lower section: BEC apparatus

The stainless steel (AISI 316L) MOT chamber features ten optical viewports, which are required to implement the MOT laser beams, to connect to the Rb vapor source, to pump the chamber and to move the atoms out of the MOT chamber towards the BEC chamber. An ion getter pump [65] is used to keep the MOT chamber at UHV conditions, as measured by an UHV pressure gauge (Bayard Alpert type) [66].

The Rb vapor source is an ampule filled with bulk Rb and He as an inert gas [67]. Since Rb is very reactive when exposed to air, the ampule is not cracked until the surrounding “oven section” has been evacuated. Once Rb has been released from the ampule, the pressure in the oven section is determined by the Rb vapor pressure, which is  $4 \times 10^{-7}$  mbar at room temperature. As a consequence, the pressure in the center of the MOT chamber increases from its original value of  $10^{-11}$  mbar to a few times  $10^{-9}$  mbar and is then completely dominated by the Rb vapor. If necessary, the vapor pressure can be adjusted by heating the Rb source or by changing the setting of the valve which separates the oven section from the MOT chamber.

The pressure in the BEC chamber is below  $10^{-11}$  mbar using a combination of a titanium sublimation (TiSub) pump [68] and an ion getter pump [65]. At this pressure we achieve lifetimes of the atom cloud of more than 2 min which is sufficient to carry out rf evaporative cooling.

In order to maintain a pressure gradient of  $p_{\text{MOT}}/p_{\text{BEC}} \approx 10^2$ , a differential pumping tube is used to separate the MOT and the BEC chamber. Since the size of the atom cloud, which has to be transported through the tube, amounts to a few millimeters, we chose the tube diameter to be 8 mm. Molecular flow calculations then determine

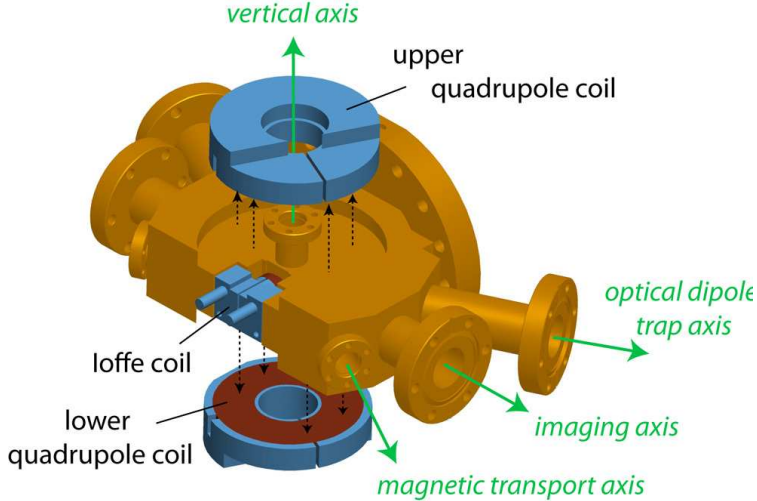


Figure 2.3: Explosion view of the BEC chamber and the magnetic QUIC trap coils. The QUIC trap is generated by the two quadrupole coils and the Ioffe coil (blue). The coils are mounted outside the vacuum to the walls of the BEC chamber. The atoms enter the chamber along the magnetic transport axis and leave it along the vertical axis.

the tube length to be 115 mm.

The design of the BEC chamber is shown in Fig. 2.3 and 2.4. After laser cooled atoms from the MOT are magnetically transported into the BEC chamber, evaporation in a Quadrupole-Ioffe configuration (QUIC) trap [69] brings the atoms to BEC or close to BEC. Afterwards they are vertically transferred to the ion trap in the science chamber. QUIC traps are typically used in combination with a glass cell, as the Ioffe coils need to be placed quite close to the atoms. In our setup where the BEC chamber is physically connected along the horizontal (to the MOT chamber) and the vertical (to the science chamber) direction, strong shear forces are acting on the chamber walls. For this reason we chose stainless steel instead of glass for the construction of the BEC chamber. To minimize the distance between the atoms and the Ioffe coil, the BEC chamber exhibits a special insertion slot with a thin end wall into which the Ioffe coil can be placed (see Fig. 2.4). The BEC chamber features four optical axes. The first axis points along the vertical direction and is needed for the optical transport of atoms from the BEC chamber into the science chamber (transport axis). On both ends small DN16CF flanges are used, so that the QUIC quadrupole coils can be easily mounted. The second axis (imaging axis) is used for imaging the ultracold atoms. DN40CF viewports are used on both ends, in order to allow for a good imaging quality. In addition, optical access along the

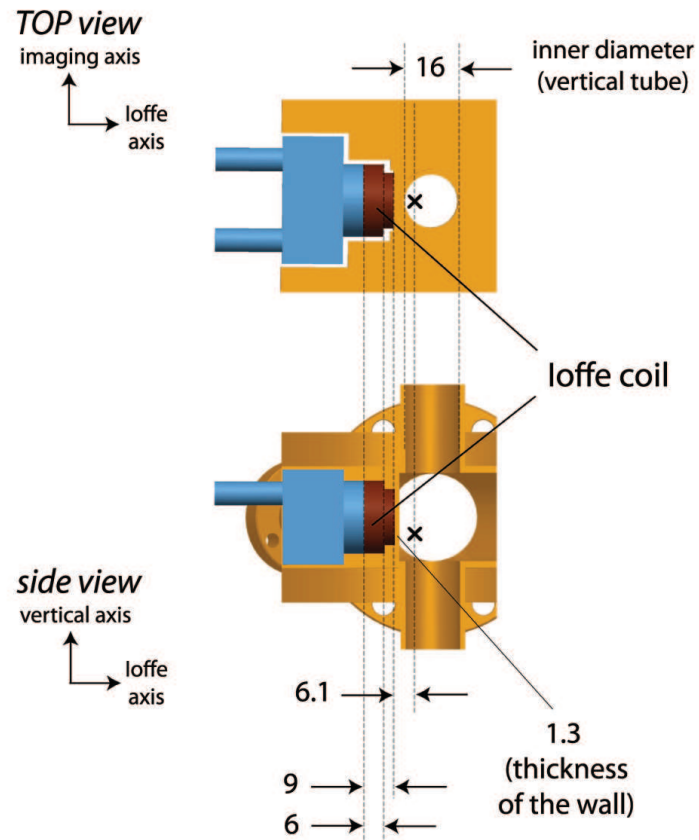


Figure 2.4: BEC chamber and Ioffe coil: The BEC chamber features a small insertion slot with an end wall thickness of only 1.3 mm, so that the Ioffe coil (brown) and its holder (blue) can be mounted at a minimum distance of only 11.1 mm from the center of the chamber. The position of the atom cloud, when it is stored in the QUIC trap, is denoted by the black cross. The dimensions are given in mm.

magnetic transport axis is desirable, in order to be able to image the atom cloud at any intermediate position of the transport. Finally, the BEC chamber features a fourth optical axis (optical dipole trap axis), which is currently not used in our experiments, but could for example be employed for the addition of a dipole trapping beam. In order to utilize the full pumping speed of our ion pump, the pumping section is connected to the BEC chamber via a DN100CF flange.

### 2.2.2 Upper section: Science chamber

The science chamber (Fig. 2.1 and 2.2), represents the heart of our vacuum apparatus since this is where the experiments take place. It is designed for maximum optical access with eight optical axes. The optical access is needed for cooling and imaging of the ions as well as for trapping, manipulating, and imaging of the atoms. All parts of the ion trap as well as an object lens to collect the ion fluorescence are mounted within the science chamber onto the “science flange” (Fig. 2.5). The flange features various electrical feedthroughs, which are needed to apply the required high voltages to the Paul-trap electrodes and to run currents of up to 12 A through the Ba oven. The DN200CF science flange is mounted on top of the science chamber.

The stainless steel, octagon-shaped science chamber (Fig. 2.1) is evacuated by a combination of an ion getter pump and a TiSub pump. As an optional addition of our setup, we have connected a channeltron ion detector [70] along the axis of the linear ion trap (see also Fig. 2.1 and 2.2). One possible application of the channeltron is the identification of ions via time-of-flight mass spectrometry as has been demonstrated in other experiments (see for example [59]).

## 2.3 Ion trapping

### 2.3.1 Linear Paul trap

We employ a linear radiofrequency (rf) Paul trap [71] (see Fig. 2.7) to store  $\text{Ba}^+$  or  $\text{Rb}^+$  ions. For the trapping of the ions along the two radial directions we use four blade electrodes, which are mounted symmetrically at a distance of  $r_0 = 2.1 \text{ mm}$  from the trap axis. A rf of  $\Omega = 2\pi \times 5.24 \text{ MHz}$  with an amplitude of  $2 \times U_{\text{rf}} = 1400 \text{ V}_{\text{pp}}$  is applied to two of the four blades, whereas the other two are grounded. The rf is generated by a commercially available function generator [72] and subsequently amplified by a 5 W rf amplifier from Minicircuits [73]. The power at the output of the amplifier is inductively coupled to the trap electrodes via a ferrite-toroid transformer

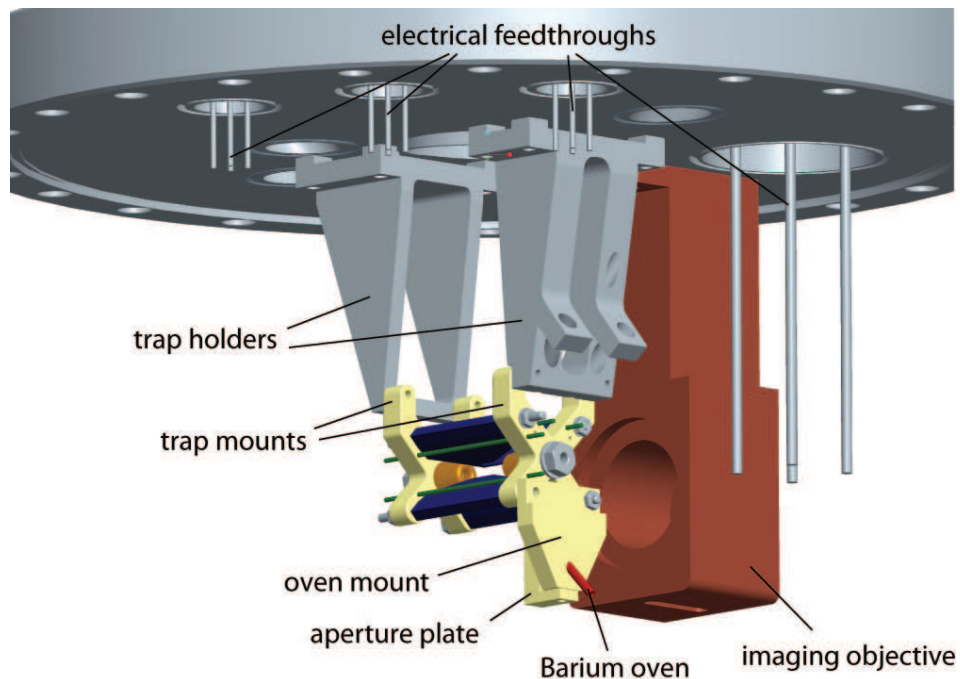


Figure 2.5: Science flange (DN200CF): The Paul trap (blue and golden) as well as the Ba oven (red) are mounted on MACOR ceramic parts (pale yellow). The imaging objective consists of four lenses, all of them held in place by a massive aluminum mount (brown) (see also section 2.3.4).

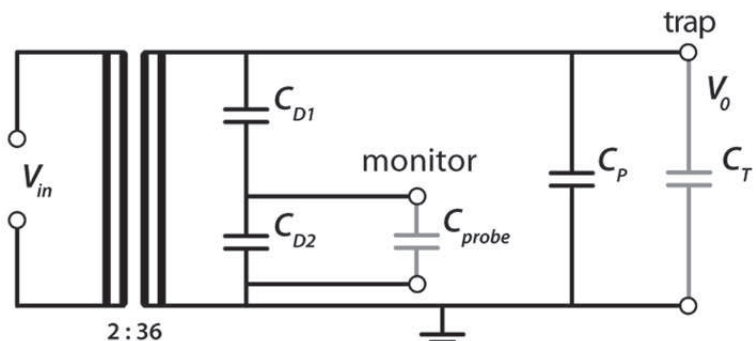


Figure 2.6: Ferrite-toroid transformer with a turns ratio of 2:36. By adjusting the capacity  $C_p$  the impedance of the trap (corresponding to  $C_T$ ) is matched and the ratio between the output and the input voltage ( $V_o/V_{in}$ ) is maximized. In order to be able to monitor the output voltage, a capacitive voltage divider ( $C_{D1}$  and  $C_{D2}$ ) is used.

(see Fig. 2.6). The impedance of the trap is matched, so that the supply voltage is resonantly enhanced by a factor of 30. Trapping along the axial direction is achieved by applying dc voltages on the order of 100 V to the two endcap electrodes which are located on the trap axis at a distance of 7 mm from the trap center. Typical ion trapping frequencies for the parameters given above are  $\omega_{\text{rad}} \approx 2\pi \times 250$  kHz and  $\omega_{\text{ax}} \approx 2\pi \times 80$  kHz for  $\text{Ba}^+$  and  $\omega_{\text{rad}} \approx 2\pi \times 390$  kHz and  $\omega_{\text{rad}} \approx 2\pi \times 100$  kHz for  $\text{Rb}^+$ . As expected, the trap frequencies of our ions in the linear Paul trap scale in first order as  $\omega_{\text{rad}} \propto 1/m$  and  $\omega_{\text{ax}} \propto \sqrt{1/m}$ . The stability factor  $q$  is generally given by  $q = 2eU_{\text{rf}}/(m\gamma r_0^2\Omega^2)$  [74], where  $\gamma = 1.53$  is a numerical factor that depends on the exact geometry of the rf electrodes. Our Paul trap allows stable trapping of both  $\text{Ba}^+$  and  $\text{Rb}^+$ , since  $q \ll 1$  for both species ( $q = 0.13$  for  $\text{Ba}^+$  and  $q = 0.21$  for  $\text{Rb}^+$ ).

All electrodes are made of non-magnetic, high-grade, stainless steel of type AISI 316L. This material is specified to have a magnetic permeability of  $\mu < 1.005$ . The blades are produced by electrical discharge machining, which allows for a higher precision and a smaller surface roughness as compared to milling. The electrodes are mounted onto two insulating parts, which are made out of a machinable glass-ceramic (MACOR). This material has a very low outgassing rate and is thus well suited for UHV applications.

### 2.3.2 Loading and laser cooling of ions

We load the Paul trap (Fig. 2.7) with either  $^{138}\text{Ba}^+$  or  $^{87}\text{Rb}^+$  ions. To work with  $\text{Ba}^+$ , we run a current of about 8 A (corresponding to 6 W) through the commercially available Ba source [75] (see Fig. 2.5). It is a stainless steel tube with a diameter of 2 mm, which is filled with metal alloy containing Ba. Ba vapor is created through sublimation out of the alloy. In the center of the trap, the neutral Ba atoms emitted by the oven are photoionized using a diode laser operating at 413 nm [76]. A few mW of laser power are used to drive the resonant two-photon transition from the ground state to the continuum via the  $^3\text{D}_1$  state. With this procedure we are able to load single ions into our trap within a few minutes.

We perform Doppler cooling of the  $^{138}\text{Ba}^+$  ions on the  $6\text{S}_{1/2} \rightarrow 6\text{P}_{1/2}$  cycling transition, which has a transition wavelength of 493 nm and a linewidth of 15.1 MHz. The corresponding Doppler temperature is  $360 \mu\text{K}$ . The 493 nm cooling light is generated via frequency doubling of a 986 nm diode laser. Both the diode laser and the frequency-doubling stage are part of the commercially available system “DL SHG” from Toptica. To stabilize the frequency of the 493 nm light, the 986 nm laser is locked to a temperature-stabilized optical cavity using the well-established Pound-

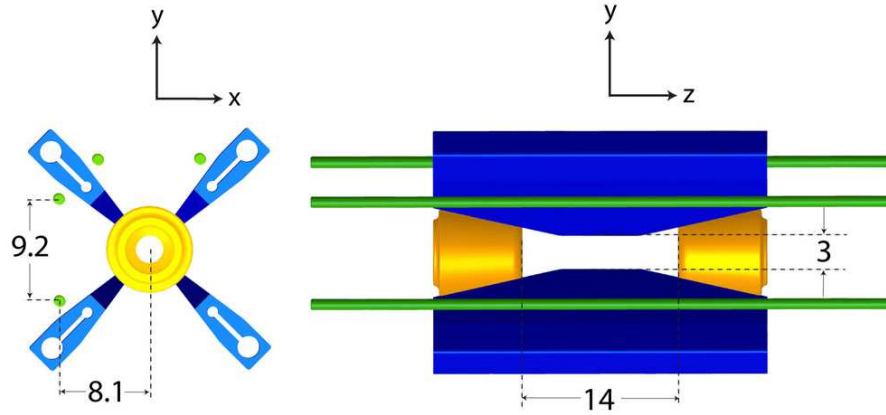


Figure 2.7: Linear ion trap (Paul trap). The trap consists of four rf electrodes (blue) for confinement in the x-y plane, two endcap electrodes (golden) for confinement along the z axis, and four compensation electrodes (green) for the generation of dc electrical fields in the x-y plane. All electrodes are made of stainless steel AISI 316L. The dimensions are given in mm.

Drever-Hall method [77, 78]. An additional “repumper” laser at a wavelength of 650 nm is needed, in order to bring the atoms from the metastable  $5D_{3/2}$  state back into the cooling cycle. The repumper is a home-made external-cavity diode laser, which features an anti-reflection-coated laser diode to guarantee stable lasing at the desired wavelength. The frequency of the repumper is stabilized using the same locking scheme as for the 986 nm laser.

To work with clouds of  $Rb^+$  ions, we transport ultracold Rb atoms into the center of the Paul trap and ionize them using the imaging laser at 780 nm together with the ionization laser at 413 nm. The resonant imaging laser brings the Rb atom into the  $5P_{3/2}$  state, so that the 413 nm laser can then drive the transition into the continuum. Since we start with an ultracold trapped atom source, this ionization procedure is very fast and efficient. It allows for loading clouds of  $Rb^+$  ions into the Paul trap within a few milliseconds.

We employ a different scheme when performing experiments with single  $Rb^+$  ions. In this case, we first load a single  $Ba^+$  ion into the Paul trap following the procedure described above. Then we let the  $Ba^+$  ion interact with ultracold Rb atoms until the charge transfer process  $Rb + Ba^+ \rightarrow Rb^+ + Ba$  has taken place. This takes typically a few seconds. The newly formed  $Rb^+$  ion is “dark”, as it cannot be detected via standard fluorescence imaging due to the lack of an accessible cycling transition. Therefore  $Rb^+$  has to be detected via its elastic collisions with the neutral atoms and the corresponding atom losses. The newly formed  $Rb^+$  ion is available

for thousands of experimental cycles, since its lifetime in the Paul trap is typically on the order of days.

### 2.3.3 Micromotion

In addition to the pseudopotential generated by the rf drive, dc stray electric fields are also present. Possible sources of these fields are imperfections in the fabrication of the trap or patch charges on the ceramic parts. Such surface charges could be generated by our blue Ba<sup>+</sup> lasers (413 nm and 493 nm) via the photoelectric effect. In any case, the dc fields push the ion out of its ideal trap location, the rf node, into a region of non-vanishing rf, leading to the so-called “excess micromotion” of the ion [74]. In order to minimize this enhanced micromotion, we have to compensate the dc electric offset fields at the position of the ion. To compensate electrical offset fields in the axial direction we can apply corresponding voltages to the endcaps of the Paul trap. To generate compensation fields along the radial direction, four “compensation electrodes” (two for each direction) are added to the design of the linear Paul trap. By placing the electrodes at a distance of 9.35 mm from the trap axis and applying a voltage  $U_{\text{comp}}$ , we are able to generate dc compensation fields of  $E_{\text{comp}} = \beta U_{\text{comp}}$ , where  $\beta = 3.1 \text{ m}^{-1}$ .

A simple and in our system very accurate method to detect excess micromotion is to determine the position shift of the ion when the rf amplitude is changed. By adjusting the compensation fields such that the position shift is minimized, we can assure that the potential minimum nearly coincides with the rf node. This method works nicely for electric fields along the vertical direction. However, for the compensation of fields along the  $x$ -axis a different method has to be used, since we are not able to measure the  $x$  position of the ion with high accuracy. One possibility, realized in our setup, is to modulate the amplitude of the rf drive. Setting the modulation frequency equal to the trap frequency leads to resonant heating of the ion, which can be detected via a smearing of the ion fluorescence. The heating is particularly strong when the ion is not in the rf node. Hence, we can adjust the compensation fields by minimizing the heating. In early experiments, using the methods described here, we were able to reduce the dc electric fields at the position of the ion to about 1 V/m [16].

### 2.3.4 Imaging methods

We detect the ion by collecting its fluorescence using a high-aperture laser objective (HALO) from Linos (see Fig. 2.7). The HALO has a numerical aperture of  $NA = 0.2$  and a focal length of  $f = 60\text{ mm}$ , which enables us to detect about  $NA^2/4 \approx 1\%$  of the spontaneously emitted photons. It is placed inside the vacuum chamber at a distance of  $f = 60\text{ mm}$  from the trap center. Since the original mount of the HALO is anodized and generally not designed to be put into a UHV environment, it was exchanged by a UHV-capable aluminum mount. This new mount features an air vent in order to avoid slow outgassing of air that is enclosed in between the different lenses of the objective.

The collimated fluorescence light exits the chamber through a DN63CF AR-coated viewport. An  $f = 300\text{ mm}$  achromat is then used to focus the light onto the EM-CCD chip of an Andor Luca(S) camera. Diffraction at the aperture of the HALO ultimately limits the resolution of the imaging system to about  $1.5\text{ }\mu\text{m}$ , which is an order of magnitude smaller than the typical distance between two neighboring ions of an ion string.

Absorption imaging of the cloud of neutral atoms is also done with the HALO. To separate the Rb imaging beam ( $780\text{ nm}$ ) from the  $\text{Ba}^+$  fluorescence light ( $493\text{ nm}$ ), we use a dichroic mirror. Together with the HALO, an  $f = 200\text{ mm}$  achromat forms the objective for the neutral atom detection. The large spacing between the ion-trap electrodes allows for taking the images not only in-situ but also after a free expansion of the atom cloud of up to 15 ms.

## 2.4 Preparation and delivery of ultracold atomic samples

After the ion has been trapped, we start the production of an ultracold atom cloud in the lower section of the vacuum apparatus. The time needed to create a Rb cloud with  $2 \times 10^6$  atoms at a temperature of about  $1\text{ }\mu\text{K}$  is approximately 35 s. Another 5 s are required to transport the atom cloud into the science chamber and to perform further forced evaporative cooling in an optical dipole trap down to BEC or to cold thermal ensembles with typical temperatures of 100 nK.

### 2.4.1 MOT loading and magnetic trap

To operate the MOT, we have set up two external-cavity diode lasers tuned to the  $5^2S_{1/2} \rightarrow 5^2P_{3/2}$  transition in  $^{87}\text{Rb}$ . One of the diode lasers is locked to the  $|F = 2\rangle \rightarrow |F' = 3\rangle$  cycling transition using the modulation transfer spectroscopy technique [79]. The light from this laser is amplified with a tapered amplifier [80] and sent through a polarization-maintaining (PM) optical fiber. After the fiber the total power of 250 mW is split up into six beams, all of them having a diameter of 30 mm. Using acousto-optical modulators the cooling light is detuned to about  $-3.5\Gamma$  relative to the cycling transition, where  $\Gamma = 6 \text{ MHz}$  is the transition linewidth. Our second Rb laser is locked to the  $|F = 1\rangle \rightarrow |F' = 1\rangle / |F' = 2\rangle$  cross over line using the frequency modulation (FM) technique [81]. This repumper laser is used to pump the atoms from the  $|F = 1\rangle$  groundstate back into the cycling transition. To operate the MOT a total repump power of  $6 \times 1.5 \text{ mW}$  is employed. The required magnetic field gradient of  $B'_z = 8 \text{ G/cm}$  is generated by running a current of 5 A through a pair of anti-Helmholtz coils. This setup enables us to load about  $3 \times 10^9$   $^{87}\text{Rb}$  atoms from the background vapor into the MOT.

By turning off the magnetic field and detuning the MOT cooling beams to about  $-8.5\Gamma$ , we perform polarization-gradient cooling for a duration of 10 ms. In this way, the temperature of the atoms is reduced to about  $40 \mu\text{K}$ . In a next step the atoms are optically pumped into the lowest magnetically trappable state  $|F = 1, m_F = -1\rangle$  and subsequently loaded into a magnetic quadrupole trap. The trap is generated by running 80 A through the MOT coils leading to a magnetic field gradient of  $B'_z = 130 \text{ G/cm}$ , which is sufficient to hold the atoms against gravity. The number of the atoms now amounts to nearly  $1 \times 10^9$ .

### 2.4.2 Magnetic transport and QUIC trap

Following the concept described in Ref. [82] (see also [83]), the cold atom cloud is transported magnetically from the MOT chamber to the BEC chamber. For the transport we employ 13 pairs of anti-Helmholtz coils and an additional “push coil”. By properly ramping the currents through the coils, it is possible to smoothly shift the position of the atoms, which are trapped in the magnetic field minimum. We are able to move the cloud over a distance of 431 mm within 1.5 s. The final particle number after transport is typically  $5 \times 10^8$ , corresponding to an overall transport efficiency of about 50%. The temperature of the atom cloud increases from initially  $150 \mu\text{K}$  to about  $230 \mu\text{K}$ .

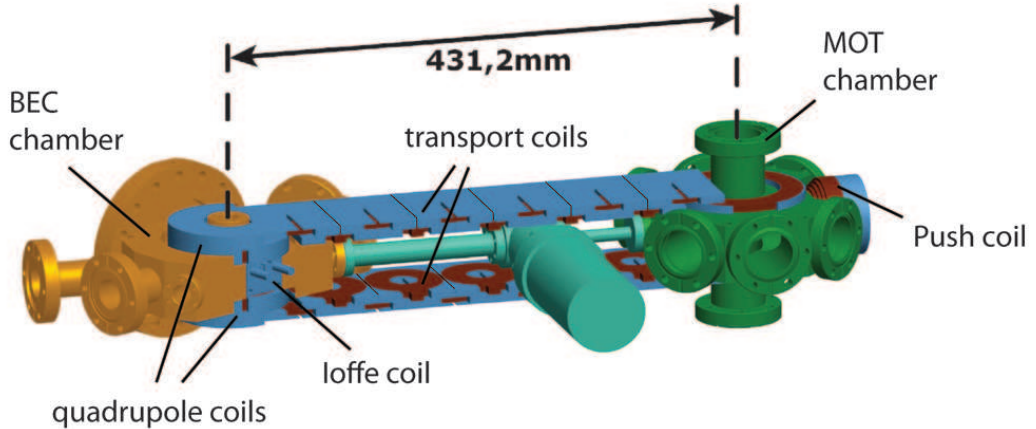


Figure 2.8: Magnetic transport line: The neutral atom cloud is transported over a distance of 431.2 mm from the MOT chamber (green) to the BEC chamber (golden). Together with their respective aluminum housings (blue) the required magnetic field coils (brown) are mounted to the stainless steel chambers.

At the end of the transport the atoms are loaded into the QUIC trap, which consists of the so-called quadrupole coils together with a small diameter end coil (Ioffe coil) (see Fig. 2.3 and 2.9). In a first step, the current through the quadrupole coils is ramped from 16 A (used for the transport) to 36 A and thus the magnetic field gradient is increased from  $B'_z = 130 \text{ G/cm}$  to  $B'_z = 320 \text{ G/cm}$ . Subsequently, we ramp the current through the Ioffe coil from 0 to 36 A. At the end of the ramp, a single power supply is used to drive the quadrupole coils and the Ioffe coil, which are connected in series. Having all the QUIC coils wired up in the same circuit minimizes heating of the atom sample and leads to a  $1/e$  lifetime of thermal atom clouds of about 2 min. The coil system generates an offset magnetic field of about 2 G and a nearly harmonic potential with trapping frequencies of  $(\omega_x, \omega_y, \omega_z) = 2\pi \times (105, 105, 20) \text{ Hz}$ , where the z-direction is along the Ioffe axis.

We perform rf-induced forced evaporative cooling to reduce the temperature of the atom cloud by more than two orders of magnitude. To selectively remove hot atoms, a small coil with 3 turns and a diameter of about 20 mm is placed inside the vacuum at the bottom of the BEC chamber at a distance of 13 mm from the atoms. The coil is driven with 30 dBm of rf power and the frequency is ramped from initially 60 MHz down to about 3 MHz within 20 s. With this procedure we are in principle able to produce Bose-Einstein condensates of up to  $3 \times 10^5$  atoms. However, for our experiments we stop the evaporation before we reach BEC, resulting in a thermal atom cloud with about 1  $\mu\text{K}$  temperature and an atom number of about

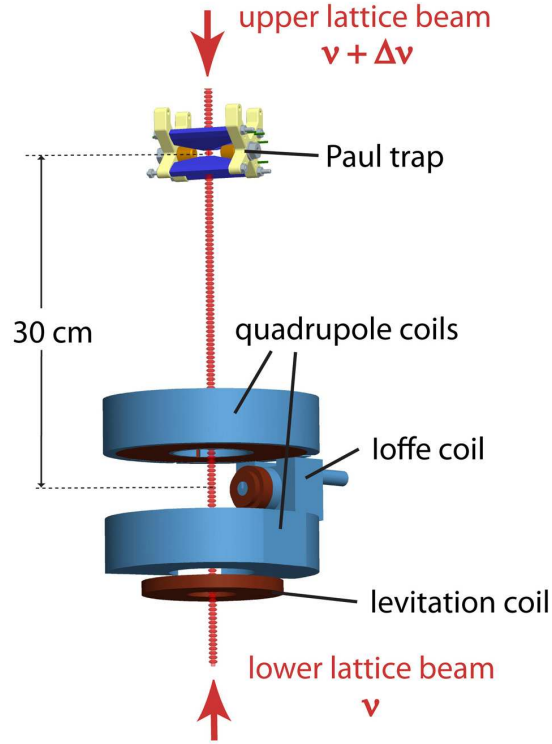


Figure 2.9: A moving optical standing wave is used to transport the ultracold atoms vertically from the QUIC trap in the BEC chamber into ion trap in the science chamber. The distance between QUIC trap and Paul trap is not to scale.

$2 \times 10^6$ . As compared to the BEC the thermal cloud experiences much smaller losses due to three-body collisions during the subsequent optical transport into the science chamber.

### 2.4.3 Optical transport of ultracold atoms

One of the key features of the experimental setup is the vertical long-distance optical transport of the ultracold atoms from the BEC chamber into the science chamber. An illustration is given in Fig. 2.9. We follow a scheme similar to that described in Ref. [84] (where, however, the optical transport was in horizontal direction). The ultracold atoms are first adiabatically loaded from the QUIC trap into a vertical far red-detuned 1-d optical lattice within 300 ms. As the lattice is set into motion it drags along the atoms, like an elevator. After a transport distance of about 30 cm, corresponding to the distance between BEC chamber and science chamber, the lattice is brought to a halt and the atoms are transferred into a crossed dipole trap.

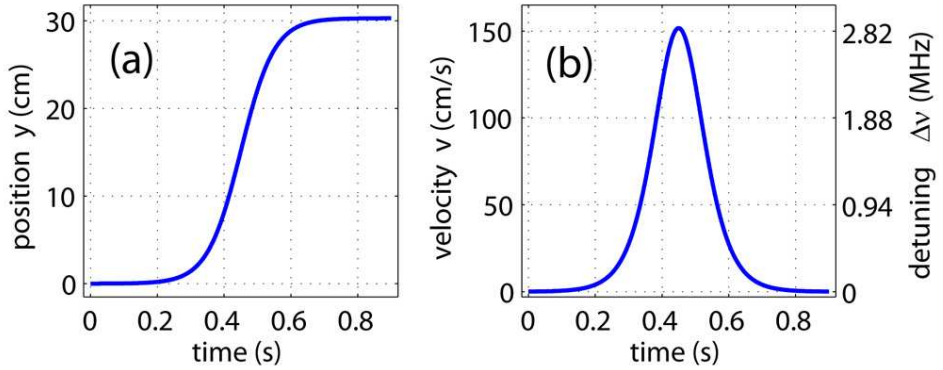


Figure 2.10: Optical transport of ultracold atoms. (a) A ramp of the form  $y(t) = D[\tanh(n(2t - T)/T) + \tanh(n)]/2 \tanh(n)$  is chosen for the vertical position of the atoms versus time, where  $D = 304$  mm is the transport distance,  $T = 0.9$  s the transport time, and  $n = 4.5$  the form parameter. (b) From the ramp  $y(t)$  we can derive the velocity  $v(t)$  of the atoms and the corresponding relative detuning (frequency shift)  $\Delta\nu(t)$  between the two lattice beams.

In order to load the atomic cloud into the 1-d optical lattice, it first has to be shifted from its location close to the Ioffe coil (where the evaporation takes place) back to the center of the quadrupole coils which is about 5 mm away. This shift is controlled via magnetic fields from various magnetic coils. Motion along the Ioffe axis (see Fig. 2.3) can be induced by changing the current through the quadrupole coils while keeping the Ioffe current constant. For position changes along the imaging direction (which is orthogonal to the Ioffe axis), we operate the last pair of the magnetic transport coils. The exact position along the (third) vertical axis is irrelevant, since the atoms can be loaded into any antinode of the optical lattice. Nevertheless, we added a levitation coil (see Fig. 2.9) to the system, which can be used to control the vertical position of the atoms. This way we can prevent the atoms from leaving the region to which we have good optical access. In order to optimize the overlap between the magnetic trap and the optical standing wave, we perform Bragg diffraction of the magnetically confined atom cloud using the 1-d optical lattice. We adjust the position of the QUIC trap such that the Bragg diffraction and thus the overlap is maximal. We can determine the lattice depth experienced by the atoms by measuring how the diffraction pattern changes as we vary the length of the Bragg diffraction pulses. For the experimental parameters used in our setup about 100 lattice cells are occupied by the atoms.

The optical lattice is formed by two counterpropagating collimated Gaussian laser beams at  $\lambda = 1064$  nm with a power of 1.25 W and 0.5 W, respectively. For both

lattice beams, the diameter at the waist was chosen to be about  $500\,\mu\text{m}$ , so that the divergence of the beams can be neglected. The light is derived from a home-made fiber amplifier which is seeded by a diode-pumped solid-state laser [85]. Due to its very low spectral linewidth ( $\approx 1\,\text{kHz}$ ), the laser is well suited for the generation of an optical lattice. Both beams are sent through acousto-optic modulators (AOM) in order to control their frequency as well as their intensity. At the beginning of the transport, both AOMs are driven with a rf of  $80\,\text{MHz}$ . For the transport scheme to work, it is essential that both rfs are phase locked to each other throughout the entire transport sequence because sudden phase jumps would in general lead to atomic loss. Therefore, the rf signals are generated using digital synthesizers (AD9854) which can be locked to the same external reference oscillator. In order to make the standing wave pattern move with a velocity  $v = \Delta\nu\lambda/2$ , we detune the frequency of the upper lattice beam by  $\Delta\nu$ . When the drive frequency of an AOM is modified, the diffraction angle and the beam path of the laser beam changes. To preserve the alignment of the lattice throughout the transport, we couple the upper lattice beam through an optical fiber before sending it to the experiment. The fiber coupling limits the power of the upper lattice beam to about  $0.5\,\text{W}$ . The lattice beams enter and exit the vacuum system through AR-coated viewports, which are attached to the chamber at an angle of about  $4^\circ$  with respect to the (vertical) transport axis. By this means we ensure that the reflections off the viewports do not interfere with the standing wave.

Due to the large waist of the laser beams, the confinement of the atoms in the optical lattice sites is more than two orders of magnitude stronger in the axial (transport) direction than in the radial direction. The strong axial confinement prevents gravity from pulling the atoms out of the lattice potential even for moderate laser intensities [86]. Even in the presence of weak heating during transport, the temperature of the atom cloud stays below  $1\,\mu\text{K}$ . This is due to evaporative cooling from the lattice potentials which are only several  $k_{\text{B}} \times \mu\text{K}$  deep .

The ramp for the relative frequency shift  $\Delta\nu(t)$  between the two lattice beams is derived from the ramp for the vertical atom position  $y(t)$ . Both quantities as well as the velocity  $v(t)$  are plotted in Fig. 2.10 as a function of time. During transport, the AOM frequencies and thus also the value for the detuning  $\Delta\nu(t)$  are updated every  $40\,\mu\text{s}$ . For a given transport distance  $D$ , the transport time  $T$  and the form parameter  $n$  (see Fig. 2.10) are optimized for maximum transport efficiency. In our case we have  $D = 304\,\text{mm}$  and find a maximum efficiency of 60% for  $T = 0.9\,\text{s}$  and  $n = 4.5$ , ending up with  $1.5 \times 10^6$  Rb atoms in the science chamber.

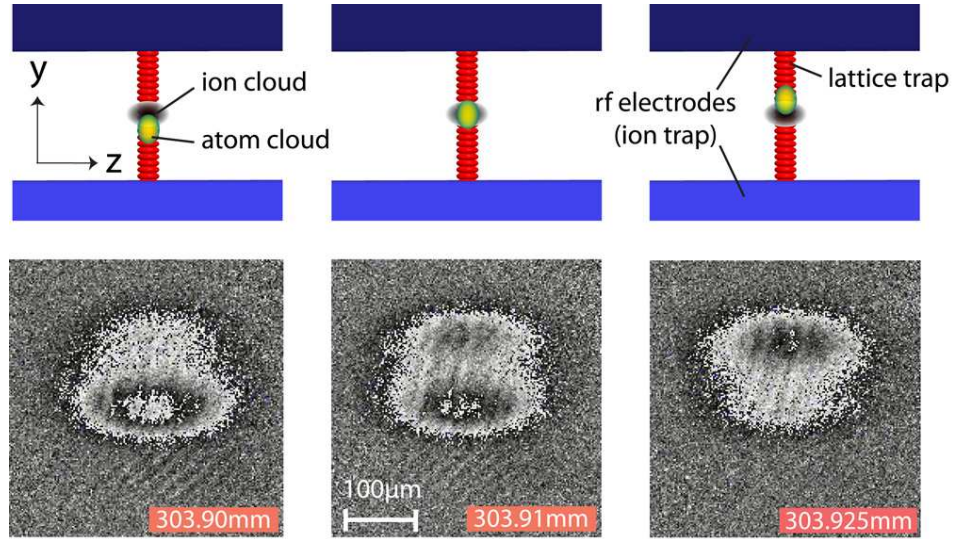


Figure 2.11: Absorption images of the atom cloud after the interaction with a localized ion cloud. The atoms are transported close to the center of the ion trap and held there for 1 s. The Paul trap is loaded with a cloud of hundreds of  $\text{Rb}^+$  ions, which are responsible for the localized loss of atoms around the ion trap center. Outside of the ion trap center the atom loss is very small, as the atoms, being trapped in lattice sites, cannot get into contact with the ion cloud. The transport distance is varied between 303.90 mm and 303.925 mm. Arrows indicate where the ion cloud has depleted the neutral atomic ensemble. For a transport distance of 303.91 mm the depletion region is located in the center of the atomic cloud, indicating a good vertical alignment. The pictures are taken after a time-of-flight of 12 ms.

The optical transport may be extended to even larger distances than described above. As a proof of principle, we have transported the atom cloud from the BEC chamber over 45 cm to the very top of the science chamber and then back into the BEC chamber again. In this experiment, the total roundtrip distance of 90 cm was only limited by the length of our vacuum apparatus.

#### 2.4.4 Adjusting the lattice transport distance

The atom transport has to be adjusted such that it stops at the exact location of the trapped ion. A simple method for this would be to use the same camera to image the locations of the ion and the lattice held atomic cloud and to adjust the transport such that they coincide. However, in our setup this is not possible since we image ions and atoms with two different cameras. We thus use a different approach which proceeds in two steps. First, an approximate value for the transport distance  $D$  is found by determining the position of the atom cloud relative to the rf electrodes via

standard absorption imaging. We choose  $D$  such that the atoms end up roughly in the center of the ion trap midway in between the lower and the upper electrodes.

Second, for a more precise adjustment, we load a cloud of hundreds of ions into the Paul trap. We then transport several freshly prepared atom clouds to the same ion cloud where the two clouds are brought to an overlap which is varied via the transport distance. After each atom cloud has been held at its respective final position an absorption image is taken (see Fig. 2.11). The atom cloud typically has an extension on the order of  $100\text{ }\mu\text{m}$  along the direction of the transport. In contrast, the ion cloud is well localized within a few tens of  $\mu\text{m}$ . We observe a substantial loss of atoms, due to elastic collisions between atoms and ions in which atoms simply get kicked out of the shallow lattice potential and are lost [16]. However, the loss takes place only in the region where the ion cloud is located (see Fig. 2.11). The strong confinement in the lattice sites prevents atoms which are located outside the ion cloud from reaching the ions. The resulting atomic distribution is shown in Fig. 2.11. We adjust the transport distance  $D$  such that the location of loss (see arrow) is centered on the atomic cloud.

#### 2.4.5 Loading of the crossed dipole trap and evaporative cooling

After transport, the atoms are loaded into a crossed optical dipole trap, formed by the lower lattice beam and an additional horizontal dipole-trap beam. This additional trapping beam is derived from the same laser as the lattice beams and propagates horizontally along the  $x'$ -axis (see Fig. 2.12), which is at an angle of  $45^\circ$  with respect to the  $x$ -axis. It has a waist of  $50\text{ }\mu\text{m}$  and is ramped up to a power of  $1\text{ W}$  within  $1\text{ s}$ . Subsequently, the power of the upper lattice beam is ramped down to zero within  $1\text{ s}$  and a crossed optical dipole trap is formed. We are able to load about 50% of the atoms from the 1-d optical lattice into this crossed dipole trap while keeping the temperature of the sample below  $1\text{ }\mu\text{K}$ .

In the next step, the depth of the dipole trap is lowered within  $4\text{ s}$  to evaporatively cool the atoms and to end up with a BEC of typically  $10^5$  atoms. If we prefer to work with a thermal atom cloud ( $T = 100\text{ nK}$ ), the evaporation is stopped immediately before the onset of Bose-Einstein condensation. The lifetime of a thermal atom cloud is typically on the order of  $10^2\text{ s}$ .

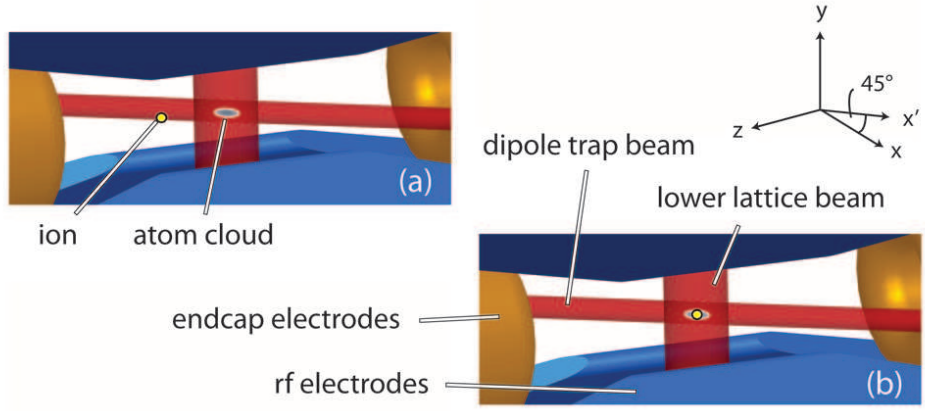


Figure 2.12: Probing the position of the optical dipole trap with a single ion. (a) First the ion is moved away  $300\ \mu\text{m}$  from its normal position to prevent any collisions with the atoms during the final evaporation stage. This is done by changing one of the endcap voltages of the ion trap which moves the ion along the ion-trap axis ( $z$ -axis). The position of the optical dipole trap is controlled by moving the laser beams with the help of AOMs. (b) By switching back to the original endcap voltages, the ion is moved back within several ms to its original position where it can now probe the local density of the atomic cloud.

#### 2.4.6 Fine alignment of the crossed dipole trap

We control the position of the crossed dipole trap dynamically with the help of AOMs (see Fig. 2.12). For a typical AOM with a center frequency of 80 MHz the corresponding Bragg angle is about 10 mrad. Since the frequency bandwidth is on the order of 10%, the diffraction angle can be varied by about 1 mrad. For distances between the AOMs and the science chamber on the order of 1 m, this results in a shift of the ion trap position by up to 1 mm.

The relative position of the dipole trap relative to the ion trap can be accurately measured by again looking at atomic collisional losses as previously described in section 2.4.4. However, this time we use a single ion (see Fig. 2.12). In order to precisely control the interaction time of the ion with the atomic cloud, the ion is at first positioned about  $300\ \mu\text{m}$  away from its proper location so that it cannot interact with the atoms. This is done by changing one of the endcap voltages of the linear ion trap. This moves the ion along the axis of the ion trap ( $z$ -axis). Afterwards, the atom cloud is transported in from the BEC chamber and positioned by smoothly ramping the AOM frequencies. By quickly switching back the endcap voltages to their proper values, the ion moves back to its original position within 2 ms and starts colliding with the atoms, kicking them out of the trap. This procedure is illustrated

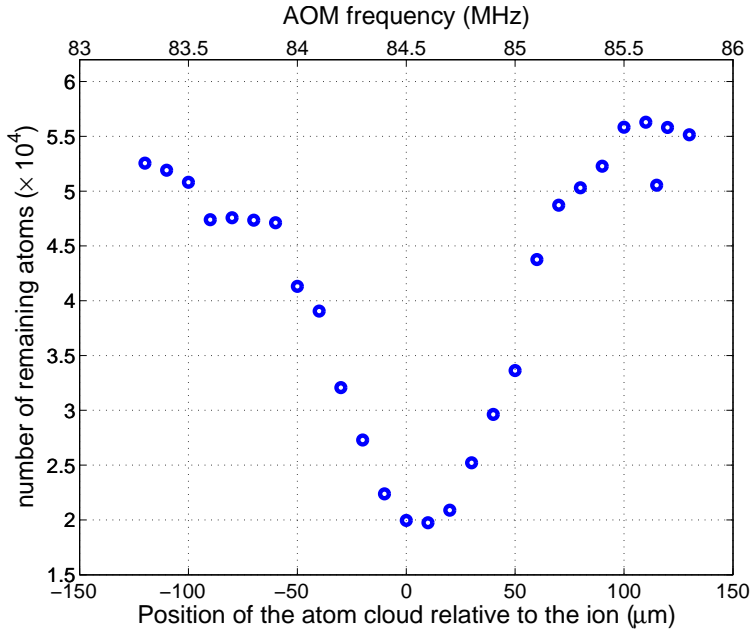


Figure 2.13: The number of remaining atoms after a given atom-ion interaction time of  $t = 1$  s. When the center of the atom cloud (i.e. the dipole trap) coincides with the position of the ion the number of remaining atoms is minimal (see also Ref. [16]). The position of the dipole trap is controlled by the drive frequency of AOMs. (Here the vertical beam of the crossed dipole trap is moved along the  $x'$ -direction.)

in Fig. 2.12. We then measure the atom loss as a function of the dipole trap position (i.e. the AOM frequencies). A typical curve is shown in Fig. 2.13 for an interaction time of about 1 s, working with a thermal cloud of initially  $5.5 \times 10^4$  atoms. Here, the same ion is used for all data points. (The micromotion of the ion was compensated to about 10 mK for these measurements.) The atom number reaches a minimum when the dipole trap is centered onto the ion. We can use this measurement to accurately overlap atom and ion trap along all three directions in space.

## 2.5 Summary

In conclusion, we have designed a hybrid vacuum apparatus which allows for cold collision experiments between ultracold neutral atoms and trapped, cold, single ions. A main feature of this apparatus is the spatial separation of production of the ultracold atomic cloud and the location where experiments take place, i.e. the linear ion trap. In order to transport the atoms to the ion trap, we use a novel efficient optical elevator consisting of a moving optical lattice which bridges a vertical gap of 30 cm within 1.5 s. The use of a vertical transport also leads to a non-standard design of

the BEC apparatus which houses a QUIC trap within a steel chamber. The overall layout of the apparatus is quite modular which has advantages in terms of stability and versatility, such that extensions can be added to the apparatus easily in the future. Also it helped to optimize the optical access to the region where ion-atom collision experiments take place. In addition to discussing the overall design we also describe various alignment and optimization procedures, e.g. accurate positioning of the atomic cloud onto the ion trap. First experiments with the apparatus [16] show promise for exciting research prospects in the future.

We would like to thank Rudi Grimm for generous support during the build-up phase. We are grateful to Michael Drewsen and the group of Rainer Blatt for advice on the design of the ion trap. We thank Wolfgang Limmer for thorough proofreading of the manuscript and help in editing. We thank Dennis Huss, Artjom Krükow, Andreas Brunner and Wolfgang Schnitzler for several technical improvements of the set-up. This work was supported by the Austrian Science Foundation (FWF) and the DFG within the SFB/ TR21. S.S. acknowledges support from the Austrian Academy of Sciences within the DOC doctoral research fellowship program.

# Chapter 3

## Dynamics of a cold trapped ion in a Bose-Einstein condensate

Physical Review Letters **105**, 133202 (2010)

Stefan Schmid<sup>1,2</sup>, Arne Härter<sup>1,2</sup>, and Johannes Hecker Denschlag<sup>1,2</sup>

<sup>1</sup>*Institut für Quantenmaterie und Center for Integrated Quantum Science and Technology IQ<sup>ST</sup>, Universität Ulm, 89069 Ulm, Germany*

<sup>2</sup>*Institut für Experimentalphysik und Zentrum für Quantenphysik, Universität Innsbruck, 6020 Innsbruck, Austria*

We investigate the interaction of a laser-cooled trapped ion ( $\text{Ba}^+$  or  $\text{Rb}^+$ ) with an optically confined  $^{87}\text{Rb}$  Bose-Einstein condensate (BEC). The system features interesting dynamics of the ion and the atom cloud as determined by their collisions and their motion in their respective traps. Elastic as well as inelastic processes are observed and their respective cross sections are determined. We demonstrate that a single ion can be used to probe the density profile of an ultracold atom cloud.

### 3.1 Introduction

The realization of a charged quantum gas, formed by laser-cooled, trapped ions and ultracold neutral atoms, offers intriguing perspectives for a variety of novel experiments. In addition to studying atom-ion collisions and chemical reactions in a regime where only one or few partial waves contribute, interesting phenomena such as charge transport in the ultracold domain [12], polaron-type physics [46, 47, 64],

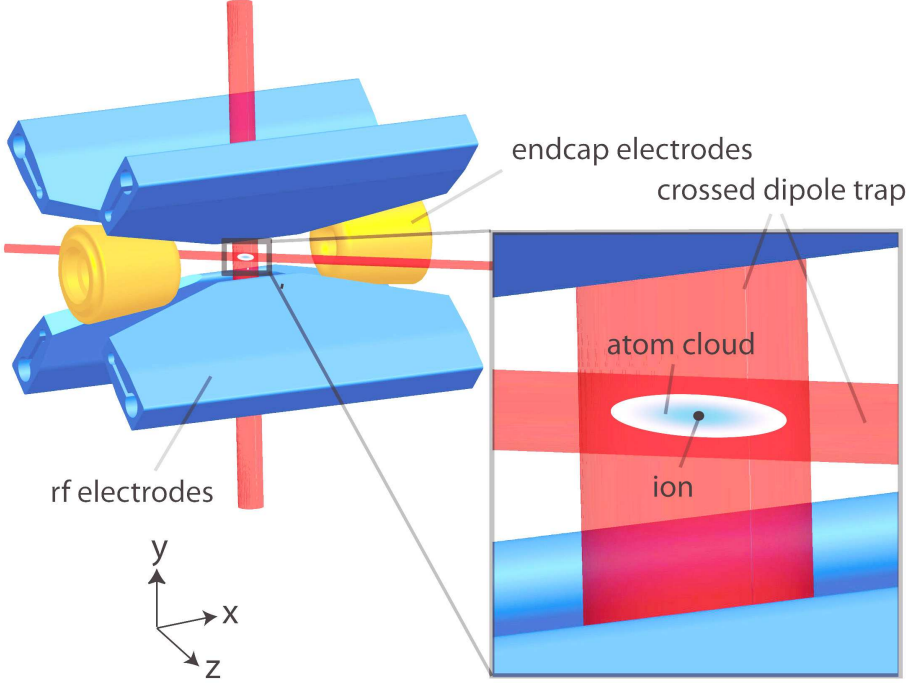


Figure 3.1: Combined atom-ion trap: A linear radiofrequency Paul trap is used to store ions [30], whereas the ultracold atoms are confined in a crossed optical dipole trap. By precisely overlapping the positions of these two traps, a single ion can be immersed into the center of the ultracold neutral atom cloud.

and novel atom-ion bound states [13] can be investigated. Further, the production of cold, charged molecules in a well-defined quantum state is an important goal in molecular physics [62, 63]. Techniques and tools that are widely used to control neutral atomic quantum gases, e.g. Feshbach resonances [87], may be employed in atom-ion collisions as well [39]. First observations of cold collisions with trapped atoms and ions in the mK regime have been made using  $\text{Yb}^+$  ions and a magneto-optical trap for Yb [14, 58] and very recently with a Bose-Einstein condensate ( $\text{Yb}^+$ ,  $\text{Rb}$ ) [15, 17]. Here we present our investigations where we use a defined small number of  $\text{Ba}^+$  or  $\text{Rb}^+$  ions which are immersed in an ultracold cloud of Rb atoms, which is either Bose-Einstein condensed or at sub- $\mu\text{K}$  temperature. The elastic cross sections are large as expected. Inelastic processes are in general strongly suppressed, which is important for planned future experiments. Charge transfer is directly identified in our experiments and found to be the dominant inelastic collision channel. As a first application we show how a trapped ion can be used to locally probe the density profile of a condensate. In our experiment we find the micromotion of the trapped ion to play an important role for the atom-ion dynamics.

In the inhomogeneous electrical field of an ion, a neutral atom is polarized and

attracted towards the ion. This interaction can be expressed as a long-range polarization potential  $V(r) = -C_4/2r^4$  with  $C_4 = q^2\alpha/4\pi\epsilon_0$ , where  $q$  is the charge of the ion and  $\alpha$  the dc polarizability of the atom. The characteristic radius of the potential is given by  $r^* = \sqrt{\mu C_4/\hbar^2}$ , where  $\mu$  is the reduced mass. For a  $^{87}\text{Rb}$  atom ( $\alpha = 4.7 \times 10^{-29} \text{ m}^3$  [88]) interacting with a  $^{138}\text{Ba}^+$  ion, this characteristic radius is  $r^* = 295 \text{ nm}$ . This is much larger than the typical length scale of the neutral atom-atom interaction potential as given by the van der Waals radius, which for  $^{87}\text{Rb}$  is  $R_{vdW} \approx 4 \text{ nm}$  [87]. For collision energies  $E$  above  $k_B \times 100 \mu\text{K}$ , the cross section for elastic scattering can be approximated by the semiclassical estimate  $\sigma_{\text{el}} = \pi(\mu C_4/\hbar^2)^{1/3}(1+\pi^2/16)E^{-1/3}$  [11]. At lower energies a full quantum mechanical treatment is necessary, which takes into account individual partial waves. In addition to elastic collisions, inelastic processes can also occur, such as charge transfer  $\text{Rb} + \text{Ba}^+ \rightarrow \text{Rb}^+ + \text{Ba}$  or molecule formation  $\text{Rb} + \text{Rb} + \text{Ba}^+ \rightarrow \text{Rb} + (\text{BaRb})^+$ .

## 3.2 Experimental setup

Here we present the first results obtained with our novel hybrid apparatus, where both species ( $\text{Ba}^+$ ,  $\text{Rb}$ ) are first trapped and cooled in separate parts of a UHV chamber in order to minimize mutual disturbance and are then brought together. We use a linear Paul trap into which we can load a well-defined number of  $^{138}\text{Ba}^+$  ions (typically 1) by photoionizing neutral Ba atoms from a getter source. Photoionization is done with a diode laser at 413 nm, which drives a resonant two-photon transition from the ground state to the continuum via the  $^3\text{D}_1$  state. The  $^{138}\text{Ba}^+$  ion which has no hyperfine structure is Doppler-cooled to mK temperatures using a laser at 493 nm. Another laser at 650 nm repumps from a metastable  $\text{D}_{3/2}$  state. The ion's fluorescence is collected with a lens of  $\text{NA} = 0.2$  and then detected using an electron multiplying charge-coupled device (EMCCD) camera. The linear Paul trap (see Fig. 1) consists of four blade electrodes, which are placed at a distance of 2 mm from the trap axis, and two endcap electrodes at a distance of 7 mm from the trap center. It is operated with a radiofrequency (rf) drive of  $\Omega = 2\pi \times 5.24 \text{ MHz}$  with an amplitude of  $1400 \text{ V}_{\text{pp}}$  and a dc endcap voltage of about 100 V. With these parameters we measure the axial and the radial trap frequencies to be  $\omega_{\text{I},\text{ax}} \approx 2\pi \times 80 \text{ kHz}$  and  $\omega_{\text{I},\text{rad}} \approx 2\pi \times 200 \text{ kHz}$ , respectively.

The sample of ultracold Rb atoms is prepared similarly as described in [89]. Atoms from a magneto-optical trap are magnetically transferred over a distance of 43 cm into a quadrupole Ioffe configuration (QUIC) trap. Evaporative cooling

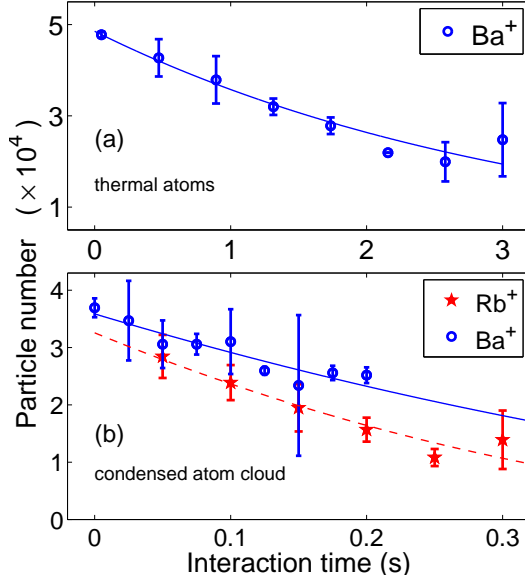


Figure 3.2: Number of remaining Rb atoms as a function of time as a sample of Rb atoms interacts with an ion. (a) A single  $\text{Ba}^+$  ion is immersed into the center of a thermal Rb cloud. The line is an exponential decay fit. (b) A single ion ( $\text{Ba}^+$  or  $\text{Rb}^+$ ) is immersed in a Rb Bose-Einstein condensate. The lines are fits based on our simple model described in the text.

yields a cloud of  $3 \times 10^6$   $^{87}\text{Rb}$  atoms in state  $|F = 1, m_F = -1\rangle$  at a temperature of about  $1\,\mu\text{K}$ . From the magnetic trap we load the atom cloud into a vertical 1-dimensional optical lattice trap formed by two counterpropagating laser beams (diameter  $\approx 500\,\mu\text{m}$ ) at a wavelength of 1064 nm with a total power of 2 W. We use the lattice as an elevator to transport the ultracold atoms upwards into the center of the Paul trap which is located 30 cm above the QUIC trap. The lattice is moved by changing the relative detuning of the two beams in a controlled manner [84]. The transport efficiency reaches more than 60%. During transport the depth of the lattice is sufficiently small ( $\approx k_{\text{B}} \times 10\,\mu\text{K}$ ) so that evaporation keeps the atom temperature at about  $1\,\mu\text{K}$ . After transport the atomic sample is loaded into a crossed optical dipole trap ( $\lambda = 1064$  nm). By lowering the trap depth, we evaporatively cool the atoms and end up with a BEC of about  $10^5$  atoms confined in a dipole trap with trap frequencies of about  $\omega_{\text{Rb}}^{(\text{x},\text{y},\text{z})} = 2\pi \times (60\,\text{Hz}, 60\,\text{Hz}, 8\,\text{Hz})$ . The condensate is detected via standard absorption imaging.

The BEC is initially located about  $300\,\mu\text{m}$  away from the ion. We move the ion within 2 ms along the Paul trap axis ( $x$  axis) into the BEC by changing the endcap voltages. The cooling lasers for the ion are switched off in order to ensure that the

ion relaxes into its electronic ground state  $|F = 1/2, m_F = \pm 1/2\rangle$  and to avoid changes in the atom-ion collision dynamics due to the cooling radiation.

### 3.3 Measurements of ion-induced atom loss

Initially the temperature of the ion is on the order of a few mK, which is much larger than the optical trap depth of about  $k_B \times 1 \mu\text{K}$ . Thus almost any collision with a cold atom leads to the atom being lost from the trap. As a consequence, one could naively expect, that the atom loss stops after a few collisions, once the ion is sympathetically cooled to atomic temperatures. However, when we measure the number of Rb atoms remaining in the trap as a function of the interaction time, we find a continuous loss of atoms (Fig. 2). It is the driven micromotion [74] of the rf trap, which is responsible for this continuing loss. In an atom-ion collision, energy can be redistributed among all motional degrees of freedom, enabling also the flux of micromotion energy to secular motion. After each collision, micromotion is quickly restored by the driving rf field. An equilibrium between the energy that is inserted by the driving field and the energy taken away by the lost atoms is reached within a few collisions. Thus the minimal temperature of a sympathetically-cooled ion stored in a rf trap is determined by the amount of micromotion of the ion [18]. Stray electric fields which shift the ion position away from the zero of the rf potential increase micromotion, leading to the so-called excess micromotion [74]. By applying dc electric fields along the radial direction this part of the micromotion is tunable.

Fig. 2 shows the elastic collision measurements with either (a) a thermal cloud of atoms (temperature  $T_{\text{Rb}} = 80 \text{ nK}$ , which is just above  $T_c$ ) or (b) a BEC. In the following we analyze these data in detail starting out with the case for thermal atoms. In general, the atom losses in our experiment are predominantly determined by atom-ion collisions. The lifetime of the atom sample without an ion being present exceeds 15 s. The loss of atoms is then described by  $\dot{N} = -\tilde{n}\sigma_{\text{el}}v_{\text{I}}$ , where  $\tilde{n}$  is the density of the atom cloud at the position of the ion,  $\sigma_{\text{el}}$  the elastic atom-ion cross section and  $v_{\text{I}}$  the velocity of the ion. In principle all three quantities are unknown. Based on our measurements and additional constraints of the following model we can still give estimates for them.

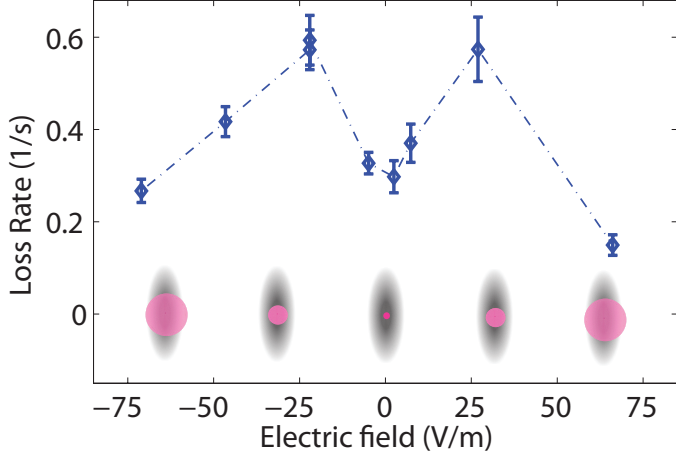


Figure 3.3: Loss rate of a thermal atom cloud when a static electric field is applied. In the presence of a field, the energy of the  $\text{Ba}^+$  ion and thus the amplitude of its secular motion are increased. As a result the sphere of depletion becomes larger, leading to an enhanced atom loss rate. For fields  $|\mathcal{E}_{\text{dc}}| > 30 \text{ V/m}$ , the amplitude of the secular motion is so large, that the ion spends a significant amount of time in a region of lower atom density. Therefore the loss rate decreases at high fields.

### 3.4 Simple model to estimate the ion energy

It is important to note that the density profile of the atom cloud is depleted locally due to the collisions with the well-localized ion. According to its mass  $m_I$ , energy  $E_I = m_I v_I^2 / 2$ , and trap frequency  $\omega_I$  the ion will be localized inside a region (which for simplicity we choose to be spherical) of radius  $r_0 = \sqrt{E_I / m_I \omega_I^2}$ . Inside this sphere we assume a homogeneous density  $\tilde{n}$ . Right outside the sphere, the density is given by  $n = N \bar{\omega}_{\text{Rb}}^3 (m_{\text{Rb}} / 2\pi k_B T_{\text{Rb}})^{3/2}$ , which is the peak density of a thermal cloud of Rb atoms (mass  $m_{\text{Rb}}$ ) confined in a harmonic trap with mean trap frequency  $\bar{\omega}_{\text{Rb}} = (\omega_{\text{Rb}}^{(x)} \omega_{\text{Rb}}^{(y)} \omega_{\text{Rb}}^{(z)})^{1/3}$ . The measured atom loss  $\dot{N}$ , which at  $t = 0$  is  $\dot{N} = 1.5 \times 10^4 \text{ s}^{-1}$  (as can be read off from Fig. 2), must match the net flux of atoms into the “sphere of depletion”, leading to the balance condition  $\dot{N} = \pi r_0^2 (n - \tilde{n}) v_{\text{th}}$ . Here the thermal velocity of the atoms is given by  $v_{\text{th}} = \sqrt{k_B T_{\text{Rb}} / 8\pi m_{\text{Rb}}}$ . By setting  $\tilde{n} = 0$  in the balance condition we get a lower bound for the ion energy, which for our parameters is equal to  $k_B \times 17 \text{ mK}$ . We can also estimate an upper limit of the ion energy from our method of compensating micromotion. The compensation is based on minimizing the position shift of the ion when the rf amplitude is changed. With this method we can reduce the DC electric field at the position of the ion to below  $4 \text{ V/m}$ , corresponding to a maximum ion energy of  $k_B \times 40 \text{ mK}$  [74]. By taking the midpoint between the two bounds we estimate the ion energy to be about  $k_B \times 30 \text{ mK}$ . Plugging this energy



Figure 3.4: *Left:* Fluorescence image of two  $\text{Ba}^+$  ions. *Right:* Fluorescence of one  $^{138}\text{Ba}^+$  next to an unknown dark ion. We infer the existence of the dark ion from the position of the  $\text{Ba}^+$ .

into the expressions above we get  $r_0 \approx 1.45 \mu\text{m}$  and a density of  $\tilde{n} \approx 0.45 n$ . Moreover we can determine the cross section  $\sigma_{\text{el}}$  to be  $1.9 \times 10^{-14} \text{ m}^2$ . This value is in rough agreement with the semiclassical estimate  $\sigma_{\text{el}}^{\text{semi}} = 9 \times 10^{-15} \text{ m}^2$ .

A slightly different analysis has to be done for the measurement with the BEC shown in Fig. 2(b). Again, collisions of the atoms with the trapped ion will lead to a sphere of depletion within the condensate. However, the flux of atoms into the sphere is now driven by mean field pressure rather than thermal motion. From numerical calculations using a 3D Gross-Pitaevskii equation with an absorptive (imaginary) potential term, we find that the flux into the sphere can be approximated by  $4\pi r_0^2 \tilde{n} v_e$ , as long as  $\tilde{n} \gtrsim 0.1 n$ . Here  $v_e = 4\hbar\sqrt{2\pi a(n - \tilde{n})}/m_{\text{Rb}}$  is the velocity with which the atoms enter the sphere,  $a = 5.61 \text{ nm}$  is the Rb-Rb s-wave scattering length and  $n = (15m_{\text{Rb}}^3 \bar{\omega}_{\text{Rb}}^3 N/\hbar a^{3/2})^{2/5}/8\pi$  is the peak density of the condensate. By equating the net flux to the measured lossrate of the BEC at  $t = 0$ ,  $\dot{N} = 8 \times 10^4 \text{ s}^{-1}$  (see Fig. 2), we find that the ion energy has to be larger than  $k_{\text{B}} \times 1 \text{ mK}$ . Our analysis shows, that on the other hand the ion energy has to be smaller than in the thermal case. Indeed, to minimize the temperature of the trapped ion, a comparatively large effort was made to compensate micromotion for the experiments with the BEC. Given that  $\sigma_{\text{el}}/\sigma_{\text{el}}^{\text{semi}} \approx 2$  as in the thermal case, our data suggests a reasonable ion energy of about  $k_{\text{B}} \times 5 \text{ mK}$ . This implies  $r_0 \approx 0.8 \mu\text{m}$ , a density of  $\tilde{n} \approx 0.1 n$  and a cross section of  $\sigma_{\text{el}} \approx 3.1 \times 10^{-14} \text{ m}^2$ . We also measured the loss rate for a single  $\text{Rb}^+$  ion and found it to be about the same as with  $\text{Ba}^+$  (Fig. 2). This is not surprising, since the atom loss rate depends only weakly on the ionic mass and the inner structure of the ion is irrelevant in the semiclassical regime.

When we intentionally increase the dc electric field  $\mathcal{E}_{\text{dc}}$ , we expect the atom loss rate to rise for two reasons. First, the atom-ion scattering rate rises as  $|\mathcal{E}_{\text{dc}}|^{1/3}$  (see also [15]), second, as the sphere of depletion increases its depletion is reduced. Figure 3 shows an increase of the loss rate up to an electric field of  $\mathcal{E}_{\text{dc}} \approx 30 \text{ V/m}$ , where the amplitude of the ion's secular motion is  $r_0 \approx 20 \mu\text{m}$ . This value is comparable to

the size of the atom cloud, which has an extension of about  $15\text{ }\mu\text{m}$  along the radial and  $80\text{ }\mu\text{m}$  along the axial direction. The model of a well-localized ion and a sphere of depletion is clearly no longer valid in this regime. We explain the decrease of the atom loss rate for even higher fields by the fact that the ion spends a significant amount of time in regions of lower atom density.

### 3.5 Inelastic processes

In addition to the elastic processes discussed so far, we have also investigated inelastic atom-ion collisions. For this we load two  $^{138}\text{Ba}^+$  ions into the ion trap. Typically after a time corresponding to  $10^4\text{-}10^5$  elastic atom-ion collisions, the fluorescence of one of the  $\text{Ba}^+$  ions is lost (Fig. 4). Since the position of the remaining bright  $\text{Ba}^+$  ion does not change, we infer that the other  $\text{Ba}^+$  ion has been replaced by an unknown dark ion formed in a reaction. We can determine the mass  $m_I$  of the dark ion by measuring the radial trap frequency. For this we modulate the amplitude of the rf voltage. When the modulation frequency is close to the trap frequency the ion motion is resonantly excited and a drop of the  $\text{Ba}^+$  fluorescence signal is observed. We only observe two resonance frequencies at 245 kHz and 400 kHz.  $\text{Ba}^+$  gives rise to the resonance at 245 kHz (which simply equals the  $\text{Ba}^+$  trap frequency that was chosen for these particular measurements). Since the radial trap frequency scales as  $1/m_I$  [30] (and since there is comparatively weak coupling between the ions due to  $\omega_{I,\text{ax}} \ll \omega_{I,\text{rad}}$ ), the 400 kHz resonance corresponds to the mass of  $^{87}\text{Rb}^+$ . We conclude that the dominant inelastic process in our system is the charge transfer process  $\text{Rb} + \text{Ba}^+ \rightarrow \text{Rb}^+ + \text{Ba}$  with a cross section  $\sigma_{\text{ch.ex.}}$  ranging between  $10^{-19}\text{ m}^2$  and  $10^{-18}\text{ m}^2$ . So far we have not observed the formation of molecular ions. Our charge transfer results are comparable to the ones observed for the heteronuclear case of  $(\text{Rb}, \text{Yb}^+)$  [17]. Homonuclear charge transfer rates are orders of magnitudes higher [14]. In our case the charge transfer is predicted to be dominantly radiative, where a photon carries away most of the 1 eV of energy released in this reaction [90].

### 3.6 The ion as a local density probe for atomic samples

We now show how a single ion may be used to locally probe the atomic density distribution. By controlling the endcap voltage we vary the position of the single  $\text{Rb}^+$

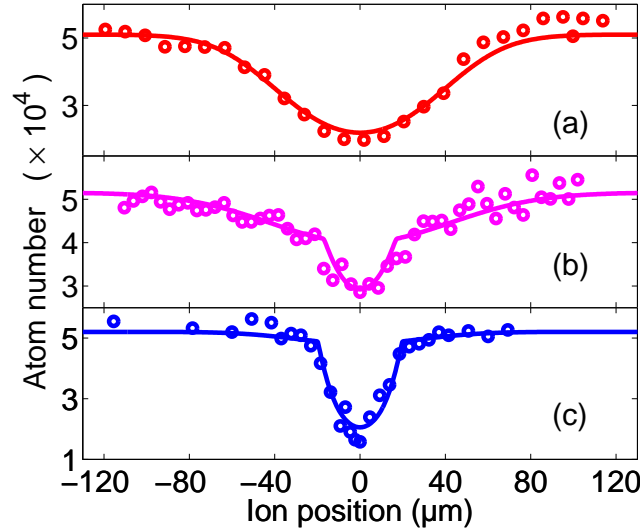


Figure 3.5: Number of Rb atoms remaining in the trap depending on the position of the  $\text{Rb}^+$  ion relative to the center of the atom cloud. The measurement is performed with (a) a thermal cloud, (b) a partially condensed cloud and (c) an almost pure Bose-Einstein condensate. The interaction time was (a) 1.5 s, (b) 1 s and (c) 0.5 s. The solid lines are fits, where the ion energy  $E_I$  and the atom temperature  $T_{\text{Rb}}$  are used as free fit parameters.

ion relative to the atom sample. At each position  $x$  the atom loss is measured on a freshly prepared atom cloud for a given interaction time (Fig. 5). The measurement is performed for three different condensate fractions. We can theoretically reproduce the data shown in Fig. 5 with our model, which demonstrates our quantitative understanding of the dynamics. For this we write the total atom loss of a partly condensed cloud as a sum of the individual losses from the BEC and the thermal cloud as discussed before. For numerical calculations we choose  $\sigma_{\text{el}} = 3 \times 10^{-14} \text{ m}^2$  and make use of the well-known density profiles for a thermal and a condensed atom cloud confined in a harmonic trap. The thermal component and BEC are in equilibrium and obey  $N_c/N = 1 - (T_{\text{Rb}}/T_c)^3$  where  $T_c$  is the critical temperature and  $N_c/N$  is the condensate fraction which changes with time. The temperature  $T_{\text{Rb}}$  of the atomic sample is constant, as determined by the optical trap depth. It is used as a free fit parameter in our model together with the ion energy  $E_I$ , which we keep fixed for all three measurements. Fig. 5 depicts the total number of remaining particles  $N(x)$  as a function of the ion's position  $x$ . The values for  $T_{\text{Rb}}$  obtained from the fit (a) 50 nK, (b) 35 nK and (c) 25 nK are in nice agreement with the temperatures determined separately in time-of-flight measurements. Moreover the fit suggests  $E_I \approx k_B \times 14 \text{ mK}$ , which

is in the same range as the temperatures found in the Ba<sup>+</sup> experiments. The ion probe features a spatial resolution on the  $\mu\text{m}$  scale and has advantages compared to absorption imaging which integrates over the line of sight.

In conclusion we have immersed cold trapped ions in a sea of ultracold neutral atoms in a novel hybrid apparatus with high spatial and temporal control. We have investigated the dynamics of the (Ba<sup>+</sup>, Rb) system in the mK regime and have extracted elastic and inelastic collision properties. In our present setup the collision energies are determined by the ionic excess micromotion, which we plan to minimize for future experiments in the ultracold regime.

The authors would like to thank Albert Frisch and Sascha Hoinka for their help during the early stage of the experiment and Thomas Busch, Tommaso Calarco, Robin Côté, Bretislav Friedrich, Bo Gao, Zbigniew Idziaszek, Tobias Schätz, Wolfgang Schnitzler, and Jaques Tempere for helpful discussions and support. We are grateful to Rudi Grimm for generous support and to Michael Drewsen and the group of Rainer Blatt for advice on the design of the ion trap. This work was supported by the Austrian Science Fund (FWF). S.S. acknowledges support from the Austrian Academy of Sciences within the DOC doctoral research fellowship program.

# Chapter 4

## Improved view on atom-ion dynamics and atom-based compensation of ion micromotion

Ion micromotion has proven to be of central importance for the understanding of our atom-ion experiments so far. Since it is constantly driven by the oscillating electric fields of the trap, it maintains a certain energy scale which is generally dominant when working with ultracold atomic ensembles.

I will provide a summary of experimental and theoretical investigations of micromotion and the resulting dynamics in atom-ion experiments. Micromotion issues in our experiment were also the central topic of the master's thesis (Diplomarbeit) of A. Brunner [91]. For those aspects of this topic that are covered in his work I will keep the discussion concise and give the corresponding reference.

In this chapter, I will first introduce an analytical model for ion micromotion without collisions with neutral atoms. To apply this model to an ion in an ultracold atom cloud I will then present numerical simulations from which ionic and atomic dynamics can be predicted and compared to experimental data. With this good understanding of the relevance of different experimental parameters I will then show results of micromotion compensation measurements based on the interaction with neutral atom clouds. Finally, technical and more fundamental limits to the attainable ion energies will be discussed.

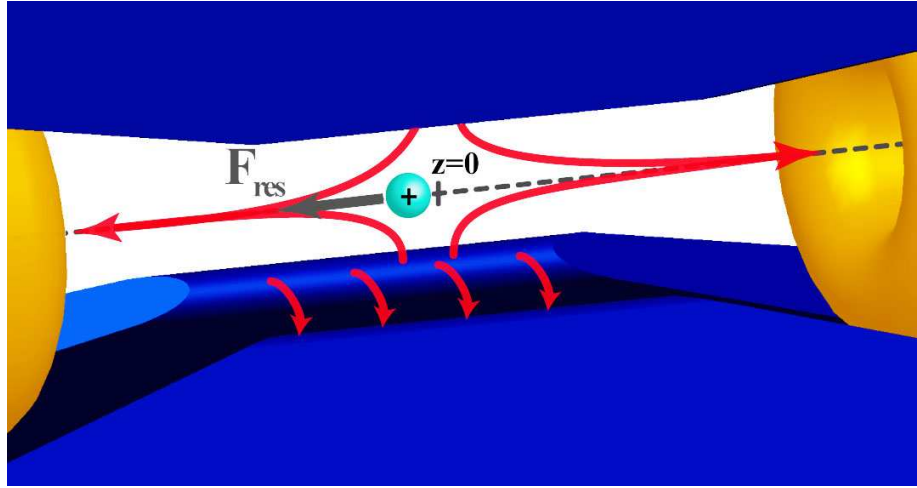


Figure 4.1: Illustration of the field configuration in our Paul trap. To a large part, the electric field lines (red) originating at the rf blades (blue) end at the adjacent rf blades which are at ground potential. However, a considerable part of the field lines extends to the endcap electrodes (gold). As a result, the ion experiences a three-dimensional rf trapping effect and also undergoes micromotion oscillations in all three dimensions.

## 4.1 Improved model of ion micromotion

In chapters 2 and 3 the sources of ion excess micromotion and the resulting challenges for atom-ion experiments have been briefly discussed. Here, I will lay a more solid groundwork and present an improved model that allows for a good understanding of the experimentally relevant parameters. The model expands the concepts of ref. [74] and is described in more detail in ref. [91].

In linear Paul traps, three-dimensional confinement of the ion is achieved by a combination of static axial confinement and radial confinement through rf fields (see e.g. [29–31]). However, both of these confinement techniques have effects in all three spatial dimensions. In the common treatment of linear Paul traps, the effect of the static field in radial direction is included while the implications of the rf fields in axial direction are neglected. However, in our experiments, the latter point becomes important. In part, this is due to the design of our trap (see Fig. 2.7) in which the axial distance from the trap center to the endcap electrodes measures  $Z_0 = 7$  mm and the radial distance to the rf electrodes  $R_0 = 2.3$  mm. Hence, both dimensions are of the same order of magnitude (see Fig. 4.1). We can expect rf field lines that originate from one of the rf electrodes to end primarily on the adjacent rf electrodes which are held at ground potential. However, a significant fraction of the field lines also ends on the two endcap electrodes. Fig. 4.1 illustrates the effect of such a field

configuration on an ion that is axially shifted from the trap center. At a given point in time, the electric fields (red) from the rf blades have a component in axial direction and thus exert a resulting force  $F_{\text{res}}$  on the ion. As the rf voltage oscillates, the ion will be subjected to oscillating rf fields along the axis of the trap resulting in an axial trapping effect with secular motion and micromotion, completely analogous to the trapping effect in the radial directions. We have therefore expanded the usual treatment of linear Paul traps to incorporate the effect of axial rf trapping.

In this treatment, the time-dependent Paul trap potential at a drive frequency  $\Omega_D$  is expressed as

$$V(x, y, z, t) = \frac{V_0}{2} \left[ \left( 1 + \frac{x^2 - y^2}{R'_{\text{rad}}^2} - \frac{z^2}{R'_z^2} \right) \cos(\Omega_D t) \right]. \quad (4.1)$$

Here,  $V_0$  is the amplitude of the rf voltage and  $R'_{\text{rad}} = 2.6 \text{ mm} \approx R_0$  the effective radial extension of the trap. The parameter  $R'_z$  depends on the axial geometry of the trap and determines the strength of the axial rf forces acting on the ion. The value of  $R'_z$  is correlated to  $Z_0$ , the distance from the trap center to the endcap electrodes, but it also depends on the exact shape of the trap electrodes. Thus, to determine  $R'_z$  we employ numerical simulations using the *Essential Numerical Tools* program developed by K. Singer et al. [92]. This software package allows us to simulate ion trajectories taking into account the full three-dimensional geometry of our trap. By fitting the simulation results to known experimental quantities (trap frequencies or applied electrode voltages) we find the effective axial dimension to be  $R'_z = 12.5 \text{ mm}$ . In addition to the oscillating potential described by equation 4.1, the static potential created by voltages  $U_0$  on the endcap electrodes is

$$U(x, y, z) = \frac{\kappa U_0}{Z_0^2} [z^2 - \frac{1}{2}(x^2 + y^2)], \quad (4.2)$$

where  $\kappa$  parametrizes the strength of the static electric fields originating from the endcap electrodes at a given voltage. In our trap we have  $\kappa \approx 0.294$  [93]. The equation of motion of an ion subjected to the total potential  $V(x, y, z, t) + U(x, y, z)$  is the Mathieu equation

$$\frac{\partial^2 r_i}{\partial t^2} + (a_i + 2q_i \cos(\Omega_D t)) \frac{\Omega_D^2}{4} r_i = 0, \quad (4.3)$$

where  $i$  can take values  $(x, y, z)$  and  $r_i$  are the corresponding positions of the ion.

The parameters  $a_i$  and  $q_i$  are given by

$$a_x = a_y = -\frac{a_z}{2} = -\frac{4e\kappa U_0}{m_{\text{ion}} Z_0^2 \Omega_D^2} \quad (4.4)$$

and

$$q_x = -q_y = -\left(\frac{R'_z}{R'_{\text{rad}}}\right)^2 q_z = \frac{2eV_0}{m_{\text{ion}} R'^2_{\text{rad}} \Omega_D^2}. \quad (4.5)$$

Comparing the quantities  $R'_{\text{rad}}$  and  $R'_z$ , we thus find the Mathieu parameter in axial direction to be significantly smaller than in the radial directions ( $q_z \approx 0.04 q_y$ ). In a typical experimental setting we have  $q_y \approx 0.2$  and therefore  $q_z \approx 0.008$ .

In a realistic experimental situation, the ion will experience additional forces, e.g. due to stray electric fields, that displace the ion from the trap center by distances ( $\Delta r_x, \Delta r_y, \Delta r_z$ ). Solving equation 4.3 under these conditions results in an ion trajectory

$$u_i(t) = \Delta r_i + r_{\text{sec},i} \cos(\omega_{\text{ion},i} t + \varphi_i) [1 + \frac{q_i}{2} \cos(\Omega_D t)] + \Delta r_i \frac{q_i}{2} \cos(\Omega_D t). \quad (4.6)$$

Here, we have introduced the secular oscillation frequencies

$$\omega_{\text{ion},i} = \frac{\Omega_D}{2} \sqrt{a_i + \frac{1}{2} q_i^2} \quad (4.7)$$

and corresponding amplitudes  $r_{\text{sec},i}$ . The last term of equation 4.6 describes the excess micromotion that is due to the displacements of the ion from the trap center. In our experiments, the dominant energy scale is typically set by this excess micromotion making it a quantity of central importance to the atom-ion interactions observed. Its energy contribution is given by

$$E_{\text{eMM},i} = \frac{m_{\text{ion}}}{16} \cdot (q_i \Omega_D \Delta r_i)^2. \quad (4.8)$$

We now want to derive the sensitivity of the excess micromotion energy with respect to a stray electric field  $\vec{\varepsilon}$ . Under typical experimental conditions ( $\Omega_D = 2\pi \times 4.17 \text{ MHz}$ ,  $V_0 = 500 \text{ V}$ ,  $U_0 = 8 \text{ V}$ ), a  $^{138}\text{Ba}^+$  ion is confined at trapping frequencies  $\omega_{\text{Ba},x} \approx \omega_{\text{Ba},y} = 2\pi \times 220 \text{ kHz}$  and  $\omega'_{\text{Ba},z} = 2\pi \times 40 \text{ kHz}$ , where  $\omega'_{\text{Ba},z}$  denotes the total axial trap frequency including static and rf confinement effects. This results in excess micromotion energies

$$E_{\text{eMM},i} = c_i \varepsilon_i^2 \quad (4.9)$$

with  $c_x \approx c_y \approx 2.15 \frac{k_{\text{B}} \cdot \text{mK}}{(\text{V}/\text{m})^2}$  and  $c_z \approx 3.7 \frac{k_{\text{B}} \cdot \text{mK}}{(\text{V}/\text{m})^2}$ . Somewhat surprisingly, the elec-

tric field sensitivity of the axial micromotion energy is significantly higher than the corresponding radial quantity. This can be understood when comparing the displacements of the ion at a given electric offset field

$$\Delta r_i = \frac{e}{m_{\text{Ba}} \omega_{\text{Ba},i}^2} \varepsilon_i = d_i \varepsilon_i, \quad (4.10)$$

where  $d_x \approx d_y \approx 0.36 \frac{\mu\text{m}}{\text{V/m}}$  and  $d_z \approx 11 \frac{\mu\text{m}}{\text{V/m}}$ . Clearly, due to the weak axial confinement, small electric fields can massively shift the ion away from the rf minimum leading to large amounts of excess micromotion in this direction. The obvious cure for this issue is to increase the voltages on the endcap electrodes to confine the ion more strongly. In the experiments presented in this work, these voltages were limited by the digital-to-analog-converter supplying our endcaps. An amplified version of this device is currently being tested and will be installed in the near future. The achievable almost tenfold increase in endcap voltage should then reduce  $d_z$  by almost an order of magnitude so that  $E_{\text{eMM},z} \propto d_z^2$  turns into a minor contribution to the total ion energy. It should be kept in mind that increasing the static confinement too much results in anti-trapping potentials in the radial directions which lead to increased radial micromotion. The optimal setting depends on the specific trap design used.

An alternative way to eliminate axial micromotion is the usage of a symmetric rf drive configuration. In such a configuration, all four rf blades carry rf voltages. Opposing blades are driven in-phase, adjacent blades out-of-phase. In this way, the electric field lines in axial direction (see Fig. 4.1) originating from one pair of opposing rf electrodes will be compensated by the other pair of rf electrodes driven with opposite phase. The symmetric configuration can thus suppress axial micromotion by several orders of magnitude. As a further advantage, for a given rf voltage  $V_0$ , the voltage difference between adjacent blades is doubled. This leads to a corresponding increase in the radial trapping effect. First attempts to implement a symmetric trap drive in our experiment suffered from very high ion heating rates, possibly due to the increased complexity of the employed ferrite-toroid transformer (similar to the one shown in Fig. 2.6). We are currently developing an improved design. Further details on this topic can be found in [91].

For an ion of mass  $m_{\text{ion}}$  the excess micromotion energies can be calculated from the corresponding expressions for  $\text{Ba}^+$  using

$$E_{\text{eMM},i} = \frac{m_{\text{ion}}}{m_{\text{Ba}}} E_{\text{eMM},i}^{Ba} \quad (4.11)$$

for the radial directions and

$$E_{\text{eMM},z} = \frac{m_{\text{Ba}}}{m_{\text{ion}}} E_{\text{eMM},z}^{Ba} \quad (4.12)$$

in axial direction when assuming that the static axial confinement is significantly stronger than the axial rf confinement. When keeping the trap settings constant, a  $^{87}\text{Rb}^+$  ion will thus undergo less radial micromotion and more axial micromotion than a  $^{138}\text{Ba}^+$  ion.

The derivations and discussions given on the last few pages can be cast into a form which expresses the excess micromotion energy directly in terms of the experimentally tunable parameters  $\Omega_D$ ,  $V_0$  and  $U_0$ . Using equations 4.4, 4.5, 4.7 and 4.10 we can rewrite equation 4.8 as

$$E_{\text{eMM},i} = \frac{1}{m_{\text{ion}}} \cdot \left( \frac{2e\varepsilon_i V_0}{R_i'^2 \Omega_D \cdot (4\chi_i \kappa U_0 / Z_0^2 + eV_0^2 / (m_{\text{ion}} R_i'^4 \Omega_D^2))} \right)^2. \quad (4.13)$$

Here,  $\chi_z = -2$ ,  $\chi_x = \chi_y = 1$  and  $R'_i = R'_{\text{rad}}$  for  $i = x, y$ . The total excess micromotion energy in a given Paul trap is given by

$$E_{\text{eMM,tot}} = \sum_{i=x,y,z} E_{\text{eMM},i} \quad (4.14)$$

and can thus be minimized by adjusting the drive frequency  $\Omega_D$  and the voltages  $V_0$  and  $U_0$ . In addition, further constraints like the stability of the trap configuration and the total trap depth need to be considered.

## 4.2 The differential atom-ion interaction cross section

The previous section introduced an improved model to understand ion micromotion in an isolated environment of a Paul trap. Additional complexity arises in our experiments through atom-ion collisions which lead to perturbations of the ion's trajectory. As a first step towards these collision dynamics, I will discuss the characteristics of the atom-ion differential collision cross section  $\frac{d\sigma_{ai}}{d\theta} \equiv \frac{d\sigma}{d\theta}$ <sup>1</sup>. It contains the information on the azimuthal angular distribution of the scattering processes and thus determines how the energy transfer between the ionic and atomic collision partners

---

<sup>1</sup>For improved readability, I have dropped the index ai used in previous chapters when referring to the differential cross section.

takes place.

To calculate  $\frac{d\sigma}{d\theta}$  I will closely follow the derivation given in Ref. [20]. In brief, we perform a partial wave analysis of the wave function yielding

$$\frac{d\sigma}{d\theta} = \frac{2\pi}{k^2} \left| \sum_{l=0}^{\infty} (2l+1) e^{i\eta_l} \sin \eta_l P_l(\cos \theta) \right|^2 \sin \theta . \quad (4.15)$$

Here,  $\hbar k$  is the collision momentum,  $l$  is the angular momentum quantum number,  $\eta_l$  is the scattering phase and  $P_l(\cos \theta)$  are the Legendre polynomials. For sufficiently large angular momenta, scattering occurs off the centrifugal barrier and the phase shifts can be estimated semiclassically by [11]

$$\eta_l = \frac{\pi \mu^2 C_4 E_{\text{col}}}{4 \hbar^4 l^3} . \quad (4.16)$$

We can apply this estimation for angular momenta with quantum numbers  $l > l_{\min} = \frac{1}{\hbar} (8\mu^2 C_4 E_{\text{col}})^{\frac{1}{4}}$  with  $E_{\text{col}}$  the collision energy. For  $l < l_{\min}$  the scattering phase depends on the details of the short-range atom-ion potential and cannot be described in a simple analytical expression. We therefore assume these phase shifts to be randomly distributed on the interval  $[0, 2\pi)$ . For the calculation of  $\frac{d\sigma}{d\theta}$  using equation 4.15 we average over 100 random sets of phase shifts for  $l < l_{\min}$  and employ the semiclassical formula 4.16 for  $l > l_{\min}$ .

In Fig. 4.2 the resulting differential cross sections are shown for homonuclear scattering of Rb and Rb<sup>+</sup> and for collision energies between  $10\mu\text{K}\cdot k_{\text{B}}$  and  $\sim 10\text{K}\cdot k_{\text{B}}$ . Two main characteristics are of central importance to the understanding of the atom-ion collision dynamics. Firstly, the magnitude of the cross section increases as the collision energy decreases. This is not surprising and in line with the semiclassical formula 1.5 describing the total cross section  $\sigma_{\text{ai}}$ . Secondly, the scattering is dominated by glancing collisions occurring at small angles  $\theta$ . As the collision energy increases, the corresponding peak in Fig. 4.2 shifts to smaller  $\theta$  and becomes even more pronounced (best seen in the double-logarithmic plot on the right). Consequently, even in the case of homonuclear collisions, the average energy transfer between the collision partners will be much smaller than the collision energy. At high enough initial collision energies it may therefore take thousands of collisions until a thermal equilibrium is reached.

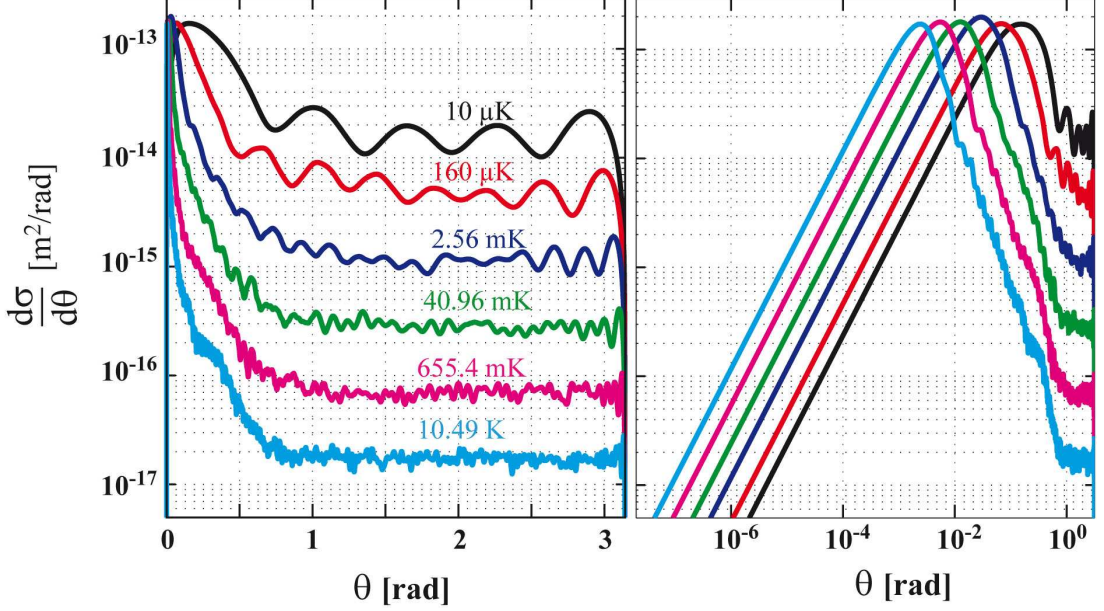


Figure 4.2: Logarithmic (left) and double-logarithmic (right) plot of the differential cross section  $\frac{d\sigma}{d\theta}$  for collision energies  $E_{\text{col}}$  between  $10 \mu\text{K}\cdot k_{\text{B}}$  and  $10.49 \text{ K}\cdot k_{\text{B}}$ . With increasing  $E_{\text{col}}$  the total cross section decreases and the scattering is more and more dominated by glancing collisions resulting in small angle deflections.

### 4.3 Simulation of ion dynamics in an atom cloud

We now want to use the acquired knowledge about the differential atom-ion cross section to simulate the collision dynamics in a realistic scenario. In this context, it is crucial to include the atomic and ionic trapping conditions, most importantly the effects of ion micromotion. The simulation discussed here builds upon the approach described in ref. [20]. Similar to the simple estimates presented in chapter 3 we can define the atom-ion scattering rate

$$\Gamma(t) = n_{\text{at}}(\vec{r}_{\text{ion}})\sigma_{\text{ai}}(E_{\text{col}})v_{\text{ion}}(t), \quad (4.17)$$

where we use the local atomic density at the position of the ion  $n_{\text{at}}(\vec{r}_{\text{ion}})$ , the energy dependent collision cross section  $\sigma_{\text{ai}}(E_{\text{col}})$  and the instantaneous ionic velocity  $v_{\text{ion}}(t)$ . The position of the ion is determined by its oscillation in the secular potential at trapping frequencies  $(\omega_{\text{ion},x}, \omega_{\text{ion},y}, \omega_{\text{ion},z})$  and can be written as

$$r_{\text{sec},i} = \frac{1}{\omega_{\text{ion},i}} \sqrt{\frac{2E_i}{m_{\text{ion}}}} \sin(\omega_{\text{ion},i}t + \varphi_i). \quad (4.18)$$

Here,  $i$  can take values  $(x, y, z)$ ,  $E_i$  are the corresponding kinetic energies of the ion,  $m_{\text{ion}}$  denotes the ionic mass and  $\varphi_i$  the oscillation phases. The secular velocity  $\vec{v}_{\text{sec}} = \frac{d\vec{r}_{\text{sec}}}{dt}$  is then obtained by simple differentiation. In addition to the secular motion, the ion undergoes micromotion driven at the trap drive frequency  $\Omega_D$ . This motion can be divided into an inherent part connected to the secular oscillation of the ion and an excess part induced by external forces which shift the ion away from the nodal line of the rf fields. The total micromotion velocity can be expressed as

$$\vec{v}_{\text{mm}} = \begin{pmatrix} q_x \cdot (r_{\text{sec},x}(t) + \Delta r_x) \\ q_y \cdot (-r_{\text{sec},y}(t) - \Delta r_y) \\ q_z \cdot (r_{\text{sec},z}(t) + \Delta r_z) \end{pmatrix} \frac{\Omega_D}{2} \cos(\Omega_D t), \quad (4.19)$$

where  $(\Delta r_x, \Delta r_y, \Delta r_z)$  are the ion's positional offsets from the rf node. They are largely dominated by stray electric fields  $(\varepsilon_x, \varepsilon_y, \varepsilon_z)$  leading to offset values

$$\begin{pmatrix} \Delta r_x \\ \Delta r_y \\ \Delta r_z \end{pmatrix} = \frac{e}{m_{\text{ion}}} \begin{pmatrix} \varepsilon_x \omega_x^2 \\ \varepsilon_y \omega_y^2 \\ \varepsilon_z \omega_z'^2 \end{pmatrix}. \quad (4.20)$$

In the case of equal atomic and ionic masses, the secular velocity after an atom-ion collision is given by

$$\vec{v}_{\text{sec,f}} = \frac{1}{2} [\vec{v}_{\text{sec,i}} + \mathbf{R} \vec{v}_{\text{sec,i}} + (\mathbf{R} - \mathbf{1}) \vec{v}_{\text{mm}}], \quad (4.21)$$

where  $\mathbf{R}$  is a rotation matrix about the angles  $\theta$  and  $\phi$ . This equation contains the coupling between secular motion and micromotion and describes the core of atom-ion collision dynamics in a Paul trap. As the micromotion is constantly driven by the trap drive, it will quickly return to its original value after the collision. Depending on the oscillation phases at which the collision takes place, this leads to heating or cooling of the secular motion of the ion. The resulting dynamics give rise to non-Gaussian ion energy distributions featuring significant power-law tails towards high energies [19, 20].

The description given in this section is essentially identical to [20] with the exception of the  $z$ -components in equations 4.19 and 4.20 which we express using the  $q_z$  parameter, in complete analogy to the other components.

### 4.3.1 Simulation of the ion energy evolution

The simulation is now applied to an atom-ion experiment in which a single Rb<sup>+</sup> ion is immersed into an atomic Rb sample for an interaction time  $\tau = 8\text{s}$ . At the beginning of the interaction the atom number is  $N_{\text{at}} = 1.1 \times 10^4$ , the atomic temperature is  $T_{\text{at}} = 1.15\,\mu\text{K}$  and the atom trap frequencies are  $(\omega_{\text{at},x}, \omega_{\text{at},y}, \omega_{\text{at},z}) = 2\pi \times (136, 141, 40)\,\text{Hz}$ . This results in an atomic peak density of  $n_{\text{at}} = 1.16 \times 10^{11}\,\text{cm}^{-3}$ . The ion trap is driven at  $\Omega_D = 2\pi \times 4.17\,\text{MHz}$  and peak rf voltages of 500 V confining the ion at trap frequencies of  $(\omega_{\text{ion},x}, \omega_{\text{ion},y}, \omega_{\text{ion},z}) = 2\pi \times (350, 350, 70)\,\text{kHz}$ . In the simulation, the initial ion energy  $E_{\text{ion}} = E_x + E_y + E_z$  is set to  $6\,k_{\text{B}}\cdot\text{K}$ , a reasonable value as the single Rb<sup>+</sup> ion cannot be cooled by means other than the buffer gas cooling taking place through the atom-ion collisions. During the production cycle of an atomic sample ( $\sim 30\,\text{s}$ ), the ion can thus accumulate energy through trap-induced heating processes [94] or collisions with hot atoms or ions from the background gas.

Fig. 4.3 shows the simulated ion energy evolution for four different settings of the electric field  $\varepsilon_{\text{vert}} = \frac{1}{\sqrt{2}}(\varepsilon_x + \varepsilon_y)$  that we apply in vertical direction using the compensation electrodes. The field values are 4.03 V/m (black trace), 1.86 V/m (green), 0.62 V/m (red) and 0.01 V/m (blue). Further sources of ion micromotion such as rf pickup in the electrodes or a difference in the phases between opposing rf electrodes can lead to additional energy contributions that we summarize in a term  $E_{\text{res}}$ . In absence of more detailed information on the sources of this energy contribution, it is incorporated into the simulation as an additional radial displacement  $\Delta s_{\text{res}} = \sqrt{\frac{E_{\text{res}}}{m_{\text{ion}}\omega_{\text{ion},x}^2}}$  which is added to both  $\Delta r_x$  and  $\Delta r_y$ . Fig. 4.3a shows the result of a single simulation run with  $E_{\text{res}} = 600\,\mu\text{K}\cdot k_{\text{B}}$ . For the lowest electric field setting of 0.01 V/m,  $E_{\text{res}}$  clearly dominates over the field-induced micromotion energy. At all four simulated electric fields we find an initial cool-down time of the ion on the order of 1 s followed by irregular energy oscillations around a mean value correlated to the amount of excess micromotion. The energy variations span up to two orders of magnitude and can occur on timescales of 0.1 s. Such fluctuations are in line with the predictions of energy distributions broadened by high energy power-law tails. In Fig. 4.3b the simulation result has been smoothed by averaging over 100 simulation runs. The initial cool-down phase requires roughly between 0.8 s and 1.4 s depending on the final energy level that is set by the amount of excess micromotion. This observation contradicts the assumption in ref. [20] that the initial ion energy is irrelevant to the observable atom-ion dynamics. In fact, simulation runs starting with ion energies at room temperature (300 K) often do not show any cooling within the interaction time  $\tau$ . To understand this effect we can estimate the typical amplitude

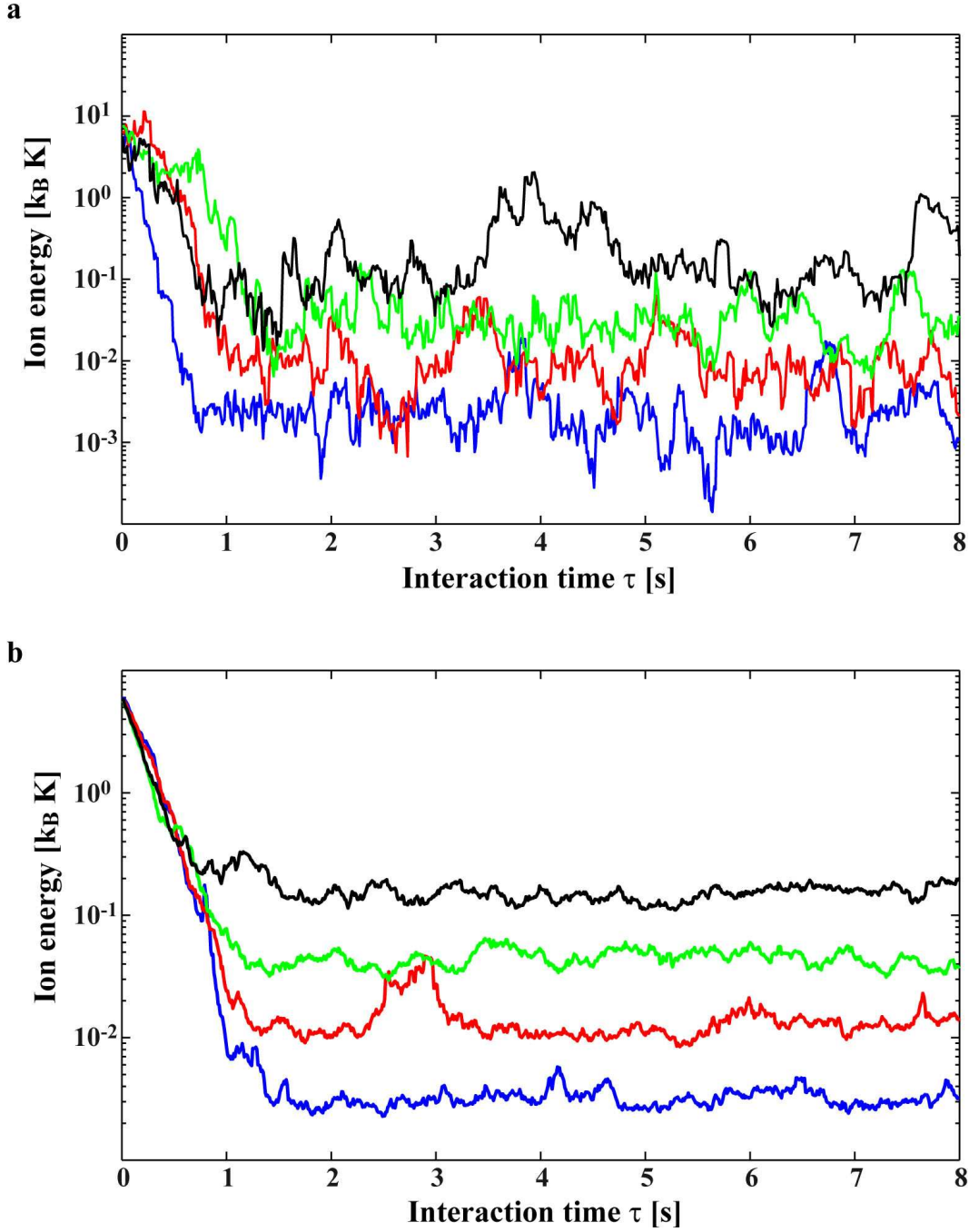


Figure 4.3: Energy evolution of a Rb<sup>+</sup> ion immersed into an atomic Rb sample. The simulation was performed for four electric field settings of 4.03 V/m (black trace), 1.86 V/m (green), 0.62 V/m (red) and 0.01 V/m (blue). The corresponding ion excess micromotion energies are 29.7 mK · k<sub>B</sub>, 8.6 mK · k<sub>B</sub>, 2.2 mK · k<sub>B</sub> and 0.62 mK · k<sub>B</sub> (assuming a residual energy contribution of  $E_{\text{res}} = 0.6 \text{ mK} \cdot k_{\text{B}}$ ). **(a)** shows the result of a single run of the simulation while **(b)** shows the average over 100 simulation runs.

of ion motion

$$r_{\max} = \sqrt{\frac{E_{\text{ion}}(300 \text{ K})}{m_{\text{ion}} \bar{\omega}_{\text{ion}}^2}} \gtrsim 100 \mu\text{m},$$

where  $\bar{\omega}_{\text{ion}}$  is the geometrical mean of the ion trap frequencies. This amplitude is much larger than the extensions of the atom cloud which range between 10 and 30  $\mu\text{m}$ . Thus, the ion rarely penetrates the atomic sample and due to the small collision cross sections at high energies the sympathetic cooling effect is negligible. As a consequence of these slow thermalization timescales, the atom-ion interaction becomes highly sensitive to rare but strong heating effects such as collisions with the background gas or chemical reactions within the atomic sample (see chapter 5). After the initial cool-down phase the mean ion energy is found to be roughly 5 times as large as the energy of the corresponding excess micromotion (see equation 4.9). This result agrees with the predictions made in [20] for homonuclear atom-ion collisions.

### 4.3.2 Simulation of the effect on the atomic sample

In a next step, we include the evolution of the atomic sample into the discussion. In a collision with the ion, an atom will typically gain an amount of kinetic energy  $\Delta E_{\text{at}}$ . If the resulting atomic energy  $T_{\text{at}} \cdot k_{\text{B}} + \Delta E_{\text{at}}$  is larger than the depth of the atom trap  $U_{\text{at}}$  (in our experiments  $U_{\text{at}} \approx 9 k_{\text{B}} \cdot \mu\text{K}$ ), the atom will be lost from the trap. In this case, the total energy of the atomic sample will change by

$$\Delta E_{\text{cloud}} = -\frac{3}{2} T_{\text{at}} \cdot k_{\text{B}} - \frac{1}{2} m_{\text{Rb}} \bar{\omega}_{\text{at}}^2 |\vec{r}_{\text{sec}}|^2, \quad (4.22)$$

with  $\bar{\omega}_{\text{at}}$  the geometrical mean of the atom trap frequencies. The position of the ion appears in the expression as it determines the position of the colliding atom and thus the potential energy that it contains. In the opposite case of a low energy transfer in the collision ( $T_{\text{at}} \cdot k_{\text{B}} + \Delta E_{\text{at}} < U_{\text{at}}$ ), the heated atom will remain trapped and eventually rethermalize with the rest of the cloud so that we simply get

$$\Delta E_{\text{cloud}} = \Delta E_{\text{at}}. \quad (4.23)$$

The final atomic temperature  $T_{\text{at,f}}$  after the collision can now be calculated using

$$T_{\text{at,f}} = \frac{3k_{\text{B}} T_{\text{at}} N_{\text{at}} + \Delta E_{\text{cloud}}}{3k_{\text{B}} N_{\text{at,f}}}, \quad (4.24)$$

where  $N_{\text{at,f}}$  denotes the final atom number. Implicitly, the described treatment of the temperature changes in the atomic sample assumes immediate rethermalization of the heated atom. In reality, the thermalization time will depend on the transferred energy  $\Delta E_{\text{at}}$  and may need to be taken into account to obtain more precise simulation results.

We do account for thermalization of the atomic sample in the trap by introducing evaporation effects following the derivations given in ref. [95]. Defining the ratio of the dipole trap depth and the mean thermal atomic energy  $\eta_{\text{evap}} = U_{\text{at}}/(k_{\text{B}}T_{\text{at}})$  we calculate the atom loss rate

$$\dot{N}_{\text{at}} = -2(\eta_{\text{evap}} - 4) \exp(-\eta_{\text{evap}}) \gamma_{\text{at}} N_{\text{at}}, \quad (4.25)$$

where

$$\gamma_{\text{at}} = 4\pi N_{\text{at}} m_{\text{Rb}} \sigma_{\text{at}} \frac{\bar{\omega}_{\text{at}}^3}{(2\pi)^3 k_{\text{B}} T_{\text{at}}} \quad (4.26)$$

is the interatomic collision rate. Here, the atomic s-wave collision cross section  $\sigma_{\text{at}}$  and the geometric mean of the atomic trap frequencies  $\bar{\omega}_{\text{at}}$  were used. The corresponding atomic temperature change is then given by

$$\dot{T}_{\text{at}} = \frac{\dot{N}_{\text{at}}}{3N_{\text{at}}} (\eta_{\text{evap}} - 1) T_{\text{at}}. \quad (4.27)$$

This treatment of evaporation effects assumes negligible background gas collisions and an evaporation parameter  $\eta_{\text{evap}}$  significantly larger than 4. Both of these assumptions are well fulfilled in our experiments.

Fig. 4.4 shows the simulation results and the data points taken under the experimental conditions outlined in section 4.3.1 ( $N_{\text{at}} = 1.1 \times 10^4$ ,  $T_{\text{at}} = 1.15 \mu\text{K}$ ,  $(\omega_{\text{at,x}}, \omega_{\text{at,y}}, \omega_{\text{at,z}}) = 2\pi \times (136, 141, 40) \text{ Hz}$ ). The electric field values are again 4.03 V/m (black trace and data), 1.86 V/m (green), 0.62 V/m (red) and 0.01 V/m (blue). The electric field is the only parameter that is varied both in the experiment and the simulation. To calibrate the electric fields in the experiment, we applied different voltages to the compensation electrodes and recorded the radial shift of the fluorescence of a  $^{138}\text{Ba}^+$  ion on the camera. This shift depends only on the radial ion trap frequency and the magnification of the imaging system. The magnification was in turn calibrated by measuring the distance between two  $^{138}\text{Ba}^+$  ions in an ion string. This distance can be directly calculated from the axial trap frequency. As both the radial and the axial ion trap frequencies are known on the percent level, the electric field calibration done in this way is also very accurate.

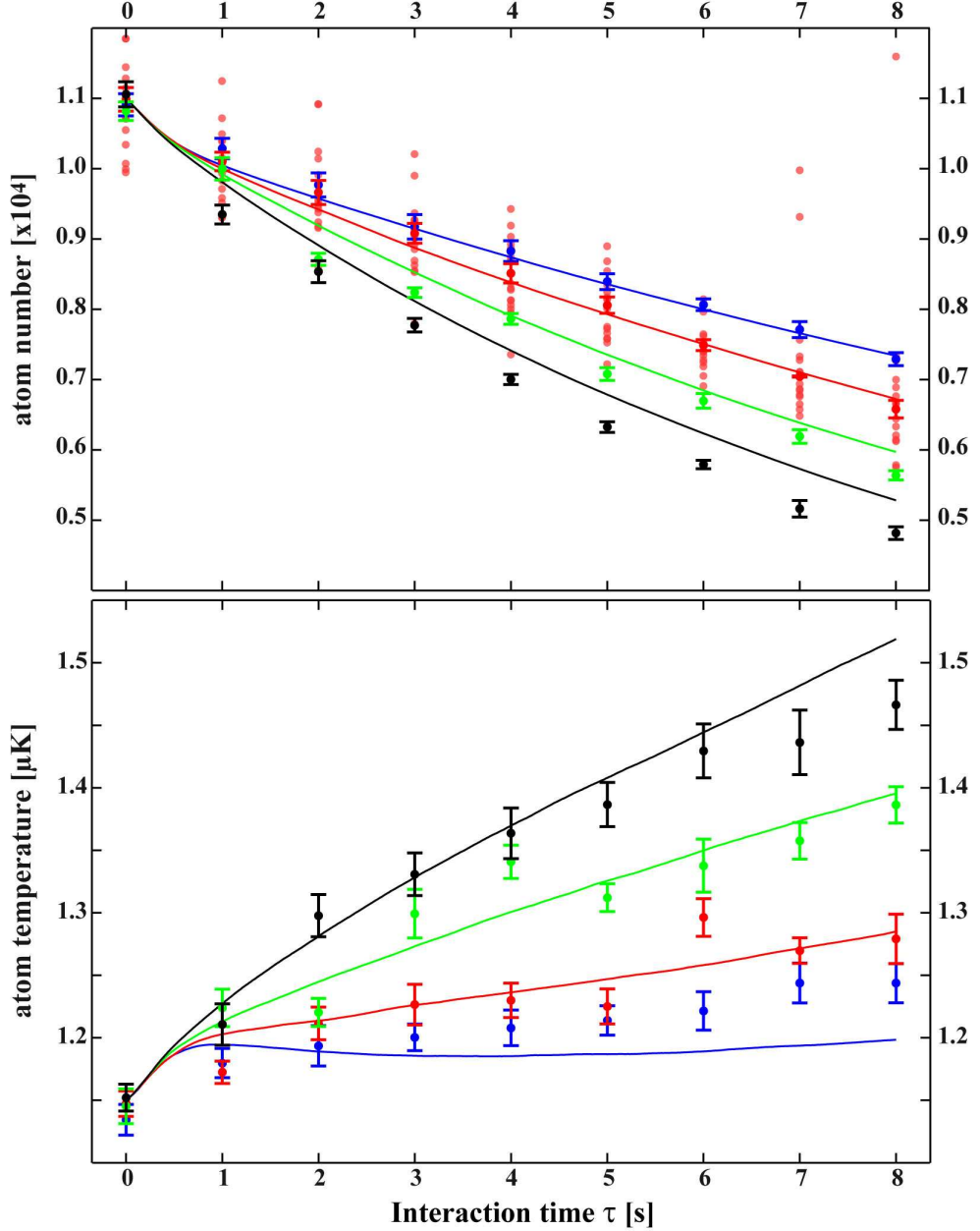


Figure 4.4: Measurement and simulation of the evolution of an atomic sample interacting with a single ion. The electric field values are again 4.03V/m (black), 1.86V/m (green), 0.62V/m (red) and 0.01V/m (blue). For the electric field setting of 0.62V/m the scattered red points in the upper panel show the outcomes of about 15 individual measurements at each interaction time. In all four data sets, three-body processes were filtered out to a large part by excluding the extreme events when calculating the averaged atom numbers and temperatures. The initial cool-down phase of the ion can be clearly seen. It is responsible for an initial atom loss and heating that does not depend on the amount of ion micromotion and thus is similar for all four data sets.

For the electric field setting of  $0.62\text{ V/m}$  the scattered red points in the upper panel of the figure show the outcomes of about 15 individual measurements at each interaction time. While most of these measurement outcomes lie within a relatively small error margin, there are some extreme outliers with almost no atom loss (best seen e.g. at  $\tau = 7\text{ s}$ ). These extreme events occur predominantly at low electric field settings and are explained by three-body recombination processes between the ion and two neutral atoms. The released energy ejects the ion from the atom cloud so that the interaction temporarily stops. The details of these processes are discussed in chapter 5. In the measurement shown here, the atomic density is so low ( $n_{\text{at}} \approx 10^{11}\text{ cm}^{-3}$ ), that atom-ion three-body interactions are very rare. As our simulation does not take three-body events into account, we want to suppress their influence on the obtained data. To do this, the mean atom number and temperature at each interaction time have been calculated by only including those individual measurements that lie within a  $2\sigma$  environment around the mean that is calculated from all data points at this field setting. In this way, the averaged values contain almost exclusively two-body atom-ion interactions.

The simulation is fitted to the data by only adjusting two initially unknown parameters, the initial ionic energy  $E_{\text{ion}} = 6\text{ K} \cdot k_{\text{B}}$  and the residual ionic energy  $E_{\text{res}} = 600\text{ }\mu\text{K} \cdot k_{\text{B}}$ . Comparing the data sets at the four different electric field settings, we clearly find that a more energetic ion generally leads to enhanced atom loss and a faster increase of the atomic temperature. The effect of the predicted long cool-down phase of the ion at the beginning of the interaction is also clearly visible both in the simulation results and the experimental data. The initially hot ion undergoes many glancing collisions typically leading to little atom loss but strong heating effects. At the lowest ion micromotion energy (blue trace and data points) the main part of the total atomic temperature increase is accumulated within the first second of interaction. Subsequently, the temperature stays almost constant for about five seconds. The corresponding simulation even indicates an intermediate phase in which the temperature decreases. This is a consequence of evaporative cooling which sets in after the initial heating phase and which temporarily dominates over the ion-induced heating rate. In this way, the atomic sample functions as a single ion calorimeter that sensitively detects even small changes in the motional properties of the ion. While the overall agreement of the simulation results and the experimental data is good, there are some significant deviations, e.g. in the atom number evolution at the highest ion energies (green and black traces) or the temperature evolution at the lowest energy (blue trace). These deviations indicate that

the sensitivity of the atom number on the ionic properties is underestimated by the simulation while the sensitivity of the atomic temperature is overestimated.

We have performed a further measurement in which we keep the atom-ion interaction time fixed at  $\tau = 8\text{ s}$  and apply vertical electric fields between  $\varepsilon_{\text{vert}} \approx -5\text{ V/m}$  and  $+5\text{ V/m}$  (see Fig. 4.5). The initial conditions of the atomic sample are almost identical to the previously discussed measurement and the atoms again interact with a single  $\text{Rb}^+$  ion. The scattered grey points show the outcomes of about 20 individual measurements at each setting of the electric field. Like before, we filter out the extreme events so that the mean atom numbers and temperatures result almost exclusively from two-body atom-ion interactions. We have also performed the numerical simulations for this measurement (solid traces in Fig. 4.5). Again, the overall qualitative agreement between the simulation and the data is quite good. However, similar to the measurement shown in Fig. 4.4, the sensitivity of the atom loss feature on electric fields is underestimated (the simulation result is "too flat") while the sensitivity of the atomic temperature is overestimated (the simulation result is "too steep").

It is difficult to rigorously trace the observed deviations between simulation and experiment to a specific simplification made in the simulation. The assumption of immediate thermalization of an atom after a collision has already been mentioned. It is an interesting question how a delayed thermalization would affect the evolution of the atomic sample. Also, as the sample is permanently in a non-equilibrium state due to the local perturbations induced by the ion, the density distribution will deviate from the expected Gaussian profile. This may affect the measurement of the atomic temperature which is based on performing a Gaussian fit to the atomic density profile. Further, the simulation ignores possible local depletion effects of the atomic density caused by a well-localized ion. The simple approach discussed in the context of local depletion in chapter 3 does not take into account the ion dynamics shown in Fig. 4.3. As the ion energy and thus its spatial fluctuations can change dramatically even on short timescales, a more sophisticated simulation of depletion effects has to reproduce the local evolution of the atomic density on these timescales.

## 4.4 Excess micromotion compensation measurements

The results shown in Fig.4.4 and Fig.4.5 nicely demonstrate the sensitivity with which ionic properties can be detected using the ultracold neutral sample as a calorimeter.

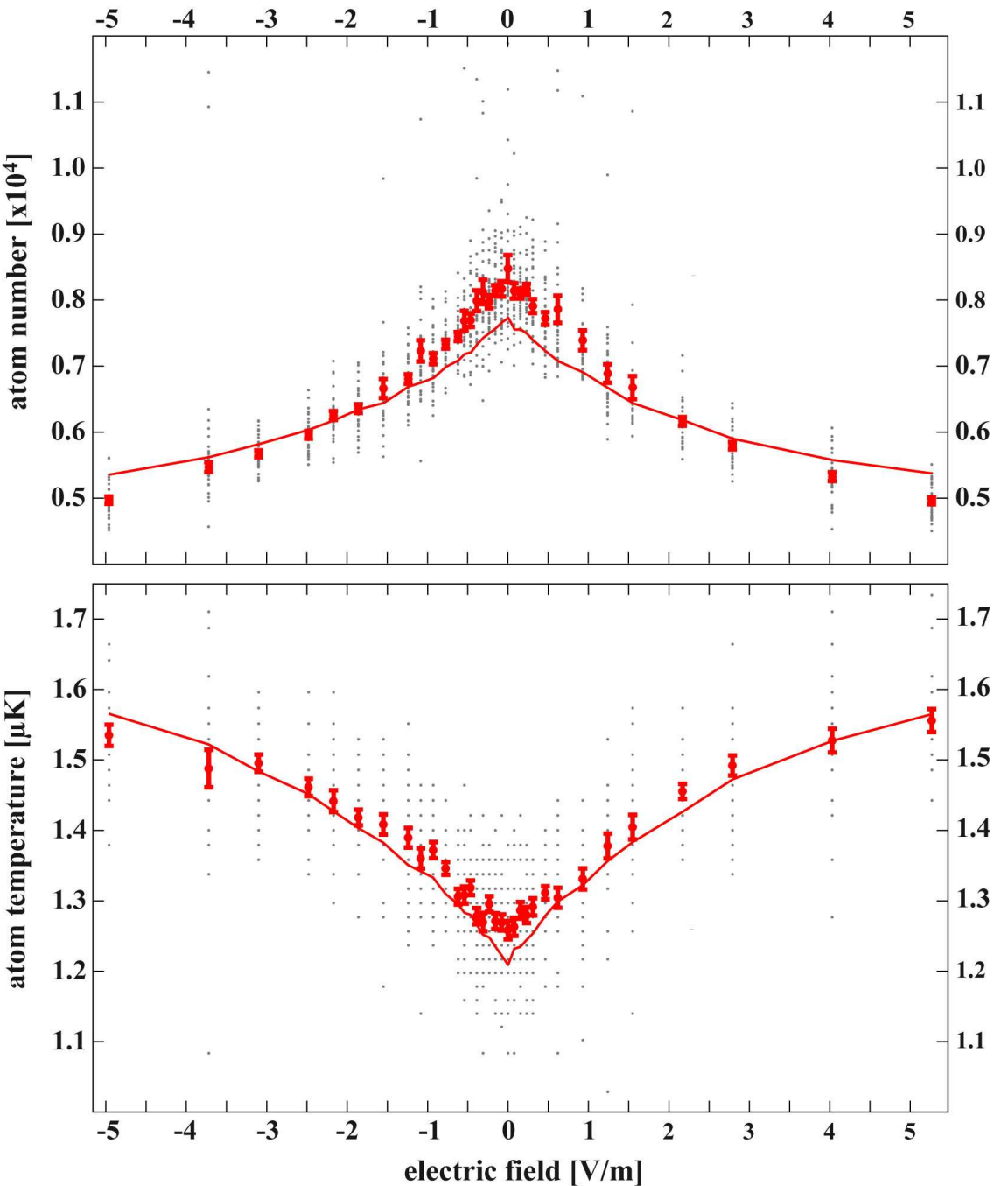


Figure 4.5: Measurement of atom numbers and temperatures after a fixed atom-ion interaction time  $\tau = 8\text{ s}$ . The grey data points show the scatter of the individual measurements. The displayed mean atom numbers and temperatures include almost exclusively two-body atom-ion interactions. The solid line shows the result of the numerical simulation.

I will now focus on this application of our hybrid setup and present novel methods for the compensation of excess micromotion that we have developed based on atom-ion interaction experiments.

#### 4.4.1 Compensation of radial excess micromotion

The measurements discussed in the previous section have already been committed to the investigation of the effects of radial micromotion that we can tune by changing the electric fields in vertical direction. Fig.4.6 shows the same measurement as Fig.4.5 with a focus on the atomic signals close to the optimal compensation voltage setting. At electric fields  $|\varepsilon_{\text{vert}}| \lesssim 0.2 \text{ V/m}$  we can observe a flattening both in the atom numbers and the corresponding temperatures. To determine the optimal compensation setting more precisely we fit parabolic functions locally to the atom number maximum and temperature minimum, respectively (see insets in Fig. 4.6). In both independent fits the uncertainty of the optimal electric field setting is below 0.05 V/m. The radial micromotion energy can thus be minimized to the corresponding value of  $E_{\text{eMM,vert}} \lesssim k_B \cdot 3.2 \mu\text{K}$ . At the highest electric fields the micromotion energy amounts to  $E_{\text{eMM,vert}} \approx k_B \cdot 50 \text{ mK}$  so that we cover a total of four orders of magnitude in micromotion energy.

We now repeat this measurement using a larger and denser atomic sample with  $N_{\text{at}} \approx 8.8 \times 10^4$ ,  $T_{\text{at}} \approx 830 \text{ nK}$  and  $n_{\text{at}} \approx 1.5 \times 10^{12} \text{ cm}^{-3}$ . The increase in density by more than an order of magnitude compared to the first measurement has a significant impact on the characteristics of the atom-ion interactions. As the electric field is reduced, the ion energy is lowered and three-body interactions with atoms become increasingly important (compare Fig. 5.4). This can be seen in Fig. 4.7 when focussing on the number of outliers at high and low electric fields. In fact, at the lowest field settings, we can expect almost every atom-ion interaction period  $\tau$  to include at least one three-body event that ejects the ion from the atom cloud. In this regime, instead of producing outliers with regard to a clearly defined mean experimental outcome, the interaction dynamics is dominated by the rare but violent three-body interactions leading to a very broad distribution of the atomic signals. Consequently, the averages in this measurement are taken over all data points at a given electric field. When comparing Fig. 4.7 with the previous measurement (Fig. 4.6) we find that the electric field sensitivity is further enhanced by the additional effects of the three-body interactions. As a result, ion micromotion can be compensated to values corresponding to electric fields  $|\varepsilon_{\text{vert}}| \lesssim 0.03 \text{ V/m}$  or micromotion energies  $E_{\text{eMM,vert}} \lesssim k_B \cdot 1.1 \mu\text{K}$ .

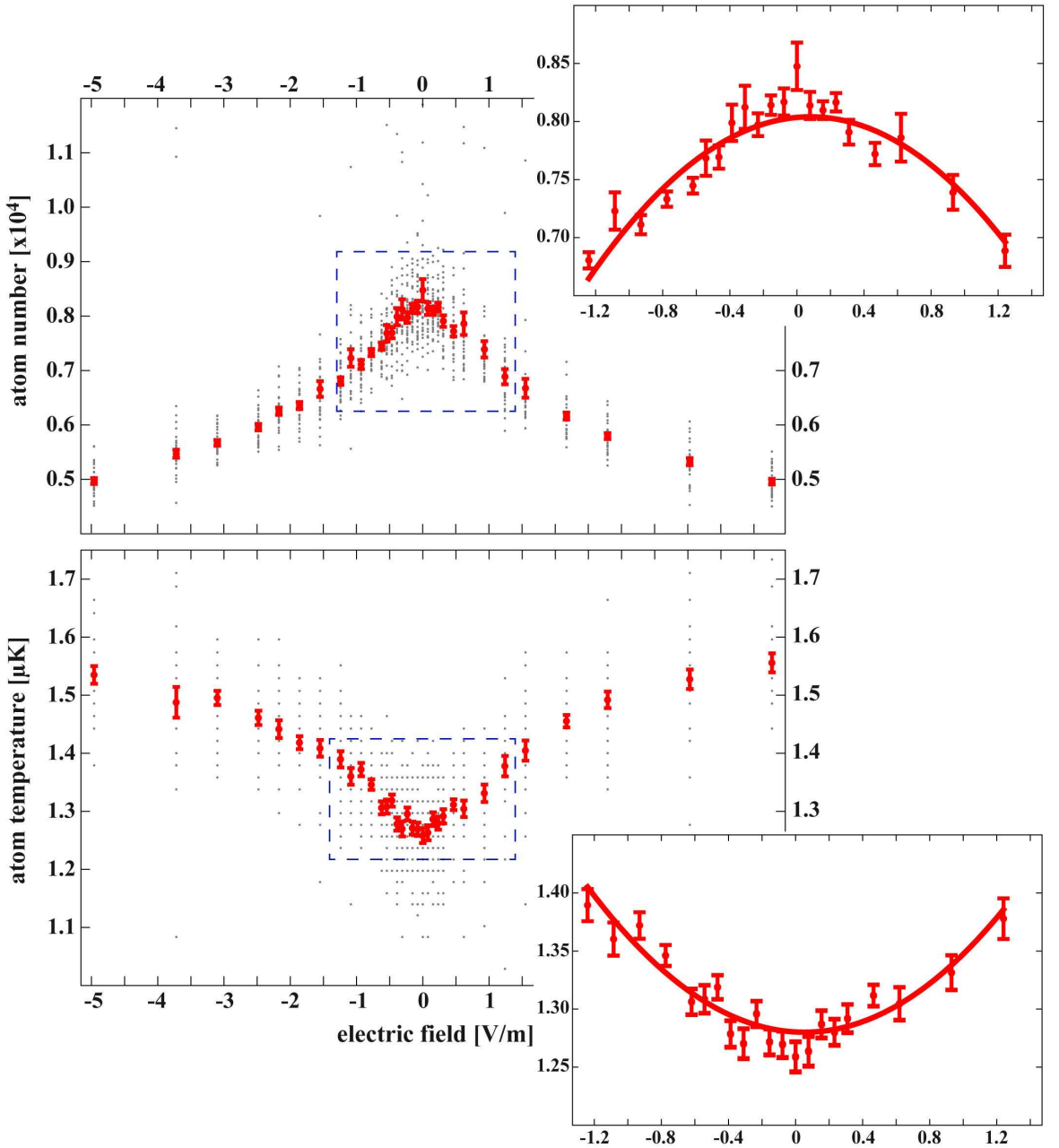


Figure 4.6: Excess micromotion compensation measurement using an atomic sample at a density of  $n_{\text{at}} \approx 10^{11} \text{ cm}^{-3}$ . The displayed mean atom numbers and temperatures include almost exclusively two-body atom-ion interactions. *Insets:* Parabolic functions are fitted locally to the atom number maximum and the temperature minimum, respectively. This allows for micromotion compensation corresponding to electric field values  $|\varepsilon_{\text{vert}}| \lesssim 0.05 \text{ V/m}$ .

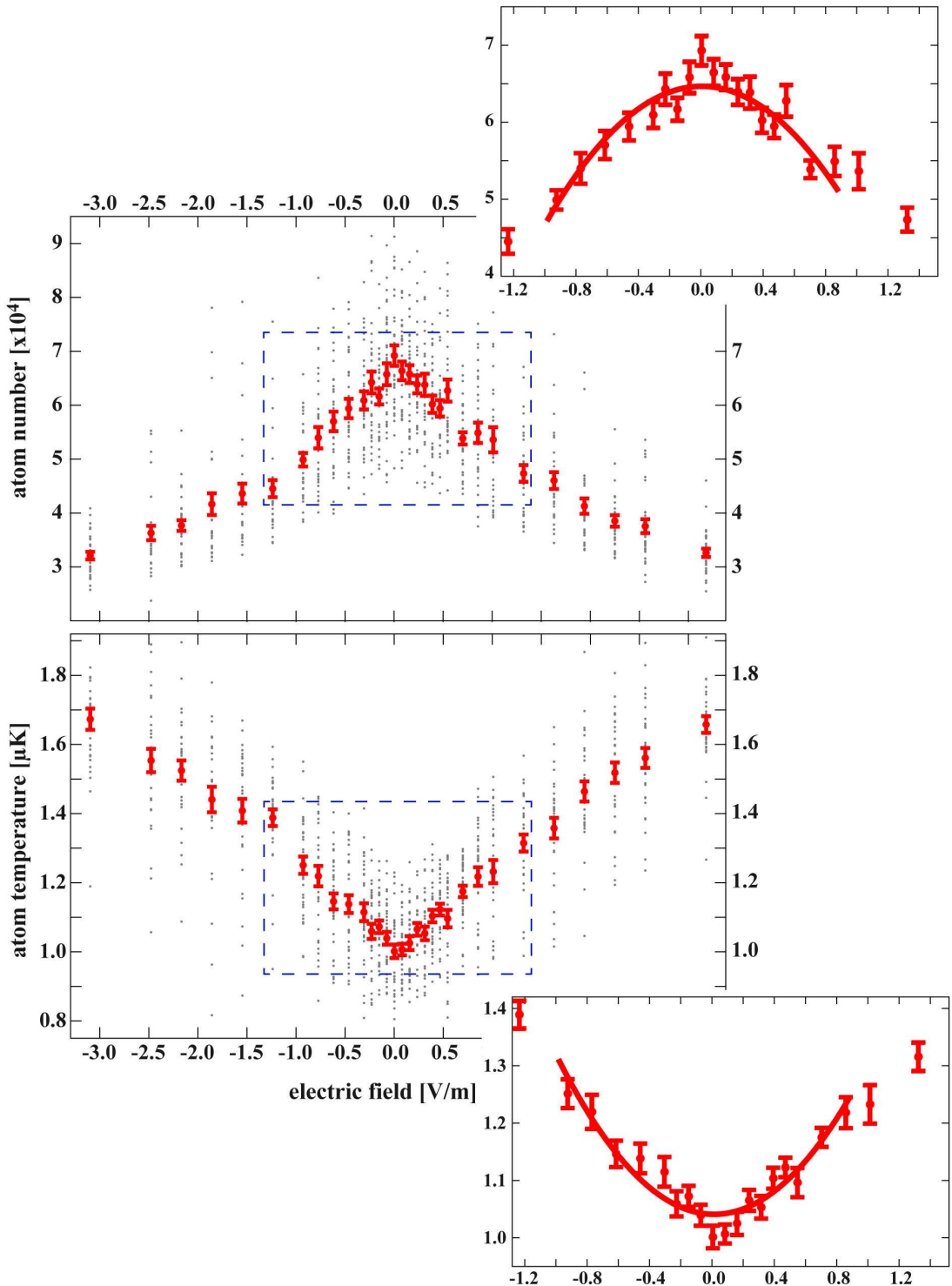


Figure 4.7: Same as Fig. 4.6 but using an atomic sample at a density of  $n_{\text{at}} \approx 1.5 \times 10^{12} \text{ cm}^{-3}$ . The additional effects of three-body atom-ion interaction increase the electric field sensitivity and allow for micromotion compensation corresponding to electric field values  $|\varepsilon_{\text{vert}}| \lesssim 0.03 \text{ V/m}$ .

Performing a simple analysis of the results presented in Figs. 4.6 and 4.7 we can gain a good qualitative understanding of the dominant physical processes and their effects on the atomic cloud. In the case of almost purely two-body atom-ion interactions (Fig. 4.6), the scattering rate is described by formula 4.17:

$$\Gamma(t) = n_{\text{at}}(\vec{r}_{\text{ion}})\sigma_{\text{ai}}(E_{\text{col}})v_{\text{ion}}(t).$$

When varying the radial compensation voltages, the ion position  $\vec{r}_{\text{ion}}$  changes only very slightly so that we can assume the atomic density to be independent of the compensation voltage. However, the compensation voltage determines the ion energy and therefore both the atom-ion scattering cross section  $\sigma_{\text{ai}}(E_{\text{col}}) \propto E_{\text{col}}^{-1/3} \propto E_{\text{ion}}^{-1/3}$  and the ionic velocity  $v_{\text{ion}}(t) \propto E_{\text{ion}}^{1/2}$ . In total, the scattering rate will thus scale as

$$\Gamma(t) \propto E_{\text{ion}}^{-1/3} \cdot E_{\text{ion}}^{1/2} = E_{\text{ion}}^{1/6}. \quad (4.28)$$

If we additionally neglect atomic density changes during the interaction time  $\tau$  and use equation 4.9, we obtain a rough estimate for the total atom loss  $N_{\text{loss}}$  as a function of the electric field  $\varepsilon_{\text{vert}}$

$$N_{\text{loss}} \approx \Gamma \cdot \tau \propto \varepsilon_{\text{vert}}^{1/3}. \quad (4.29)$$

This scaling with the cube root of the electric field can indeed be recognized in Fig. 4.6 when inspecting the curvature and the flattening of both the mean atom numbers and the atomic temperatures.

The results shown in Fig. 4.7 show a different behavior. The atom losses and the atomic temperatures increase almost linearly with the electric field. This is explained by the additional effects of atom-ion three-body events. As is discussed in chapter 5, the corresponding three-body coefficient  $K_3$  scales roughly as  $K_3 \propto E_{\text{ion}}^{-0.43} \propto \varepsilon_{\text{vert}}^{-0.86}$ . A three-body event temporarily ejects the ion from the atom cloud. Effectively, this reduces the atom-ion interaction time  $\tau$  and introduces a dependence of this parameter on the electric field  $\tau = \tau(\varepsilon_{\text{vert}})$ . The amount of time the ion spends outside the atom cloud and the ion recooling dynamics are difficult to estimate. However, the relatively strong dependence of the three-body coefficient on the electric field adds to the relatively weak dependence of the two-body scattering rate. This motivates the qualitative change observed in Fig. 4.7 with an almost linear scaling of atom numbers and temperatures with electric field. It is thus the interplay of two-body and three-body dynamics that helps us improve the sensitivity of our micromotion compensation scheme when working with denser atomic samples.

#### 4.4.2 Compensation of axial micromotion

In section 4.1 I have pointed out the importance of axial micromotion in our Paul trap. Using the atomic sample as a sensor, we can now also minimize this micromotion contribution. In these measurements, due to the much weaker confinement in axial direction and the much lower value of the  $q$  parameter in this direction, the ion position  $\vec{r}_{\text{ion}}$  shifts significantly when varying the axial micromotion via the endcap voltages. In contrast to the compensation of radial micromotion, the ion is thus subjected to different atomic densities depending on the axial shift  $\Delta r_z$  from the trap center. Thus, the Gaussian density profile of the atom cloud becomes clearly visible in the measurement shown in Fig. 4.8. As the ion is moved towards the trap center, the increase in density gives rise to increased atom losses and heating roughly down to positional shifts  $|\Delta r_z| \gtrsim 20 \mu\text{m}$ . At even smaller displacements of the ion, a dramatic reduction of the ionic impact on the atom cloud is observed despite the high atomic densities that the ion experiences. This is due to the increasing relative reduction of micromotion energy as the ion approaches the trap center ( $\Delta E_{\text{eMM},z}/E_{\text{eMM},z} \propto 1/\Delta r_z$ ). The fits to the data allow us to determine the position of the rf frequency node to within  $\Delta r_{z,\min} \approx 0.6 \mu\text{m}$ . The axial micromotion energy can then be calculated with

$$E_{\text{eMM},z} = \frac{m_{\text{Rb}}}{16} \cdot (q_z \Omega_D \Delta r_z)^2 , \quad (4.30)$$

(compare equation 4.8) so that we obtain  $E_{\text{eMM},z} \approx k_B \cdot 9 \mu\text{K}$ . This is much larger than the radial excess micromotion energies. As stated earlier, the axial micromotion proves to be of significant importance when minimizing the total energy of the ion. However, when adding up the residual ion energy contributions induced by imperfect ion positioning in all three dimensions, the result falls short of the residual ion energy  $E_{\text{res}} = 600 \mu\text{K} \cdot k_B$  extracted from the simulations in section 4.3. This indicates that further ion heating mechanisms such as excess micromotion induced by phase differences between opposing rf electrodes, electronic noise in the trap electrodes or anomalous heating effects play a role in our experiments. Quantifying and reducing these sources of heating requires further experimental and theoretical investigations (see also section 4.6).

Another important point becomes obvious when analyzing the data in Fig. 4.8. Since the sensitivity of atom-ion interactions with regard to the axial positioning of the ion is on the order of  $1 \mu\text{m}$ , axial micromotion compensation can only work for a single ion. The trapping of a second ion leads to axial positional shifts on the order of

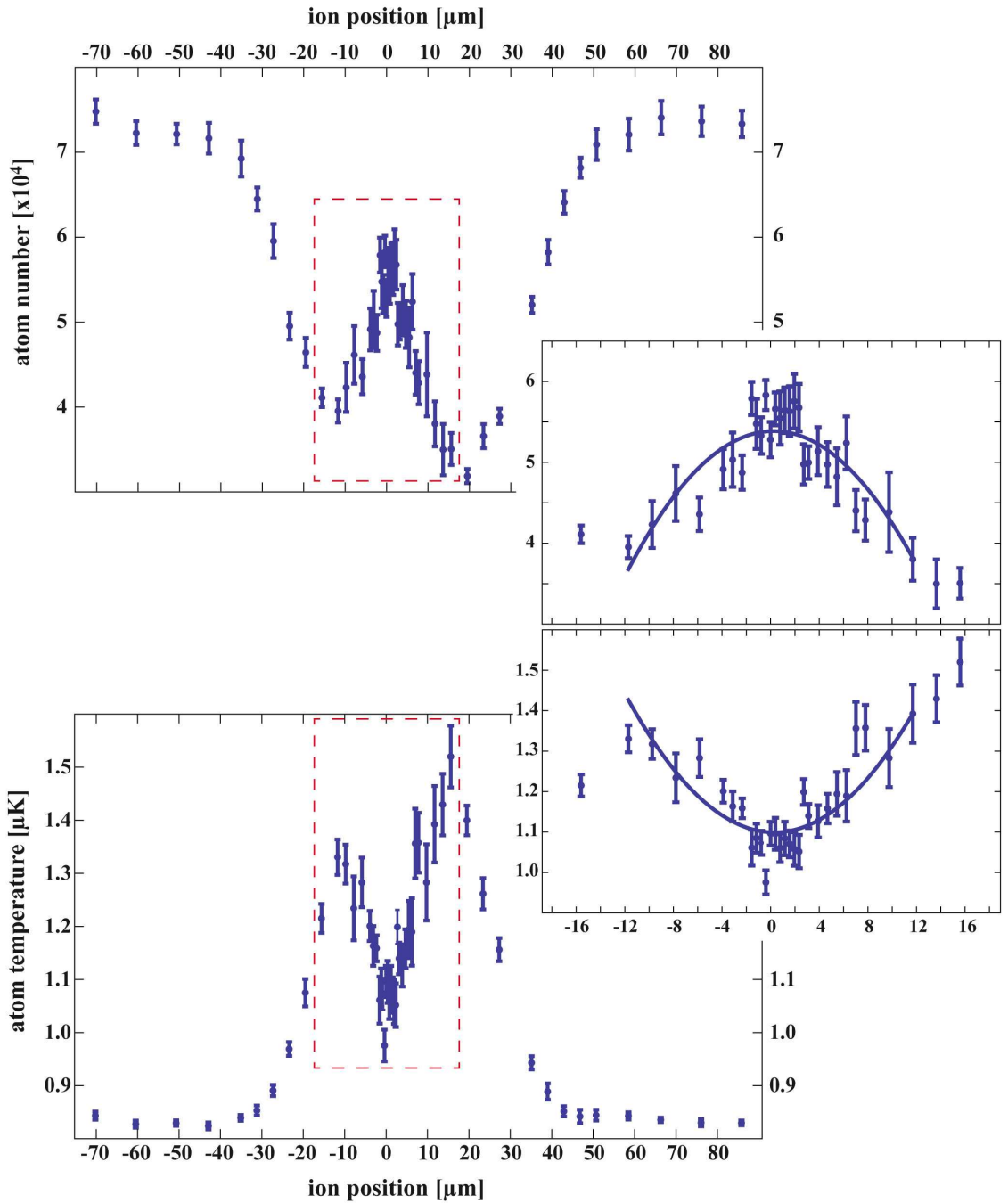


Figure 4.8: Measurement of the axial micromotion of the ion. Due to the small value of  $q_z$ , the ion shifts through the atom cloud as its micromotion is varied. In the outer part of the plot ( $|\Delta r_z| \gtrsim 20 \mu\text{m}$ ), the Gaussian density profile of the atomic sample can be recognized. At smaller ionic displacements, the reduction in axial micromotion dominates over the change in atomic density and a drastic decrease of the impact on the atomic sample is observed. The fits shown in the insets allow us to determine the position of the rf frequency node to within  $\Delta r_{z,\min} \approx 0.6 \mu\text{m}$ .

$10\ \mu\text{m}$  and consequently to large amounts of micromotion. The measurement shown in Fig. 4.8 can therefore also be used to unambiguously determine whether a single ion has been trapped. Additional ions will completely eliminate the drastic decrease of atom losses at the center of the trap.

It should be noted that performing atom-based micromotion compensation requires an iterative process of compensating all three dimensions. The data shown in Figs. 4.6-4.8 were acquired after micromotion in the remaining two directions had already been minimized.

#### 4.4.3 Comparison with established compensation methods

We have compared the atom-based micromotion compensation methods with well-established compensation methods based on fluorescence detection of single ions.

##### Comparison with fluorescence-based compensation in our setup

We employ two different micromotion compensation methods that rely on the determination of the ion's position or the spread of the fluorescence on an electron-multiplying charge-coupled device camera, respectively (see Fig. 4.9). The first method solely requires a precise determination of the ion's position. By fitting a Gaussian profile to the fluorescence signal, this position can be determined down to values of about  $50\ \text{nm}$ . This is much smaller than the diffraction limit of our objective lens and is only limited by the signal-to-noise-ratio between ion fluorescence signal and background counts of the camera. In vertical direction, micromotion compensation is done by monitoring the ion position while switching the radial trap frequency between  $\omega_x \approx 2\pi \times 220\ \text{kHz}$  and  $\omega_x \approx 2\pi \times 100\ \text{kHz}$ . If external electric fields are present, they exert a force on the ion which competes with the confining force of the trap. As a consequence, the ion's position shifts more strongly when the radial trap frequency is reduced. By detecting the shift with a precision on the order of  $50\ \text{nm}$ , electric fields can be compensated to better than  $0.03\ \text{V/m}$ , comparable to the precision of the atom-based compensation method. The described method is widely used in Paul traps and is usually referred to as a rather coarse technique (see e.g. [74]). In our trap, however, the attained accuracy is excellent and comparable to much more involved methods. This is largely due to the comparably low trapping frequencies that we can realize while still maintaining stable ionic confinement.

This simple and precise method currently cannot be used in the other radial direction due to the angle of view of the camera. In this direction as well as in axial direction

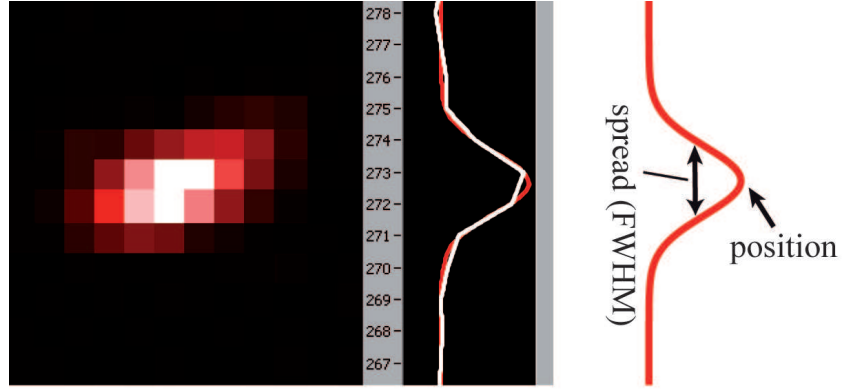


Figure 4.9: Analysis of the fluorescence signal from a single  $^{138}\text{Ba}^+$  ion. A Gaussian profile is fitted to the signal. The center position of this profile can be determined down to about 50 nm despite the typical fluorescence spread on the order of  $2\ \mu\text{m}$ . Figure adapted from [91].

we use a second method which is based on exciting the ion's secular motion via frequency modulation of the trap drive  $\Omega_D$  [96,97]. When modulating  $\Omega_D$  at a secular frequency, we resonantly drive an oscillation of the ion in the secular potential. This effects an increase in the spread of the fluorescence detected on the camera. When the ion is shifted from the rf frequency node, it experiences stronger rf fields and the excitation becomes stronger. With this method, we can compensate the horizontal electric fields in radial direction down to 0.1 V/m and position the ion axially to better than 1  $\mu\text{m}$ .

We have verified that the atom-based compensation measurements yield the same optimal compensation voltages as determined via the established fluorescence-based methods. The precision of the atom-based compensation methods is comparable or better than the described fluorescence-based methods. The fluorescence-based methods have the advantage of working on timescales of a few minutes which is about two orders of magnitudes faster than the atom-based methods. However, they require the trapping of a laser-cooled ion. This implies the heating of an oven for the generation of an atomic beam and the usage of ionization and cooling lasers at wavelengths below 500 nm. These measures are known to have significant impact on the ion trap conditions, e.g. through the buildup of patch charges, and lead to drifts of the optimal compensation voltages on timescales between minutes and days (see also section 4.5).

	$\varepsilon_{\text{rad}}$ [V/m]	$u_{\text{rad}}$ [nm]	$E_{\text{rad}}$ [ $\mu\text{K}\cdot k_{\text{B}}$ ]	$\varepsilon_{\text{ax}}$ [V/m]	$u_{\text{ax}}$ [nm]	$E_{\text{ax}}$ [ $\mu\text{K}\cdot k_{\text{B}}$ ]
$^{172}\text{Yb}^+$ [98]	0.9	1.1	60	0.3	-	-
$^{40}\text{Ca}^+$ [99]	0.42	0.46	3.6	-	-	-
$^{25}\text{Mg}^+$ [100]	-	-	-	-	0.2	0.75
$^{87}\text{Rb}^+$	0.03	0.8	1.1	0.056	24	9

Table 4.1: Comparison of commonly used figures of merit to quantify ion micromotion. Residual electric fields  $\varepsilon_i$ , micromotion motional amplitudes  $u_i$  and micromotion energies  $E_i \equiv E_{\text{eMM},i}$  are given. The first three rows show values extracted from the cited references to the best of my knowledge. The last row gives the values obtained in this thesis.

### Comparison with measurements from other groups

The precision of micromotion compensation achieved in our experiment is clearly the highest reached in atom-ion experiments so far (compare e.g. [14, 17]). A similar degree of compensation can be found in ion trapping setups working on atomic clocks and precision spectroscopy. In the following, I will compare our results to such high-precision apparatuses.

First, micromotion compensation measurements were recently reported in [98]. In this reference,  $^{172}\text{Yb}^+$  ions are used to minimize micromotion via photon-correlation measurements. The obtained residual electric fields are on the order of 0.5 V/m resulting in excess micromotion energies of about  $60 \mu\text{K}\cdot k_{\text{B}}$  in the radial directions. The sensitivity of these measurements thus is significantly lower than the results reached in our trap via atom-ion interaction measurements. Axial micromotion in [98] seems to be somewhat lower due to the design of the trap.

In a second reference, compensation is done using resolved sideband measurements on  $^{40}\text{Ca}^+$  ions [99]. The achieved micromotion energies are on the order of  $3 \mu\text{K}\cdot k_{\text{B}}$  in the radial directions. No statement is made about the axial direction which could not be measured due to the incidence angle of the sideband laser beam.

In a third experimental setup, a Raman laser scheme is used to realize axial micromotion minimization of trapped  $^{25}\text{Mg}^+$  ions down to  $0.75 \mu\text{K}\cdot k_{\text{B}}$  [100]. In this reference, no statement is made about the radial directions, again due to the incidence angles of the laser beams.

To summarize these comparisons, the performance of our trap and the described compensation technique appears to be excellent, even when comparing to state-of-the-art compensation methods used on isolated ions (see table 4.1). An especially valuable feature of atom-based micromotion compensation is the direct applicability to all three spatial dimensions. Performing three-dimensional compensation on a similar level via laser-based techniques comes at the cost of considerable experimental

Wavelength [nm]	$\Delta U_{\text{ver}}/(P_{\text{L}} \cdot t)$ [V/Ws]
413	2.83
493	0.50
532	0.01
650	0.00

Table 4.2: Changes of the vertical compensation voltage as a function of the laser wavelength normalized to laser power and exposure time. A sharp increase of the influence of the light on the compensation voltages is seen at wavelengths below 500 nm.

efforts to implement the corresponding laser beams.

## 4.5 Long-term drifts of compensation voltages

A known issue in many ion traps is the accumulation of patch charges on dielectric surfaces in proximity to the trap center. These charges are created through the photoelectric effect induced by laser light at wavelengths below about 500 nm. Changes of the patch charges lead to changes of the electric fields at the trap center and thus to positional shifts of the trapped ions. These shifts increase the excess micromotion and need to be counteracted by adjusting the compensation voltages.

We have tested the effects of the four lasers used for photoionization and laser cooling of  $\text{Ba}^+$  ions in our setup (see table 4.2). As expected, starting at wavelengths below 500 nm we find a sharp increase in the impact of the light on the compensation voltages. In our setup, patch charges are probably mainly created on the mounts for the trap electrodes and for the Ba oven which are made out of machineable glass-ceramic (Macor) (see section 2.2.2 for details). We find the strongest shifts of the electric fields to occur in the vertical and axial directions. This is probably due to the oven mount which is located about 1 cm below one of the endcap electrodes (see Fig. 2.5). As this mount breaks the symmetry of the trap setup, light which is reflected in a diffuse way from vacuum windows can still lead to electric field shifts in a preferred direction. A detailed discussion of these effects can be found in ref. [91].

A unique feature of the atom-based compensation method is that it requires the usage of only infrared laser light within the Paul trap. In addition to the high-power laser needed for the dipole trap at a wavelength of 1064.5 nm, only very small amounts of light at 780 nm are required for absorption imaging of the atomic samples. We have found both wavelengths to produce no measurable patch charges that would shift the optimal compensation voltages. In a typical ion trapping setup as is commonly used, e.g. for quantum information processing, the discussed buildup

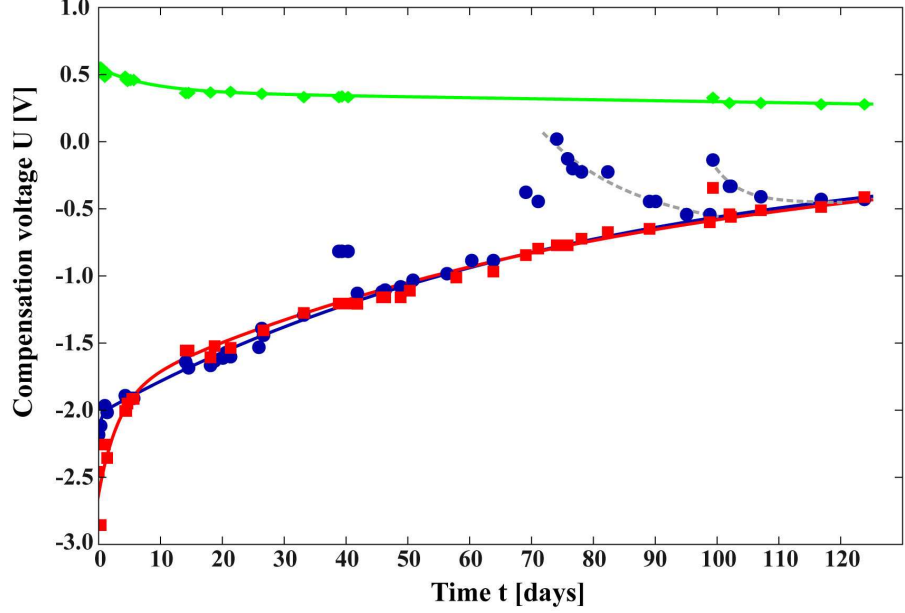


Figure 4.10: Long-term drift of the vertical (blue), horizontal (red) and axial (green) compensation voltages over a timespan of about 4 months. Except for two occasions ( $t \approx 70$  days and  $t \approx 100$  days) the Paul trap was isolated from any light below a wavelength of 780 nm. The solid lines are double-exponential fits to the data yielding long-term time constants on the order of three months. Figure partly adapted from [91].

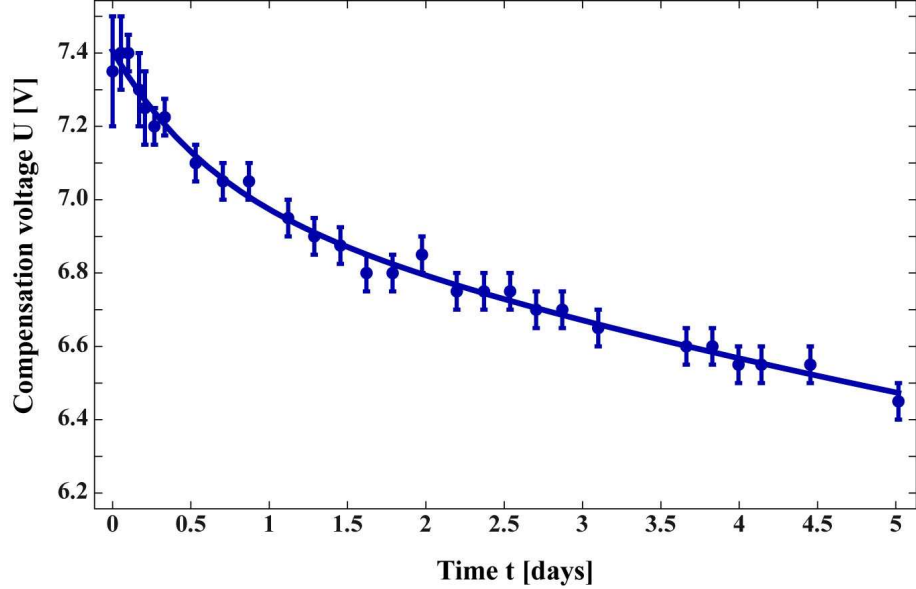


Figure 4.11: Relaxation of the compensation voltage shift induced by subjecting the Paul trap to light at 413 nm. The solid line is a double-exponential fit to the data with a dominant slow decay with a time constant  $\tau_2 \approx 11$  days.

of charges on dielectric surfaces will continuously take place due to the cooling light at short wavelengths. This makes it difficult to observe long-term effects on the ion trap conditions which may occur e.g. through deposition of atoms from the oven on the trap electrodes. Such effects are believed to be relevant in the context of anomalous heating in ion traps and have been extensively investigated over the course of the last decade. A series of reports from different groups has been published [94, 101–105]. Using the atom-based micromotion detection method, we were able to monitor the evolution of the compensation voltages over a timespan of about four months with very little perturbations through light-induced patch charge buildup. The results are shown in Fig. 4.10 for the vertical (blue), horizontal (red) (i.e. horizontal and radial with respect to the trap axes) and axial (green) directions. Before these measurements were started, the ion trap had been operated with  $\text{Ba}^+$  ions so that both the Ba oven and the necessary lasers had been frequently used. The voltage Null in the plot has been set to the expected long-term limits. The solid lines are double-exponential fits to the data which account for relatively rapid initial decays with time constants  $\tau_1 \approx 0.5 - 3$  days and subsequent slow decays within  $\tau_2 \approx 100$  days. At two occasions ( $t \approx 70$  days and  $t \approx 100$  days) the light-tight protective covers around the experimental setup had to be removed for several hours so that the Paul trap was subjected to ambient white light of the fluorescent lamps. As a consequence, the compensation voltage in vertical direction increases and then decays back towards its long-term behavior within several days. In general, however, the change of the compensation voltages becomes continuously slower over time. After 100 days, the daily drift of the vertical compensation voltage is less than 10mV so that the electric field in this direction is stable to within 0.03 V/m. Such stability has been crucial to the investigations of atom-ion three-body interactions (see chapter 5) for which the ion energies had to be reliably set for thousands of consecutive experimental cycles.

After the time period shown in Fig. 4.10 we made use of the almost perfect stability of the trap conditions to test the individual influence of the ionization laser at 413 nm. As expected, shining in about 3 mW of laser power for a few minutes shifted the vertical compensation voltage by about 2 V. The laser was then switched off and the decay of the voltage shift was monitored over 5 days (see Fig. 4.11). The data is excellently fit by a double-exponential curve with a rapid initial decay on a timescale  $\tau_1 \approx 0.6$  days and a dominant slow decay with  $\tau_2 \approx 11$  days. This is in accordance with the decay curves seen in Fig. 4.10 after the Paul trap had been subjected to ambient light. The long-term drift induced by the slow decay of patch charges generated by "blue" light can therefore be expected to generally occur towards smaller

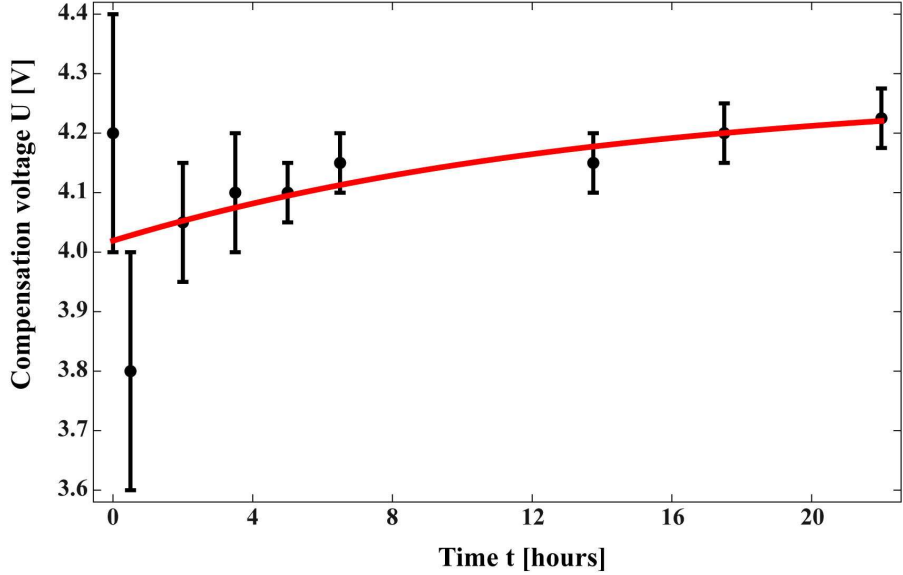


Figure 4.12: Relaxation of the compensation voltage shift induced by heating the Ba oven at a current of 7 A for a few minutes. Before the oven was switched on, the compensation voltage was around 6.4 V, close to the final values of Fig. 4.11. During the oven heating time the compensation voltage consequently dropped by about 2.4 V (unresolved in the displayed data). Subsequently, it required one to two hours to reestablish a good degree of compensation by optimizing the compensation voltages in all three dimensions. This explains the comparably large error bars of the first two data points. In total, the voltage shows a drift towards higher voltages which could explain the long-term behavior seen in Fig. 4.10.

compensation voltages in vertical direction.

Finally, we have also investigated the influence of the Ba oven. It was switched on at a typical heating current of 7 A for a few minutes and the subsequent relaxation of the compensation voltages was measured (see Fig. 4.12). While the oven was heated, the voltage dropped by about 2.4 V (this drop is not resolved in the data of Fig. 4.12 due to its short timescale) and then gradually increased with a time constant of 6 days. As this measurement was performed shortly after the measurement shown in Fig. 4.11, the time constant extracted in the investigation of the oven may be influenced by a continuing decay of the patch charges generated through the ionization laser. However, we can still conclude that the oven produces a long-term drift towards higher vertical compensation voltages and can therefore be responsible for the very slow drift with a timescale of about 100 days dominating in Fig. 4.10.

While the underlying mechanism for the effects of the "blue" light can be under-

stood relatively easily, this is more difficult for the case of the Ba oven. A possible explanation is the deposition of Ba atoms on the trap electrodes which then leads to electric field shifts via the contact potentials that are created on the stainless steel surfaces. Over time, the Ba atoms may chemically react with the surface so that these contact potentials slowly decrease. As the oven is located below the trap, the lower side of the electrodes will be predominantly affected by the atomic beam. This could explain the drift into a preferred direction.

Summarizing the results of the atom-based compensation of ion excess micromotion, we have shown that this method provides a novel possibility to determine compensation voltages in all three dimensions. The precision of these measurements is comparable to standard fluorescence-based techniques and is applicable to all ionic species that allow stable trapping in our Paul trap. As a great advantage, the atom-based compensation only requires infrared laser light which has enabled us to work with an almost drift-free Paul trap. As a byproduct, we were also able to investigate the long-term drifts of compensation voltages and how they are influenced by "blue" light and by heating of the Ba oven. In hybrid atom-ion setups, where ultracold atom clouds are readily available within the Paul trap, compensation of micromotion via this method may become an important tool in the further development of the field.

## 4.6 The role of inherent micromotion in atom-ion interactions

The discussion so far has been restricted to the effects of ion excess micromotion neglecting possible implications of the inherent micromotion that the ion undergoes. This is reasonable with regard to the early measurements presented in chapter 3, where excess micromotion was clearly dominant and lead to ion energies on the order of tens of mK. In section 4.4 I showed how we could significantly increase the control over the electric fields and thus reduce excess micromotion effects by orders of magnitude. It is now interesting to consider the case of an ideal Paul trap with complete elimination of excess micromotion in an environment of ultracold atoms. This has been done by Cetina and coworkers in ref. [35]. In this scenario, the ion initially follows a trajectory given by equation 4.6 with  $\Delta r_i = 0$ . When the ion is approached by a neutral atom, the attractive atom-ion interaction will lead to a deviation from this trajectory so that the hard-core atom-ion collision occurs outside the trap center at a distance  $R_{\text{col}}$ . This distance depends on the mass ratio between atom and ion and on the ionic confinement. For our case of homonuclear atom-ion

interaction and a radial trap frequency  $\omega_x = 2\pi \times 350$  kHz we obtain  $R_{\text{col}} \approx 50$  nm. This number is to be compared to the effect of a residual stray electric field in x-direction  $\varepsilon_x = 0.03$  V/m which displaces the ion by  $\Delta r_x = 7$  nm. We can thus conjecture that at this level of electric field control, the implications of the inherent micromotion become comparable or greater than the effects of field-induced excess micromotion. The ion displacement  $R_{\text{col}}$  at the time of the collision has two main consequences. Firstly, the micromotion will be enhanced at this position and an increased amount of energy can be transferred into ion energy through the collision (compare equation 4.21). Secondly, as the attraction to the atom pulls the ion from its original position at the trap center, the electric fields of the Paul trap can do work on the moving ion and increase its energy. In general, ref. [35] predicts this second effect to be dominant, especially at low values of the trap parameter  $q$ . For our typical trap settings, a lower bound for the ion energy of  $E_{\text{ion,min}} \approx 90 \mu\text{K}\cdot k_{\text{B}}$  is predicted due to the effects of the inherent micromotion. In the realistic situation in which axial micromotion also occurs, this value may even be somewhat higher. If the Rb<sup>+</sup> ion is replaced by Ba<sup>+</sup> and the trap frequency and  $q$  parameter are kept constant,  $E_{\text{ion,min}}$  is reduced slightly to about  $80 \mu\text{K}\cdot k_{\text{B}}$ . This is due to the larger mass of the Barium ion which is thus less susceptible to the perturbing force exerted by the approaching neutral atom.

It may be possible to measure the influence of the inherent micromotion by exploiting the sensitivity of our atom-based probing technique. Since we are able to detect the small energy differences induced by electric fields in the mV/m regime, it may also be feasible to observe changes in the atomic signal when varying the characteristics of the inherent micromotion. A possible scheme would be to measure the scaling of the ion energy with the  $q$  parameter while keeping the drive frequency  $\Omega_D$  constant. We expect three micromotion energy contributions to be relevant in these experiments: electric field-induced excess micromotion energy, excess micromotion energy caused by phase differences between opposing rf electrodes and inherent micromotion energy. While the field-induced micromotion energy decreases with  $q$  as  $E_{\text{eMM},i} \propto q^{-2}$ , both the micromotion energies due to phase differences ( $E_{\text{eMM},\varphi} \propto q^2$ ) and inherent micromotion ( $E_{\text{ion,min}} \propto q^{2/3}$ ) increase with  $q$ . In principle, the different scaling of the three energy contributions should thus allow us to identify the dominant source of micromotion heating in our experiments. Such a scheme requires excellent experimental control over the relevant parameters and a precise theoretical model to extract reliable ion energies from measured atomic signals.

# Chapter 5

## Single Ion as a Three-Body Reaction Center in an Ultracold Atomic Gas

Physical Review Letters **109**, 123201 (2012)

Arne Härtter, Artjom Krükow, Andreas Brunner, Wolfgang Schnitzler,  
Stefan Schmid, and Johannes Hecker Denschlag

*Institut für Quantenmaterie und Center for Integrated Quantum Science and  
Technology IQ<sup>ST</sup>, Universität Ulm, 89069 Ulm, Germany*

We report on three-body recombination of a single trapped Rb<sup>+</sup> ion and two neutral Rb atoms in an ultracold atom cloud. We observe that the corresponding rate coefficient  $K_3$  depends on collision energy and is about a factor of 1000 larger than for three colliding neutral Rb atoms. In the three-body recombination process large energies up to several 0.1 eV are released leading to an ejection of the ion from the atom cloud. It is sympathetically recooled back into the cloud via elastic binary collisions with cold atoms. Further, we find that the final ionic product of the three-body processes is again an atomic Rb<sup>+</sup> ion suggesting that the ion merely acts as a catalyst, possibly in the formation of deeply bound Rb<sub>2</sub> molecules.

## 5.1 Introduction

Early on in the quest for ultracold quantum gases three-body recombination played a crucial role as a limiting factor for Bose-Einstein condensation. It was first investigated in spin-polarized hydrogen [106] and somewhat later for alkali atoms [107, 108]. Recently, three-body recombination was investigated with single atom resolution [109]. Combining ultracold atoms with cold trapped ions is an emerging field where large scattering cross sections naturally come into play due to the comparatively long range  $1/r^4$  polarization interaction potential. Two-body collisions between atoms and ions in the low energy regime have been recently studied [11, 14–16, 21, 24, 59]. In this letter, we report on three-body collisions involving two ultracold  $^{87}\text{Rb}$  atoms and a  $^{87}\text{Rb}^+$  ion at mK temperatures. The ion in our experiment can be regarded as a reaction center, facilitating molecule formation through its large interaction radius.

For the work presented here, it is essential that we work with ions and atoms of the same species. This renders charge transfer reactions irrelevant, which otherwise would strongly constrain our measurements. As  $\text{Rb}^+$  is not amenable to laser-cooling and cannot be imaged, we detect the ion and investigate its dynamics in an indirect way, i.e. through its action on the atom cloud. In our experiments, we place a single ion into the center of an atomic sample resulting in a continuous loss of atoms due to elastic atom-ion collisions. This behavior is interrupted when a highly energetic three-body process ejects the ion from the atom cloud. By examining the statistics of ion-induced atom loss in hundreds of repetitions of the experiment, we can investigate a number of important details of the three-body process, such as its quadratic density-dependence, the energy that it releases, its rate coefficient  $K_3$ , the dependence of  $K_3$  on collisional energy, and its reaction products. Furthermore, our measurements also demonstrate sympathetic cooling of an ion from eV energies down to about 1 mK using an ultracold buffer gas.

## 5.2 Experimental Setup

The atom-ion collision experiments are conducted in a hybrid apparatus (for details see [110]) where a single  $^{87}\text{Rb}^+$  ion, trapped in a linear Paul trap, is brought in contact with an ultracold cloud of spin polarized  $^{87}\text{Rb}$  atoms ( $F = 1, m_F = -1$ ). The atom cloud is previously prepared at a separate location from where it is transported to the Paul trap and loaded into a far off-resonant crossed optical dipole trap. The dipole trap is at first spatially separated from the trapped ion by about  $50\ \mu\text{m}$ . To start

the atom-ion collision experiments it is then centered on the ion with  $\mu\text{m}$  precision within a few 100ms. At this point the atom cloud consists of  $N_{\text{at}} \approx 4.0 \times 10^4$  atoms at a temperature of  $T_{\text{at}} \approx 1.2 \mu\text{K}$  and a peak density  $n_{\text{at}} \approx 1.1 \times 10^{12} \text{ cm}^{-3}$ . At trapping frequencies of (190, 198, 55) Hz this results in a cigar shaped cloud with radial and axial extensions of about 10  $\mu\text{m}$  and 35  $\mu\text{m}$ , respectively.

The single Rb<sup>+</sup> ion is confined in a Paul trap driven at a frequency of 4.17 MHz resulting in radial and axial trapping frequencies of 350 kHz and 72 kHz, respectively. As the trap is about 4 eV deep, the ion typically remains trapped for thousands of experimental cycles. It is initially produced by photoionization of an atom from a cold Rb cloud in the Paul trap [111]. Typical kinetic energies  $E_{\text{ion}}$  of the ion after sympathetic cooling in the atom cloud are about a few mK· $k_{\text{B}}$ . This energy scale is mainly set by two quantities: (1) The excess micromotion (eMM) [74] in the Paul trap whose main part we can control by compensating stray electric fields [111]. (2) Heating effects induced by the interplay of micromotion and elastic collisions [19, 20, 35].

### 5.3 Evidence for Atom-Ion Three-Body Interaction

As described in [16], an ion immersed in an ultracold atom cloud leads to atom loss by expelling atoms from the shallow optical trap ( $\approx 10 \mu\text{K} \cdot k_{\text{B}}$  trap depth) via elastic collisions. The radio frequency (rf) driven micromotion is a constant source of energy which drives these loss-afflicting collisions. Figure 5.1a shows such a decay of an atom cloud at relatively low densities ( $\approx 10^{11} \text{ cm}^{-3}$ ) and relatively high ion energies ( $\approx 35 \text{ mK} \cdot k_{\text{B}}$  [112]). Plotted is the number of remaining atoms after an atom-ion interaction time  $\tau$ . Each data point corresponds to a single measurement. Overall, the plot shows a relatively smooth decay of the atom cloud with a relative scatter of the atom number of less than 10%. This changes drastically when we carry out the experiments at low ion energies ( $\approx 0.5 \text{ mK} \cdot k_{\text{B}}$  [112]) and larger densities ( $\approx 10^{12} \text{ cm}^{-3}$ ) (Fig. 5.1b). Here, the scatter dramatically increases with  $\tau$  and is on the order of the number of lost atoms. In Fig. 5.1c histograms are shown which contain the data of Fig. 5.1b. With increasing time  $\tau$  the initial Gaussian distribution develops a striking tail towards large atom numbers. At the tips of the tails we find cases where even after interaction times of several seconds barely any atoms have been lost, a signature of missing atom-ion interaction. Apparently, sporadically the ion is ejected from the atom cloud and promoted onto a large orbit for a period of time during which atom-ion collisions are negligible (Fig. 5.2a). In principle, this is reminiscent

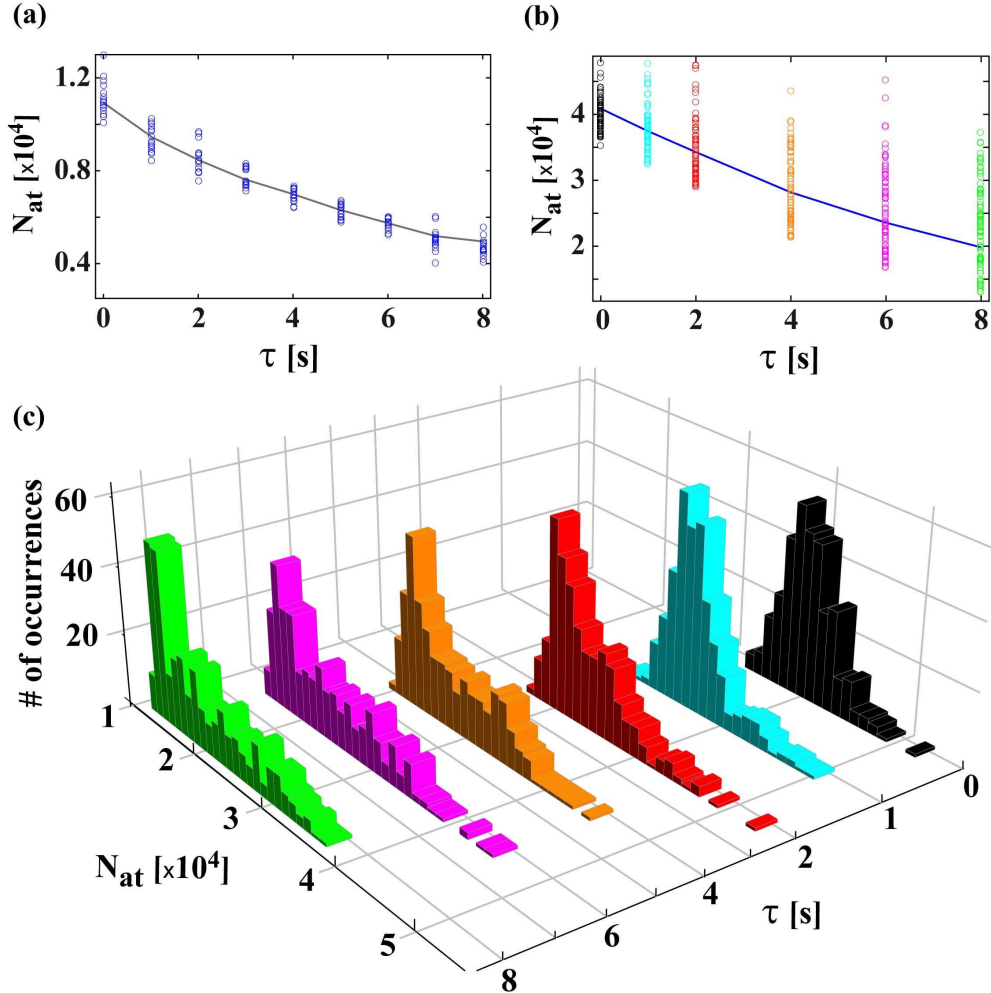


Figure 5.1: Decay of the atom cloud under influence of a single trapped ion. (a) Remaining atom numbers after interaction time  $\tau$  for an ion with  $E_{\text{ion}} \approx 35 \text{ mK}\cdot k_{\text{B}}$  [112] and  $n_{\text{at}} \approx 10^{11} \text{ cm}^{-3}$ . The solid line indicates the decay of the mean atom number. (b) Same as (a) but  $E_{\text{ion}} \approx 0.5 \text{ mK}\cdot k_{\text{B}}$  [112] and  $n_{\text{at}} \approx 1.1 \times 10^{12} \text{ cm}^{-3}$ . (c) Histograms containing the data shown in (b).

of the energy distributions with high energy tails that have recently been predicted for trapped ions immersed in a buffer gas [19, 20]. However, it turns out that such an explanation is inconsistent with our observations on the grounds of energetics and scaling. Rather, we find that it is a three-body recombination process involving the ion and two neutrals that ejects the ion from the cloud. Due to the large trap depth the ion is not lost in such an event, but it is recooled back into the cloud through binary collisions after some time.

Figure 5.2b illustrates in a simple picture how the decay of the atom number over time can follow different paths. The solid trace  $T_1$  shows the case when only binary atom-ion collisions occur. Such traces result in the narrow Gaussian peak of the atom number distribution shown on the right of Fig. 5.2b. Traces  $T_2$  and  $T_3$  exhibit three-body collisions at points  $E_2$  and  $E_3$ . At point  $R_2$  the ion reenters the atom cloud after an interruption time  $t_{\text{out}}$ . Rare three-body events and long times  $t_{\text{out}}$  result in a long tail of the distribution. We can reproduce the histograms in Fig. 5.1 with a simple Monte Carlo type simulation (for details see supplemental material). We assume an initial Gaussian distribution of the atom number which then decays exponentially with the binary atom-ion collision rate  $K_2 n_{\text{at}}$ . Here,  $K_2$  is a rate constant given by the product of the elastic cross section and the ion velocity. A three-body event, occurring at a rate  $K_3 n_{\text{at}}^2$ , interrupts this decay for a period  $t_{\text{out}}$ . As the ion can only be recooled by the atomic sample, we assume the rate for reentry of the ion into the atom cloud to be proportional to the number of atoms  $1/\langle t_{\text{out}} \rangle = N_{\text{at}}/c_{\text{out}}$  with  $c_{\text{out}}$  being a constant that depends on the trap parameters. Figure 5.2b (right) shows exemplarily that the model can describe well the histograms in Fig. 1. In the following we continue the analysis by studying  $P_{\text{threebody}}$  which is the probability that at least one three-body process takes place within time  $\tau$ . For each  $\tau$  we determine  $P_{\text{threebody}}$  from our histograms.  $P_{\text{threebody}}$  is the count number of the tail of a histogram divided by the histogram's total count number (for details see supplemental material). Fig. 5.2c shows these data for four atomic densities, including the data in Fig. 5.1c. All four data sets have in common that the number of three-body events first rapidly increases and subsequently levels off. The levelling off is mainly due to the fact that the probability for a three-body reaction is strongly density-dependent. Surprisingly, in the beginning of the interaction ( $\tau \lesssim 1$  s) only very few three-body events are detected for the lower density samples. We explain this delay by an initial phase of sympathetic cooling of the  $\text{Rb}^+$  ion which experiences significant heating during the preparation (e.g. rf evaporative cooling) of the atom cloud. From numerical calculations similar to [20] we estimate that recooling times

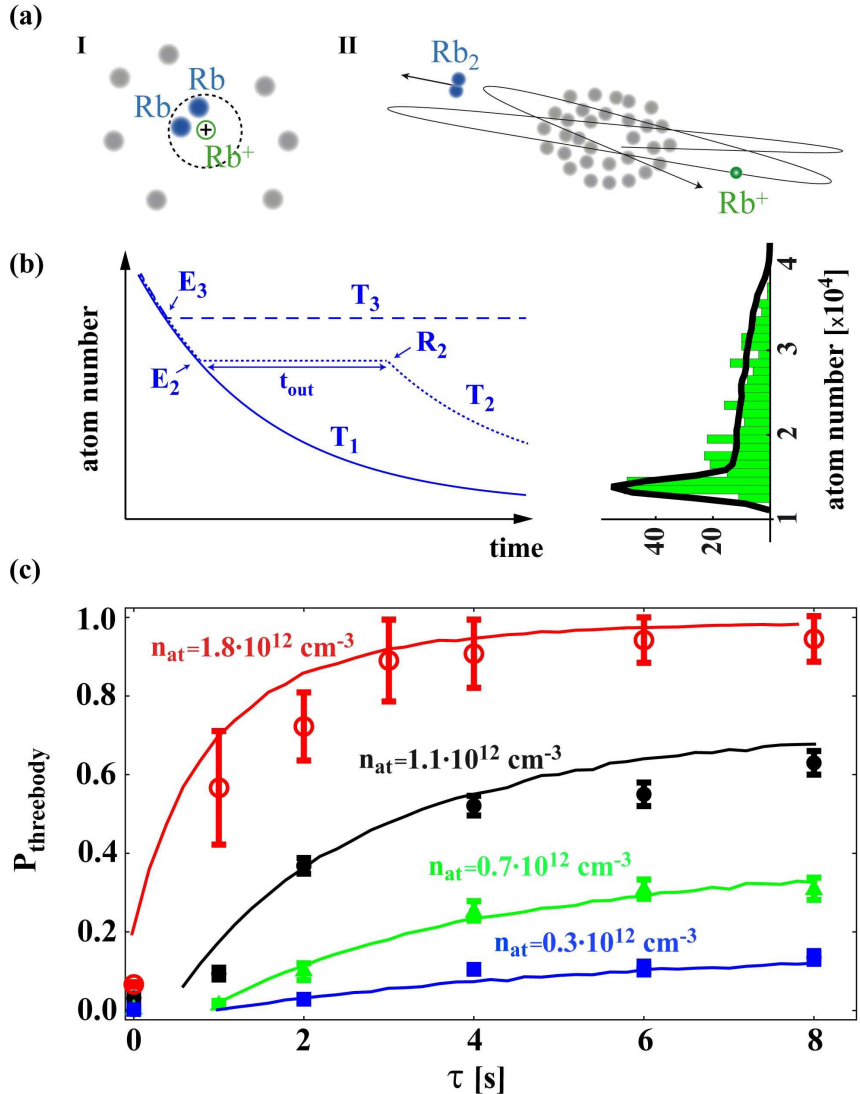


Figure 5.2: (a) Illustration of an atom-atom-ion collision. (I) Two atoms simultaneously enter the interaction radius of the ion and a three-body process takes place. (II) The three-body reaction ejects the ion onto a trajectory much larger than the atom cloud. (b) Illustration of our simple model. *Left:* Various possible time traces for the atom number. If only binary atom-ion collision occur the atomic sample decays exponentially (Trace T<sub>1</sub>). Three-body events (E<sub>2</sub>, E<sub>3</sub>) interrupt the atom loss until the atom is recooled and reenters the sample at point R<sub>2</sub> (Traces T<sub>2</sub> and T<sub>3</sub>). *Right:* Atom number histogram from Fig. 5.1c ( $\tau = 8$  s) and the corresponding simulation result (solid black line). (c) Plot of the probability  $P_{\text{threebody}}$  for initial atomic densities  $(1.8, 1.1, 0.7, 0.3) \times 10^{12} \text{ cm}^{-3}$  and atom numbers  $(6.5, 4.0, 2.8, 1.6) \times 10^4$ , respectively. The solid lines are results of the numerical simulation.

of about 1 s in atom clouds with  $n_{\text{at}} \approx 10^{12} \text{ cm}^{-3}$  correspond roughly to ion kinetic energies of a few  $100 \text{ K}\cdot k_{\text{B}}$ . The ion will typically undergo several thousand binary collisions with cold atoms until it is sympathetically recooled to  $\text{mK}\cdot k_{\text{B}}$  energies. We are able to describe all four data sets in Fig. 5.2c consistently with our simple Monte Carlo model (continuous lines). The initial cool-down time is accounted for by adjusting the starting time for each data set. From a fit to the data sets we obtain rate coefficients  $K_2 = 5.0(5) \times 10^{-9} \text{ cm}^3/\text{s}$  and  $K_3 = 3.3(3) \times 10^{-25} \text{ cm}^6/\text{s}$  and the reentry parameter  $c_{\text{out}} \approx 1.7 \times 10^5 \text{ s}$ . The errors given exclude systematic uncertainties in the atomic density. We note that the value for our atom-atom-ion  $K_3$  rate coefficient is more than three orders of magnitude larger than the three-body coefficient for three colliding neutral  $^{87}\text{Rb}$  atoms [107]. The value of  $K_2$  roughly agrees with previously obtained results [15, 16]. For the typical atom numbers used here the obtained value of  $c_{\text{out}}$  results in several seconds of negligible atom-ion interaction following each ejection of the ion.

In order to challenge our analysis we have attempted to model the events that send the ion into orbit as two-body processes. The corresponding linear density dependence of the event rate yields inconsistent fit results such that we can exclude two-body interactions as an explanation for our data (for details see supplemental material). As a cautionary note, we point out that three-body recombination processes to weakly-bound molecular states with binding energies  $\lesssim 10 \text{ meV}$  are not detected in our experiments as the ion will not leave the atom cloud. Thus, the true three-body coefficient may even be significantly larger.

## 5.4 Direct Measurement of the Energy released in the Recombination Events

In a further experiment, we quantify the kinetic energy gained by the ion in a three-body event. The idea is to lower the depth of the ion trap such that an ion with an energy of a few 0.1 eV escapes while a cold ion remains trapped. The experiment is performed as follows. We prepare a first atom cloud which we bring to interaction with an ion for 4 s. Similar to the previously described experiments, we measure the ion-induced atom loss from which we judge whether or not the ion has participated in a three-body event. Directly afterwards, the ion trap depth is reduced to one of 5 values  $U_{\text{red}}$  by lowering one of the endcap voltages of the Paul trap within 300 ms. The voltage is held at this value for 200 ms and ramped back up within 200 ms. Subsequently, we probe the ion's presence in the trap via the loss it inflicts on a second

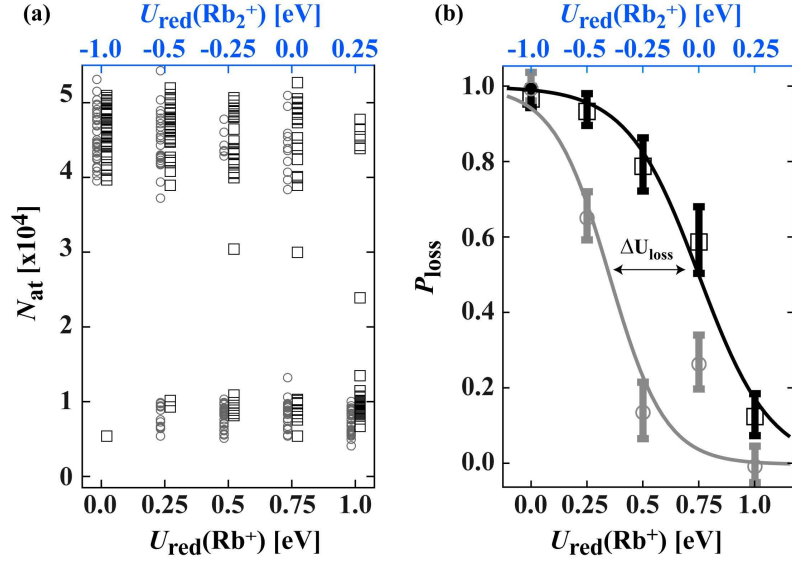


Figure 5.3: (a) Probing the ion's presence using an atom cloud. A low (high) remaining atom number  $N_{\text{at}}$  signals the presence (absence) of an ion. For better visibility, we have slightly offset in energy the black squares corresponding to ions that have participated in a three-body process from the grey circles corresponding to ions where purely binary collisions were detected. (b) Ion loss probability  $P_{\text{loss}}$  calculated from the data in (a). The continuous lines are fits to the data using a broadened step function. The trap depths  $U_{\text{red}}$  are determined for our Paul trap geometry using methods detailed in [92] for both  $\text{Rb}^+$  (bottom abscissa scale) and  $\text{Rb}_2^+$  (top). A trap with negative trap depth value is non-trapping.

atom cloud. This cloud is prepared within 40 s and contains about  $5 \times 10^4$  atoms. Figure 5.3a shows the remaining atom number of the atom cloud after 6 s of interaction time. We deliberately apply an offset electric field of about 6 V/m to increase the eMM energy. In this way, we make three-body reactions unlikely and induce a rapid loss of atoms through binary atom-ion collisions. An atom number  $\lesssim 1 \times 10^4$  indicates the presence of an ion while a number around  $4.5 \times 10^4$  shows its absence. The clear splitting of the two groups of data allows for ion detection with an efficiency close to unity. Figure 5.3a contains two different plot symbols, distinguishing two classes of ions. Black squares correspond to ions that have participated in a three-body event within the first atom cloud while grey circles correspond to ions where only binary collisions were detected. We now analyze the data points of Fig. 5.3a by calculating the probability for ion loss  $P_{\text{loss}}$  for each trap depth ( $P_{\text{loss}} = \text{Number of lost ions} / \text{Number of trials}$ ). The result is shown in Fig. 5.3b. As expected, ions that were previously involved in a three-body recombination process can in general escape from deeper traps than ions only involved in binary interactions. To obtain a more quantitative measure of the ion energy we fit broadened step functions of the form  $1 / \{1 + \exp[(U_{\text{red}} - U_{\text{loss}})/d]\}$  to the data. The width of the steps  $d$  is on the order of 0.15 eV. From the energy offset between the two fit curves we estimate the gained energy  $\Delta U_{\text{loss}} \approx 0.4$  eV. We note that for trap depths  $U_{\text{red}} \lesssim 0.25$  eV the probability of loss is high in general. This suggests that the stability of our trap is compromised at shallow trap settings. In fact, lowering the voltage of only one of the two endcaps renders the trap quite asymmetric. This degrades the ideal quadrupole field configuration and thus the stability of the ion trap. As a consequence the accuracy with which we can determine the energy released in the three-body process is limited. Still, we find a clear splitting between the step functions of 0.4 eV in Fig. 5.3b. Thus, a resolution of the measurement on the order of 0.1 eV seems plausible.

Mainly two recombination processes come into consideration. In a reaction of the type  $\text{Rb} + \text{Rb} + \text{Rb}^+ \rightarrow \text{Rb}_2 + \text{Rb}^+$  the formation of a neutral molecule is catalyzed by the ion which carries away 2/3 of the energy released. If deeply bound  $\text{Rb}_2$  molecules are produced, binding energies of up to  $\sim 0.5$  eV are released, in agreement with the measurement. A second possible recombination process,  $\text{Rb} + \text{Rb} + \text{Rb}^+ \rightarrow \text{Rb}_2^+ + \text{Rb}$ , produces a molecular ion and a neutral atom. However, as indicated in figure 3, the molecular ion, due to its higher mass, experiences a significantly shallower trap than the atomic ion and would immediately be lost for our parameter range. We thus infer that the ion at hand is  $\text{Rb}^+$ . However, we cannot completely exclude the formation of an intermediate molecular ionic state which may

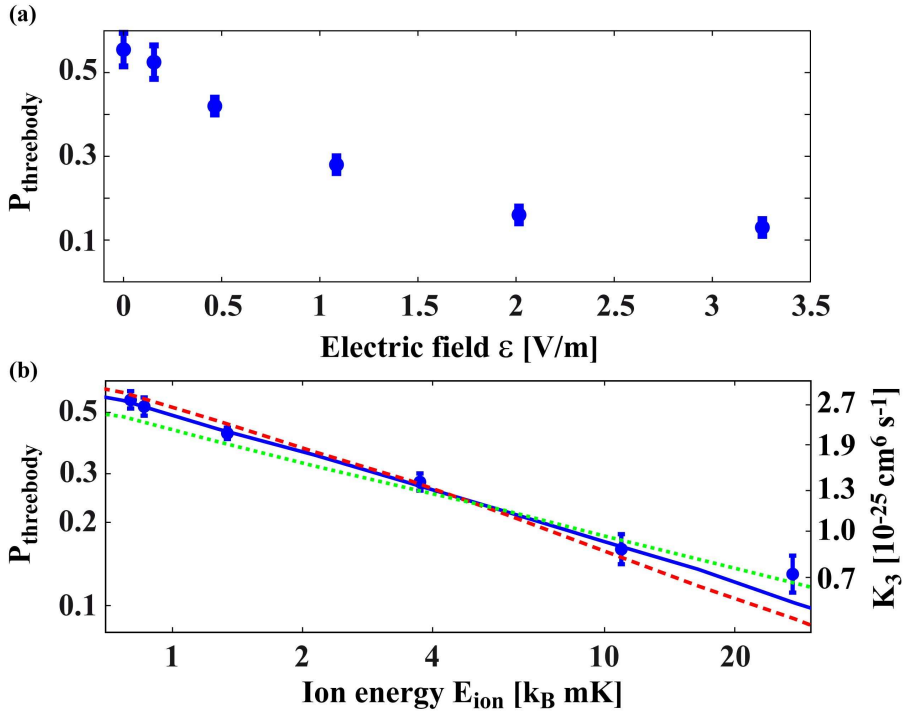


Figure 5.4: (a)  $P_{\text{threebody}}$  as a function of the external electric field. (b) Double-logarithmic plot of  $P_{\text{threebody}}$  as a function of the ion energy  $E_{\text{ion}}$  [112]. A scale for the three-body coefficients  $K_3$  as derived from the simulation is also given (see text for details).

subsequently dissociate.

## 5.5 Measurement of the Energy Dependence of the Three-Body Coefficient

In a third type of measurement we study the dependence of the three-body coefficient on the ion kinetic energy which we can tune by controlling the ion micromotion. For this we apply a static electric field  $\epsilon$  perpendicular to the axis of the Paul trap and let the ion interact for  $\tau = 8 \text{ s}$  with an atom cloud with  $n_{\text{at}} \approx 1.0 \times 10^{12} \text{ cm}^{-3}$ . We find  $P_{\text{threebody}}$  to increase roughly by a factor of 5 when reducing  $\epsilon$  from 3.25 V/m to 0 V/m (Fig. 5.4a).

In order to express the electric field values in terms of kinetic energy we make use of the relation  $E_{\text{eMM}} = c_{\text{trap}} \cdot \epsilon^2 + E_{\text{res}}$  with  $c_{\text{trap}}$  being a constant that depends on the trap configuration and the ion mass [74].  $E_{\text{res}}$  stands for residual uncompensated micromotion energy. The ion energy can be expressed as  $E_{\text{ion}} = c_{\text{dyn}} \cdot E_{\text{eMM}}$  [112].  $c_{\text{dyn}}$

is a constant which depends on the atom-ion mass ratio and the spatial extension of the atom cloud and for our experiments can be estimated to be about 2 [20]. We attempt to describe our data with a power-law dependence of the form  $K_3 \propto E_{\text{ion}}^\alpha$  within our simulation. Good agreement with the data is achieved for  $\alpha = -0.43$ ,  $E_{\text{res}} = 370 \mu\text{K} \cdot k_{\text{B}}$  and a maximal value for  $K_3$  of  $2.75 \times 10^{-25} \text{ cm}^6/\text{s}$  (solid trace in Fig. 5.4b). For comparison, curves for exponents  $\alpha = -0.5$  and  $\alpha = -0.33$  (dashed and dotted traces, respectively) are shown as well. A residual energy  $E_{\text{res}} = 370 \mu\text{K} \cdot k_{\text{B}}$  is a reasonable value for our current setup and in agreement with other measurements of ours [111].

In conclusion, we have studied three-body recombination involving a single trapped ion and two of its parent atoms at collision energies approaching the sub-mK regime. With a relatively simple model we can understand the two- and three-body collision dynamics and extract corresponding rate coefficients. We observe an increase of the three-body rate coefficient with decreasing collision energy, a behavior that can be expected to become crucial for future experiments targeting even lower temperatures. After a three-body event, ion energies on the order of 0.4 eV were measured, indicating that deeply bound molecules have been created. Since we have not observed  $\text{Rb}_2^+$  ions, the formation of  $\text{Rb}_2$  seems probable. The ion would then act as an atomic size catalyzer at mK temperatures.

The authors would like to thank Kilian Singer, Piet Schmidt, David Hume, Olivier Dulieu and Brett Esry for helpful discussions and information. This work was supported by the German Research Foundation DFG within the SFB/TRR21.

## 5.6 Supplemental Material

### 1. Method to determine $P_{\text{threebody}}$

$P_{\text{threebody}}$  is the probability for at least one three-body process to happen within time  $\tau$ . We describe here in more detail how we extract  $P_{\text{threebody}}$  from an atom number histogram. Fig. 5.5 shows such a histogram which consists of two components: a Gaussian distribution on the left hand side and a tail on the right hand side. We assume that only counts outside the Gaussian (i.e. within the tail) correspond to experimental runs with atom-atom-ion three-body events. Then,

$$P_{\text{threebody}} = \frac{\text{Sum of all counts in the tail}}{\text{Total number of counts of histogram}} .$$

A Gaussian fit to the peak on the left hand side of the histogram separates the tail

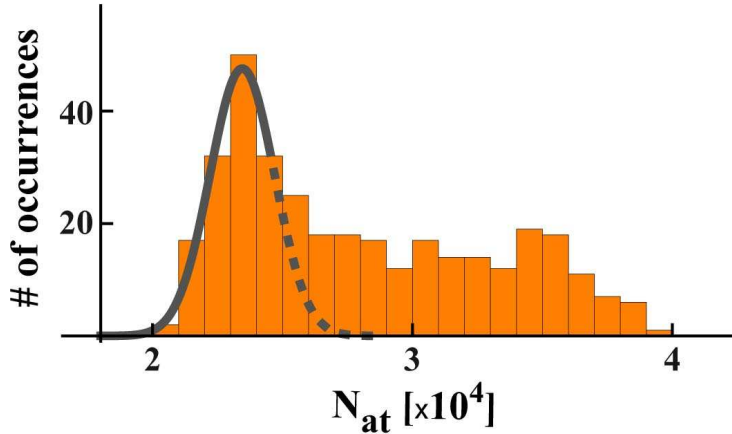


Figure 5.5: Illustration of the fit method used to determine  $P_{\text{threebody}}$ . The histogram shown is taken from Fig. 1 of the main text ( $\tau = 4$  s).

from the Gaussian distribution. For the fit we use the data points roughly up to the top of the peak of the distribution (solid line in the figure). In addition, we estimate the uncertainty of  $P_{\text{threebody}}$ . For this, we vary the number of columns used for the fit and record the corresponding fluctuations of the fit results.

## 2. Description of the numerical simulation

Based on Monte Carlo techniques, we have implemented a simple numerical simulation of the atom-ion interactions. The simulation takes into account the binary atom-ion collisions leading to atom loss, recooling of the ion and the three-body events which eject the ion from the atom cloud.

Initially the ion is positioned at the center of the atom cloud. Time advances in small steps  $\Delta t$ . The evolution of atom number  $N_{\text{at}}$  and density  $n_{\text{at}}$  (for the time being) follows

$$N_{\text{at}}(t + \Delta t) = N_{\text{at}}(t) - K_2 n_{\text{at}}(t) \Delta t$$

and

$$n_{\text{at}}(t + \Delta t) = n_{\text{at}}(t) \frac{N_{\text{at}}(t + \Delta t)}{N_{\text{at}}(t)} .$$

Thus, in our simple model two-body collisions lead to an exponential decay of the atom number, which is a sufficiently good approximation of the observed behavior. We neglect ion-induced temperature changes of the atom cloud which would lead to corrections of the density evolution.

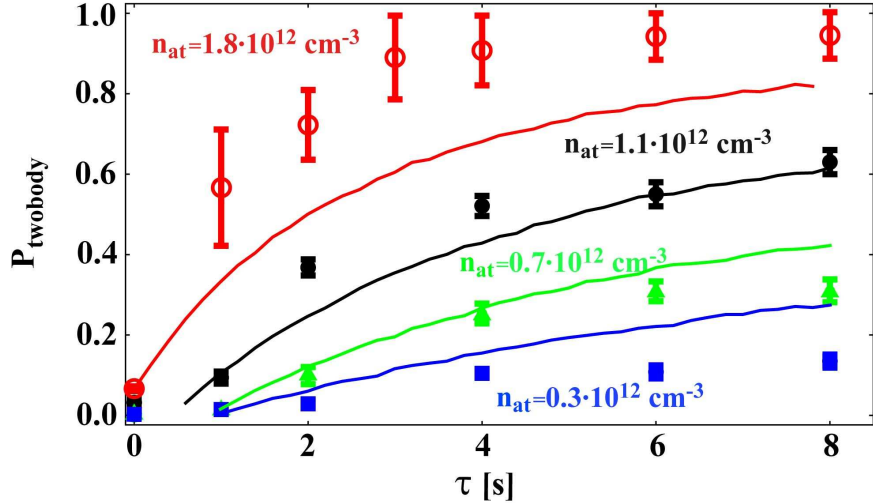


Figure 5.6: Data points from Fig. 2c of the main text and results of simulations of the ion ejection as two-body events.

The possibility of a three-body event is included in the simulation in a probabilistic way. We compute

$$\wp_{\text{threebody}} = K_3 n_{\text{at}}(t)^2 \Delta t$$

which is the probability that within the time step  $\Delta t$  a three-body event will take place. If the three-body event does happen, the simulation stops the evolution of  $N_{\text{at}}$  and  $n_{\text{at}}$  until a reentry of the ion into the atom cloud takes place. The probability for the reentry within a time step  $\Delta t$  is

$$\wp_{\text{reentry}} = \frac{N_{\text{at}}(t)}{c_{\text{out}}} \Delta t.$$

The simulation runs until the total interaction time  $\tau$  is reached. By performing many runs of the simulation we arrive at the atom number distribution in figure 2b and the averaged values for  $P_{\text{threebody}}$  in figures 2c and 4 of the main text.

### 3. Modelling of the ion ejections as two-body events

An important test of our interpretation of the experimental data is the comparison with a model that does not contain three-body collisions. Instead, events sending the ion onto large orbits are also modelled as two-body processes. We can adapt our simulation of the previous section by simply replacing the probability density

$\phi_{\text{threebody}}$  by  $\phi_{\text{twobody}}^*$  where

$$\phi_{\text{twobody}}^* = K_2^* n_{\text{at}}(t) \Delta t . \quad (5.1)$$

Fig. 5.6 shows the simulation results using a best fit value of  $K_2^* = 2.0 \times 10^{-13} \text{ cm}^3/\text{s}$ . While a data set for a single density can still be described reasonably well, this clearly does not work for all four sets with a single  $K_2^*$  rate constant. Thus we exclude two-body interactions as the cause of the ion-ejection.

# Chapter 6

## Shedding Light on Three-Body Recombination in an Ultracold Atomic Gas

arXiv:1301.5518 (2013)

Arne Härter<sup>1</sup>, Artjom Krükow<sup>1</sup>, Markus Deiß<sup>1</sup>, Björn Drews<sup>1</sup>,  
Eberhard Tiemann<sup>2</sup> and Johannes Hecker Denschlag<sup>1</sup>

<sup>1</sup>*Institut für Quantenmaterie und Center for Integrated Quantum Science and Technology IQ<sup>ST</sup>, Universität Ulm, 89069 Ulm, Germany*

<sup>2</sup>*Institut für Quantenoptik, Leibniz Universität Hannover, 30167 Hannover, Germany*

Three-body recombination is a prime example of the fundamental interaction between three particles and it is of importance to the physics of ultracold gases. Due to the complexity of this process it has resisted a comprehensive theoretical description. Experimental investigations have mainly focussed on the observation of corresponding loss rates without revealing information on the reaction products. Here, we provide the first general experimental study on the population distribution of molecular quantum states after three-body recombination. We utilize a novel

detection scheme which combines photoionization of the molecules with subsequent ion trapping. By analyzing the ionization spectrum, we identify the population of energy levels with binding energies up to  $h \times 750$  GHz. We find a broad population of electronic and nuclear spin states and determine a range of populated vibrational and rotational states. The method presented here can be expanded to provide a full survey of the products of the recombination process. This may be pivotal in developing an in-depth model of the underlying three-body dynamics.

## 6.1 Introduction

While cold collisions of two atoms are understood to an excellent degree, the addition of a third collision partner drastically complicates the interaction dynamics. In the context of Bose-Einstein condensation in atomic gases, three-body recombination plays a crucial role [106–108, 113] and it constitutes a current frontier of few-body physics [114–116]. However, the investigations focussed mainly on the atom loss rates established by the recombination events. Discussions of the final states populated in the recombination process were restricted to the special case of large two-body scattering lengths [117, 118] and culminated in the prediction and observation of Efimov resonances [119–121]. In general, recombination processes are of fundamental interest in various physical systems [106, 122, 123]. The control and tunability of ultracold atomic systems provides an experimental testbed for a detailed understanding of the nature of these processes.

Here, we demonstrate the probing of molecules with binding energies up to  $h \times 750$  GHz (where  $h$  is Planck’s constant) generated via three-body recombination of ultracold thermal  $^{87}\text{Rb}$  atoms. We produce the atomic sample in an optical dipole trap located within a linear Paul trap. The recombination and detection process is illustrated in Fig. 6.1a-d. Following a recombination event, the created  $\text{Rb}_2$  molecule can undergo resonance-enhanced multi-photon ionization (REMPI) by absorbing photons from the dipole trap laser at a wavelength around 1064.5 nm. The ion is then captured in the Paul trap and detected essentially background-free with very high sensitivity on the single particle level. Fig. 6.1e shows a simplified scheme of the  $\text{Rb}_2$  and  $\text{Rb}_2^+$  potential energy curves. From weakly-bound molecular states three photons suffice to reach the molecular ionization threshold. An additional photon may dissociate the molecular ion. By scanning the frequency of the dipole trap

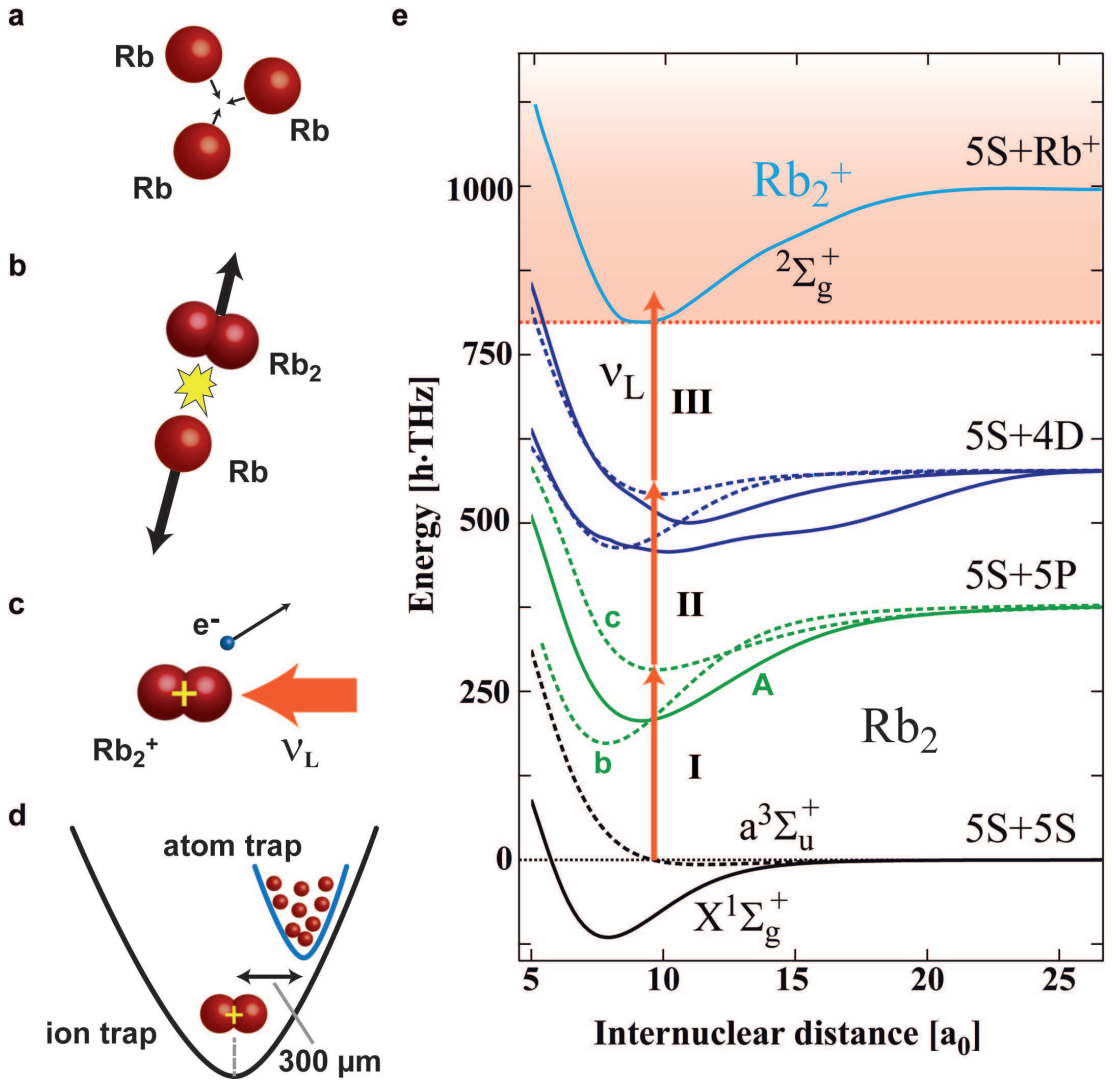


Figure 6.1: Illustration of recombination and ionization in the atom-ion trap. **a**, A three-body collision in the ultracold gas of <sup>87</sup>Rb atoms leads to a recombination event in which, **b**, a Rb<sub>2</sub> molecule is formed with high kinetic energy. **c**, While the atom is lost from the trap, the molecule can be photoionized in a REMPI process and trapped in the Paul trap. **d**, The relative positions of the atom and ion trap centers are shifted by about 300  $\mu$ m to avoid atom-ion collisions. **e**, Potential energy curves of the Rb<sub>2</sub> and Rb<sub>2</sub><sup>+</sup> molecule adapted from refs [124, 125]. The internuclear distance is given in units of Bohr radii  $a_0$ . A REMPI path with three photons is shown. It can create Rb<sub>2</sub><sup>+</sup> ions in vibrational states up to  $v \approx 17$ .

laser by more than 60 GHz we obtained a high resolution spectrum featuring more than 100 resonance peaks. This dense and complex spectrum contains information which vibrational, rotational and hyperfine levels of the Rb<sub>2</sub> molecule are populated. We present an analysis of these data and make a first assignment of the most prominent resonances. This assignment indicates that in the recombination events a broad range of levels is populated in terms of vibrational, rotational, electronic and nuclear spin quantum numbers.

## 6.2 Experimental scheme

Our experimental scheme to detect cold molecules makes use of the generally excellent detection efficiencies attainable for trapped ions. It is related to proven techniques where photoassociated cold molecules in magneto-optical traps were photoionized from the singlet and triplet ground states [23, 124, 126–128] (see also ref [129]). Our method is novel as it introduces the usage of a hybrid atom-ion trap which significantly improves the detection sensitivity. We perform the following experimental sequence. A thermal atomic sample typically containing  $N_{\text{at}} \approx 5 \times 10^5$  spin-polarized <sup>87</sup>Rb atoms in the  $|F = 1, m_F = -1\rangle$  hyperfine state is prepared in a crossed optical dipole trap at a magnetic field of about 5 G. The trap is positioned onto the nodal line of the radiofrequency field of a linear Paul trap. Along the axis of the Paul trap the centers of the atom and ion trap are separated by about 300  $\mu\text{m}$  to avoid unwanted atom-ion collisions (Fig. 6.1d). At atomic temperatures of about 700 nK and peak densities  $n_0 \approx 5 \times 10^{13} \text{ cm}^{-3}$  the total three-body recombination rate in the gas is  $\Gamma_{\text{rec}} = L_3 n_0^2 N_{\text{at}} / 3^{5/2} \approx 10 \text{ kHz}$ . Here, the three-body loss rate coefficient  $L_3$  was taken from ref [113]. At the rate  $\Gamma_{\text{rec}}$ , pairs of Rb<sub>2</sub> molecules and Rb atoms are formed as final products of the reactions. Both atom and molecule would generally be lost from the trap due to the comparatively large kinetic energy they gain in the recombination event (in our case typically on the order of a few K  $\times k_{\text{B}}$  where  $k_{\text{B}}$  is the Boltzmann constant). The molecule, however, can be state-selectively ionized in a REMPI process driven by the dipole trap laser. These molecular ions remain trapped in the deep Paul trap and are detected with single particle sensitivity (see Methods). In each experimental run, we hold the atomic sample for a time  $\tau \approx 10 \text{ s}$ . After this time we measure the number of produced ions in the trap from which we derive (after averaging over tens of runs) the ion production rate  $\Gamma_{\text{ion}}$  normalized to a cloud atom number of  $10^6$  atoms.

As a consistency check of our assumption that  $\text{Rb}_2$  molecules are ionized in the REMPI process, we verify the production of  $\text{Rb}_2^+$  molecules. For this, we perform ion mass spectrometry in the Paul trap (see Methods). We detect primarily molecular  $\text{Rb}_2^+$  ions, a good fraction of atomic  $\text{Rb}^+$  ions but no  $\text{Rb}_3^+$  ions. Our experiments show that  $\text{Rb}^+$  ions are produced in light-assisted collisions of  $\text{Rb}_2^+$  ions with Rb atoms on timescales below a few ms. Details of this dissociation mechanism are currently under investigation and will be discussed elsewhere.

## 6.3 Dependence of the ion production on atomic density, laser frequency and laser intensity

In the following, we analyze the dependence of the ion production rate on atomic density as well as on laser frequency and intensity. This will ultimately help understand the three-body recombination process.

### 6.3.1 Density dependence

By investigating the dependence of the ion production rate on atomic density, we verify that three atoms are originally involved in the reaction. For this measurement, the density is mainly adjusted by varying the cloud atom number while keeping the light intensity of the dipole trap constant. We find the obtained data (Fig. 6.2) to be in good agreement with a fit curve assuming a simple quadratic dependence  $\Gamma_{\text{ion}} \propto n_0^2$ . Thus, a three-body process marks the starting point of the ionization process.

### 6.3.2 Dependence on laser frequency - REMPI spectrum

Next, we investigate the dependence of the ion production rate on the wavelength of the narrow-linewidth dipole trap laser (see Methods). We scan the wavelength over a range of about 0.3 nm around 1064.5 nm, corresponding to a frequency range of about 60 GHz. Typical frequency step sizes are 50 MHz or 100 MHz. We obtain a rich spectrum of resonance lines which is shown in Fig. 6.3a. The quantity  $\bar{\Gamma}_{\text{ion}}$  denotes the ion production rate normalized to the atom number of the cloud and to

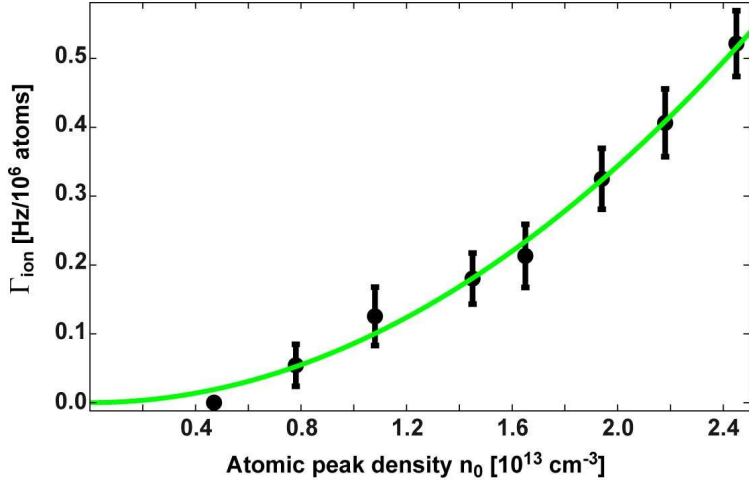


Figure 6.2: Dependence of the ion production rate  $\Gamma_{\text{ion}}$  on atomic density.  $\Gamma_{\text{ion}}$  is normalized to a cloud atom number of  $10^6$  atoms. The data are well described by a quadratic fit (solid green line). They were taken at a constant dipole trap laser intensity  $I_L = 36 \text{ kW/cm}^2$ .

the square of the atomic peak density.

We find strongly varying resonance strengths and at first sight fairly irregular frequency spacings. In the following we will argue that most resonance lines can be attributed to respective well-defined molecular levels (resolving vibrational, rotational and often even hyperfine structure) that have been populated in the recombination process. These levels are located in the triplet or singlet ground state,  $a^3\Sigma_u^+$  and  $X^1\Sigma_g^+$ , respectively. The relatively dense distribution of these lines reflects that a fairly broad range of states is populated. A direct assignment of the observed resonances is challenging, as it hinges on the precise knowledge of the level structure of all the relevant ground and excited states. In the following we will access and understand the data step by step.

One feature of the spectrum that catches the eye is the narrow linewidth of many lines. For example, Fig. 6.3b shows a resonance of which the substructures have typical half-widths  $\Delta\nu_r \approx 50 \text{ MHz}$ . This allows us to estimate the maximal binding energy of the molecules involved. Since the velocity of the colliding ultracold atoms is extremely low, the kinetics of the recombination products is dominated by the released molecular binding energy  $E_b$ . Due to energy and momentum conservation the molecules will be expelled from the reaction with a molecular velocity  $v_{\text{Rb}2} = \sqrt{2E_b/(3m_{\text{Rb}2})}$  where  $m_{\text{Rb}2}$  is the molecular mass. The molecular resonance

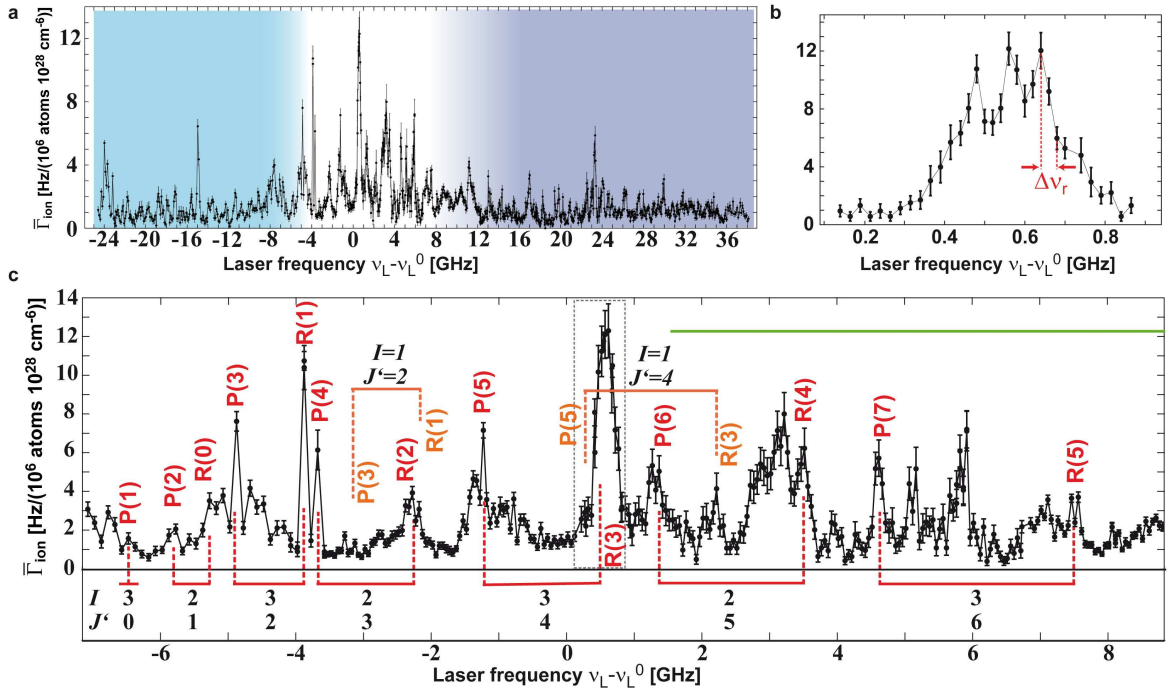


Figure 6.3: REMPI spectrum. **a**, A scan of the dipole trap laser frequency  $\nu_L$  over more than 60 GHz around an offset frequency  $\nu_L^0 = 281.610$  THz shows a multitude of resonance lines. Each data point is the result of 30 to 60 repetitions of the experiment with ion detection on the single particle level. The total spectrum was obtained over a time span of 2 months. Checks of the long-term consistency of resonance positions and strengths were performed. Spectral regions dominated by transitions to  $c^3\Sigma_g^+$  are indicated by the shaded areas in dark and light blue ( $0_g^-$  and  $1_g$  component, respectively). **b**, High-resolution scan of the strong resonance at  $\nu_L - \nu_L^0 \approx 0.5$  GHz. **c**, Central spectral region with assigned P/R branches of the transition  $X^1\Sigma_g^+(v = 115) \rightarrow A^1\Sigma_u^+(v' = 68)$ . The corresponding quantum numbers  $I$  and  $J'$  are given). P( $J$ ) marks the transition  $J \rightarrow J + 1$ , R( $J$ ) the transition  $J \rightarrow J - 1$ . The region where also transitions to  $b^3\Pi_u$  appear is marked by a green horizontal bar.

frequency  $\nu_0$  will then be Doppler-broadened following a distribution with half-widths  $\Delta\nu_D = \sqrt{3}\nu_0 v_{\text{Rb}2}/2c$ . Here,  $c$  is the speed of light. By comparing  $\Delta\nu_D$  to the observed values of  $\Delta\nu_r$  we estimate a maximal binding energy of  $E_{\text{b},\text{max}} \approx h \times 2.5 \text{ THz}$ . This simple analysis overestimates the value  $E_{\text{b},\text{max}}$  since it neglects the natural linewidth of the transition and possible saturation broadening. Still, it already strongly constrains the possible populated molecular levels that are observed in our experiment.

### 6.3.3 Dependence on laser intensity

Next, we investigate the dependence of the ion production rate on laser intensity  $I_L$ . In our experimental setup, this measurement is rather involved because the laser driving the REMPI process also confines the atomic cloud. Thus, simply changing only the laser intensity would undesirably also change the density  $n_0$  of the atoms. To prevent this from happening we keep  $n_0$  constant ( $n_0 \approx 5 \times 10^{13} \text{ cm}^{-3}$ ) by adjusting the atom number and temperature appropriately. Due to these experimental complications we can only vary  $I_L$  roughly by a factor of 2 (Fig. 6.4a). We set the laser frequency to the value of  $\nu_L = \nu_L^0 \equiv 281610 \text{ GHz}$ , on the tail of a large resonance (see Fig. 6.3). The atomic temperatures in this measurement range between 500 nK and  $1.1 \mu\text{K}$ , well above the critical temperatures for Bose-Einstein condensation. The atomic densities can therefore be described using a Maxwell-Boltzmann distribution. Assuming a simple power-law dependence of the form  $\bar{\Gamma}_{\text{ion}} \propto I_L^\alpha$  we obtain the best fit using an exponent  $\alpha = 1.5(1)$  (solid green line in Fig. 6.4a). This fit is between a linear and a quadratic intensity dependence (dashed red and blue lines, respectively). Thus, at least two of the three transitions composing the ionization process are partially saturated at the typical intensities used.

In order to better circumvent possible density variations of the atomic cloud induced by changes in laser intensity, we employ a further method which enables us to vary the intensity with negligible effects on the atomic sample. We achieve this by keeping the time-averaged intensity  $\langle I_L \rangle$  constant and comparing the ion production rates in a continuous dipole trap with a "chopped" dipole trap in which the intensity is rapidly switched between 0 and  $2I_L$ . In both cases the trap is operated at an intensity  $\langle I_L \rangle \approx 15 \text{ kW/cm}^2$ . In the "chopped" configuration the intensity is switched at a frequency of 100 kHz so that the atoms are exposed to the light for  $5 \mu\text{s}$  followed by  $5 \mu\text{s}$  without light. It should be noted that molecules formed in the "dark" period with sufficiently high kinetic energies may leave the central trapping region before the laser light is switched back on. They are then lost for our REMPI detection.

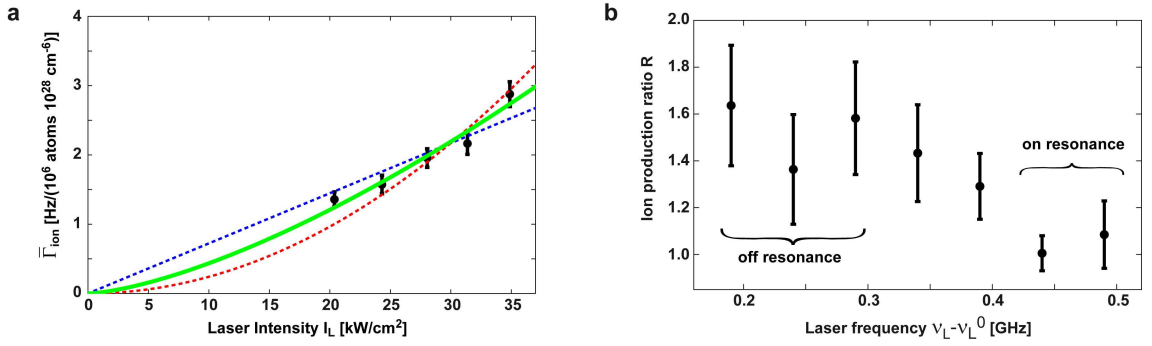


Figure 6.4: Dependence of the ion production rate on the intensity of the dipole trap laser. **a**, Assuming a power-law dependence  $\bar{\Gamma}_{\text{ion}} \propto I_L^\alpha$ , the best fit to the data is achieved for  $\alpha \approx 1.5$  (solid green line). Linear and quadratic fits are also given (blue and red dashed lines, respectively). **b**, Measurement of the intensity dependence using a "chopped" dipole trap. The ratio  $R \approx 1$  on resonance indicates saturation of both transitions I and II.

Taking into account the molecular velocity and the transverse extensions of the laser beams we can estimate that this potential loss mechanism leads to errors of less than 30%, even at the highest binding energies relevant to this work ( $E_b \approx h \times 750$  GHz, see below). We did not observe evidence of such losses experimentally. Investigations were made by changing the chopping frequency. We define  $R$  as ratio of the ion production rates in the "chopped" and the continuous trap configuration. Fig. 6.4b shows the results of these measurements for various laser frequencies  $\nu_L$ . We find a value  $R \approx 1.5$  for off-resonant frequency settings  $\nu_L - \nu_L^0 < 0.4$  GHz, in good agreement with the result presented in Fig. 6.4a. When scanning the laser onto resonance at  $\nu_L - \nu_L^0 \approx 0.45$  GHz (see also Fig. 6.3b) we obtain  $R \approx 1$ . This result indicates a linear intensity dependence of the REMPI process in the resonant case, which is explained by the saturation of two of the three molecular transitions involved. It is known that transitions into the ionization continuum (photon III, see Fig. 6.1e) will not saturate under the present experimental conditions. This means that the excitation pathway via photon I and II must be saturated and therefore on resonance. However, an inspection of the level structure shows that photon I can only resonantly reach three vibrational levels which correlate to the  $5s + 5p$  asymptote. This is largely due to its long wavelength of 1064.5 nm. For example, within the  $c^3\Sigma_g^+$  state only the lowest ( $v' = 0$ ) vibrational level can be excited, namely from level  $v = 26$  of  $a^3\Sigma_u^+$  which has a binding energy of  $E_b \approx h \times 516$  GHz. The other two excited vibrational levels are the  $v' = 68$  of  $A^1\Sigma_u, 0_u^+$  and  $v' = 72$  of  $b^3\Pi_u, 0_u^+$ . The dipole trap laser

couples these levels resonantly to  $v = 115$  of  $X^1\Sigma_g^+$  (binding energy  $\approx 161 \text{ GHz} \times h$ ) and  $v = 109$  of  $X^1\Sigma_g^+$  (binding energy  $\approx 754 \text{ GHz} \times h$ ), respectively (see Fig. 6.5 for details). Coupling to other nearby  $a$  or  $X$  ground state levels can be neglected due to weak transition strengths, resulting from small Franck-Condon factors or dipole selection rules. We note that there is a strong mixing of  $A^1\Sigma_u^+$  and  $b^3\Pi_u$  due to spin-orbit coupling. The transitions that we consider exhibit large enough Franck-Condon factors (typ.  $10^{-2}\dots 10^{-3}$ ) so that at laser powers of  $\approx 10^4 \text{ W/cm}^2$  resonant transitions can be well saturated.

## 6.4 Assignment of observed resonances to molecular transitions

From recent spectroscopic studies [130–132] and additional measurements in our lab [133] the level structure of all relevant levels of the  $X, a, A, b$ , and  $c$  states is well known. The absolute precision of most of the level energies is far better than 1 GHz for low rotational quantum numbers  $J$ . Spin-orbit and effective spin-spin coupling in the  $A, b$ , and  $c$  states lead to Hund’s case c coupling where the relevant levels of states  $A$  and  $b$  have  $0_u$  symmetry while the levels of state  $c^3\Sigma_g^+$  are grouped into  $0_g^-$  and  $1_g$  components. The level structure of the  $0_u^+$  states is quite simple as it is dominated by rotational splittings. Typical rotational constants for the electronically excited states are on the order of 400 MHz, for the weakly bound  $X$  and  $a$  states they are around 100-150 MHz.

In the experimental data (Fig. 6.3a) the central region from  $\nu_L - \nu_L^0 = -6$  to 7 GHz is marked by several prominent resonances that are significantly stronger than those observed throughout the rest of the spectrum. These resonance peaks can be explained by transitions from the  $X$  ground state to  $A$  and  $b$  states. The prominence of these singlet transitions is explained by the degeneracy of levels due to small hyperfine splittings. Indeed, by analyzing these strong resonances with regard to line splittings and intensities it was possible to consistently assign rotational ladders for total nuclear spin quantum numbers  $I = 1, 2, 3$  for the transition  $X^1\Sigma_g^+(v = 115) \rightarrow A^1\Sigma_u^+(v' = 68)$ . For the weakly bound  $X$  states, the  $I$  quantum numbers are approximately good. For  $I = 1, 3$  the total parity of the molecule is negative, while for  $I = 0, 2$  the parity is positive. The starting point of the rotational ladder is fixed by the already mentioned additional spectroscopic measurements [133]. In Fig. 6.3c the P branch and the R branch of the rotational ladders are

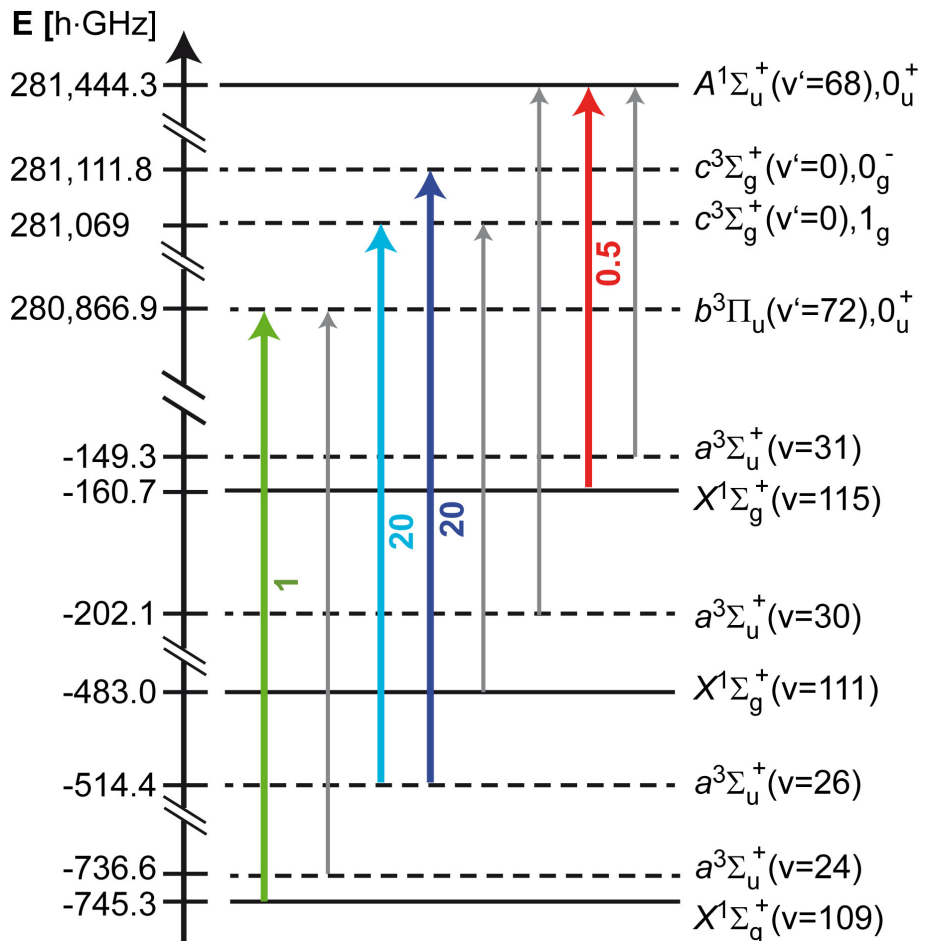


Figure 6.5: Overview over relevant molecular transitions. The energy  $E$  of the energetically lowest levels of each vibrational manifold is given with respect to the  $5s5s$  asymptote. Colored thick arrows represent molecular transitions relevant to the spectrum of Fig. 6.3. The expected relative strengths of these transitions are also given. Here we only consider Franck-Condon factors and mixing of singlet and triplet, while electronic transition moments are ignored. Grey arrows mark transitions that occur in the relevant spectral region but are very weak. We identify three main molecular transitions for the initial step of the REMPI process. (1) Molecules in the  $v = 26$  vibrational level of the  $a^3\Sigma_u^+$  potential are excited to the  $v' = 0$  level of the  $c^3\Sigma_g^+$  potential. This level is split into a  $1_g$  and a  $0_g^-$  component. (2) Excitation from  $X^1\Sigma_g^+(v = 115)$  to  $A^1\Sigma_u^+(v' = 68)$ . (3) Excitation from  $X^1\Sigma_g^+(v = 109)$  to  $b^3\Pi_u(v' = 72)$ . Transition (3) becomes possible through the strong spin-orbit coupling of the  $A$  and  $b$  states.

indicated. These lines can be grouped into pairs sharing the same  $J'$  of the excited state and  $I$  quantum number. At frequencies  $\nu_L - \nu_L^0 \gtrsim 2$  GHz additional strong lines appear that we attribute to the  $X^1\Sigma_g^+(v = 109) \rightarrow b^3\Pi_u(v' = 72)$  transition. We can now roughly estimate the range of molecular rotation  $J$  of the populated levels in the ground state. The strong isolated lines that we have assigned to the  $X^1\Sigma_g^+ \rightarrow A^1\Sigma_u^+$  transition are all contained within a relatively small spectral region ( $|\nu_L - \nu_L^0| < 6$  GHz) and are explained by rotational quantum numbers  $J \leq 7$ . Population of higher rotational quantum numbers would result in a continuation of the strong resonance lines stretching to transition frequencies beyond  $\nu_L - \nu_L^0 = 10$  GHz, which we do not observe. Similarly, if only rotational quantum numbers  $J \leq 5$  were populated, a spectrum would result which does not have enough lines to explain the data. Thus, we can roughly set the limits on the molecular rotation to  $J \leq 7$ . These results are consistent with our observations of the spread of the transitions  $X \rightarrow b$  and  $a \rightarrow c$  (see Fig. 6.5).

From our measurements we can also make an estimate about the number of molecular vibrational levels populated in the recombination events. For this we integrate over the spectral region dominated by the transition  $X^1\Sigma_g^+(v = 115) \rightarrow A^1\Sigma_u^+(v' = 68)$  and divide by the observed FWHM linewidth ( $\approx 100$  MHz). The result is then divided by a factor of 2 to account for the P and R branch of the transition. For the given atom numbers and atomic densities in our cloud, this yields an estimate for the global ion production rate from this vibrational level. Assuming that the two first transitions of the REMPI process are saturated and using a typical ionization cross section for the third transition to be  $\sim 10$  MBarn [134–136], we obtain an ionization probability of around 10 % for molecules formed in one of the levels susceptible to the REMPI process. From this we can estimate the population rate for the  $X^1\Sigma_g^+(v = 115)$  level due to three-body recombination. It is roughly on the order of 0.2 kHz. We can compare this to the much larger total recombination rate of  $\Gamma_{\text{rec}} = 10$  kHz in the atomic gas. Consequently, our estimate suggests that on the order of 50 vibrational levels, a significant fraction of all the 169 existing levels of the  $X$  and  $a$  states, may be populated in the three-body recombination. This estimate seems reasonable considering that we have observed molecule production down to  $X^1\Sigma_g^+(v = 109)$ , which is located 38 vibrational levels (counting both singlet and triplet states) below the atomic asymptote.

## 6.5 Conclusion

In conclusion, we have carried out a first, detailed experimental study of the molecular reaction products after three-body recombination of ultracold Rb atoms. We use a high-power, narrow-linewidth laser to state-selectively ionize the produced molecules in a REMPI process. Subsequently, these ions are trapped in an ion trap and detected with very high sensitivity and negligible background. An analysis of the ionization spectrum allows us to identify population of several vibrational quantum levels indicating that the recombination events result in a fairly broad and uniform population distribution. We conjecture that dozens of vibrational levels are populated in total. Molecules are produced both in  $X^1\Sigma_g^+$  as well as  $a^3\Sigma_u^+$ , with negative and positive total parity, various total nuclear spins and rotational quantum numbers reaching  $J \leq 7$ . We have made a first assignment of several strong individual spectral lines. Confirming and expanding this assignment to other transitions will require further experimental and theoretical efforts to acquire a more detailed knowledge of the involved molecular levels. Such studies may finally pave the way to a detailed understanding of three-body recombination in the future. Reaching beyond the scope of three-body recombination, the great sensitivity of our detection scheme has enabled us to state-selectively probe single molecules that are produced at rates of only a few Hz. We thereby demonstrate a novel scheme for precision molecular spectroscopy in extremely dilute ensembles.

## 6.6 Methods

### 6.6.1 Dipole trap and REMPI configuration

The crossed dipole trap is composed of a horizontal and a vertical beam focussed to beam waists of  $\sim 90 \mu\text{m}$  and  $\sim 150 \mu\text{m}$ , respectively. It is positioned onto the nodal line of the radiofrequency field of the linear Paul trap with  $\mu\text{m}$  precision. The two trap centers are separated by about  $300 \mu\text{m}$  along the axis of the Paul trap (see Fig. 6.1d). In a typical configuration, the trap frequencies of the dipole trap are  $(175, 230, 80)$  Hz resulting in atom cloud radii of about  $(6, 7, 16) \mu\text{m}$ . The short-term frequency stability of the dipole trap laser source is on the order of 1 kHz and it is stabilized against thermal drifts to achieve long-term stability of a few MHz. The two beams of the dipole trap are mutually detuned by 160 MHz to avoid interference

effects in the optical trap. Consequently, two frequencies are in principle available to drive the REMPI process. However, the intensity of the horizontal beam is 4 times larger than the one of the vertical beam and we have not directly observed a corresponding doubling of lines. Further details on the atom-ion apparatus are given in ref [110].

### 6.6.2 Paul trap configuration

The linear Paul trap is driven at a radiofrequency of 4.17 MHz and an amplitude of about 500 V resulting in radial confinement with trap frequencies of  $(\omega_{x,Ba}, \omega_{y,Ba}) = 2\pi \times (220, 230)$  kHz for a  $^{138}\text{Ba}^+$  ion. Axial confinement is achieved by applying static voltages to two endcap electrodes yielding  $\omega_{z,Ba} = 2\pi \times 40.2$  kHz. The trap frequencies for "dark"  $\text{Rb}_2^+$  and  $\text{Rb}^+$  ions produced in the REMPI processes are  $(m_{\text{Ba}}/m_{\text{dark}} \times \omega_{x,Ba}, m_{\text{Ba}}/m_{\text{dark}} \times \omega_{y,Ba}, \sqrt{m_{\text{Ba}}/m_{\text{dark}}} \times \omega_{z,Ba})$  where  $m_{\text{Ba}}$  and  $m_{\text{dark}}$  denote the mass of the  $\text{Ba}^+$  ion and the dark ion, respectively. The depth of the Paul trap depends on the ionic mass and exceeds 2 eV for all ionic species relevant to this work.

### 6.6.3 Ion detection methods

We employ two methods to detect  $\text{Rb}_2^+$  and  $\text{Rb}^+$  ions both of which are not amenable to fluorescence detection. In the first of these methods we use a single trapped and laser-cooled  $^{138}\text{Ba}^+$  ion as a probe. By recording its position and trapping frequencies in small ion strings with up to 4 ions we detect both the number and the masses of the ions following each REMPI process (see also [16]). The second method is based on measuring the number of ions in the Paul trap by immersing them into an atom cloud and recording the ion-induced atom loss after a hold time of 2 s (see also [32]). During this detection scheme, we take care to suppress further generation of ions by working with small and dilute atomic clouds and by detuning the REMPI laser from resonance. Both methods are background-free in the sense that no ions are captured on timescales of days in the absence of the atom cloud. Further information on both detection methods is given in the Supplementary Information.

The authors would like to thank Stefan Schmid and Andreas Brunner for support during early stages of the experiment and Olivier Dulieu, Brett Esry, William

Stwalley, Ulrich Heinzmann, Jeremy Hutson, Pavel Soldan, Thomas Bergeman and Anastasia Drozdova for valuable information and fruitful discussions.

## 6.7 Supplementary Information

In this Supplementary Information we describe two methods that we employ to detect small numbers of  $\text{Rb}_2^+$  and  $\text{Rb}^+$  ions in our linear Paul trap.

### 6.7.1 Ion detection method 1

To implement our first ion detection method allowing mass-sensitive detection of "dark" ions we rely on the presence of a single "bright" ion in the trap. Information on additional ions can be extracted from its fluorescence position. When using this method, our experimental procedure begins with the loading of a single  $^{138}\text{Ba}^+$ -ion into our linear Paul trap. We laser-cool the ion and image its fluorescence light onto an electron-multiplying charge-coupled device camera. This enables us to determine the position of the trap center to better than 100 nm. The ion is confined at radial and axial trapping frequencies  $\omega_{r,\text{Ba}} \approx 2\pi \times 220 \text{ kHz}$  and  $\omega_{ax,\text{Ba}} \approx 2\pi \times 40.2 \text{ kHz}$  and typically remains trapped on timescales of days. Next, we prepare an ultracold atomic sample in the crossed dipole trap. At typical atomic temperatures of about 700 nK the atom cloud has radial and axial extensions of about  $7 \mu\text{m}$  and  $15 \mu\text{m}$  and is thus much smaller than the trapping volume of our Paul trap. To avoid atom-ion collisions we shift the  $\text{Ba}^+$ -ion by about  $300 \mu\text{m}$  with respect to the atom cloud before the atomic sample arrives in the Paul trap. The shifting is performed along the axis of the trap by lowering the voltage on one of the endcap electrodes. Additionally, we completely extinguish all resonant laser light so that the atoms are only subjected to the light of the dipole trap. The atomic sample is moved into the center of the radial trapping potential of the Paul trap and is typically held at this position for a time  $\tau_{\text{hold}} \approx 10 \text{ s}$ . Despite the axial offset from the center of the Paul trap, the atom cloud at this position is fully localized within the trapping volume of the Paul trap. After the hold time the sample is detected using absorption imaging. Subsequently, the ion cooling beams are switched back on for fluorescence detection of the  $\text{Ba}^+$ -ion. The presence of a second ion in the trap leads to positional shifts of the  $^{138}\text{Ba}^+$ -ion

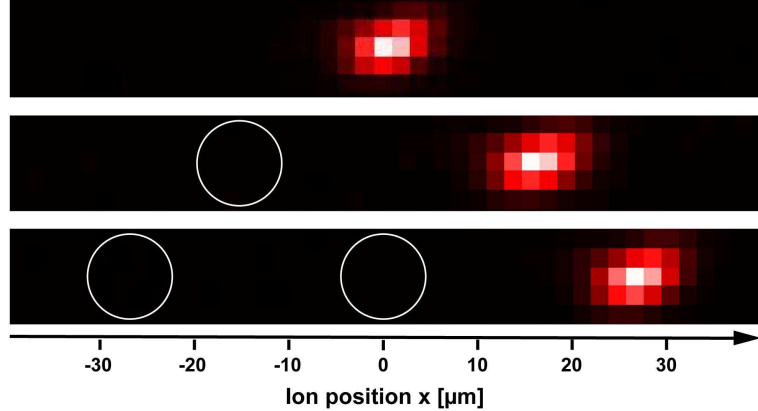


Figure 6.6: Ion detection using a  $^{138}\text{Ba}^+$ -ion. Positional shifts of the fluorescence of the  $\text{Ba}^+$ -ion and measurements of the trap oscillation frequencies allow us to perform mass-sensitive detection of up to three "dark" ions in the trap.

by distances on the order of  $10\mu\text{m}$  (see Fig. 6.6). We make use of the mass-dependent trap frequencies of the Paul trap to gain information on the ion species trapped. In a two-ion Coulomb crystal composed of a  $\text{Ba}^+$ -ion and a dark ion, the axial center-of-mass frequency  $\omega_{\text{ax},2\text{ion}}$  shifts with respect to  $\omega_{\text{ax},\text{Ba}}$  depending on the mass of the dark ion  $m_{\text{dark}}$  [137]. We measure  $\omega_{\text{ax},2\text{ion}}$  by modulating the trap drive at frequencies  $\omega_{\text{mod}}$  and by monitoring the induced axial oscillation of the  $\text{Ba}^+$ -ion, visible as a blurring of the fluorescence signal. In this way, after each ion trapping event, we identify a resonance either at  $\omega_{\text{mod}} \approx 2\pi \times 44\text{ kHz}$  or  $\omega_{\text{mod}} \approx 2\pi \times 38\text{ kHz}$  corresponding to  $m_{\text{dark}} = 87\text{ u}$  and  $m_{\text{dark}} = 174\text{ u}$ , respectively (see table 6.1).

We have expanded this method for ion strings with up to four ions including the  $\text{Ba}^+$ -ion. For this purpose, we perform the following step-by-step analysis.

1. The position  $x$  of the  $\text{Ba}^+$ -ion with respect to the trap center is detected. If  $x \neq 0$ , the value of  $x$  allows us to directly determine the total number of ions in the string.
2. If  $x = 0$  we need to distinguish between a single  $\text{Ba}^+$  ion and a three-ion string with  $\text{Ba}^+$  at its center. This is done by modulating the trap drive at  $\omega_{\text{ax},\text{Ba}}$ , thereby only exciting the  $\text{Ba}^+$  ion if no further ions are present.
3. We destructively detect the  $\text{Rb}^+$  ions by modulating the trap drive on a  $5\text{ kHz}$  wide band around  $2 \times \omega_{\text{r,Rb}}/(2\pi) = 691\text{ kHz}$ . This selectively removes only

Table 6.1: Trap oscillation frequencies of two-ion crystals

Ion species	$\omega_{\text{ax},2\text{ion}}/2\pi$ [kHz]	$\omega_r/2\pi$ [kHz]
$^{138}\text{Ba}^+$ and $^{138}\text{Ba}^+$	40.2	220.0
$^{138}\text{Ba}^+$ and $^{87}\text{Rb}^+$	44.0	345.3
$^{138}\text{Ba}^+$ and $^{87}\text{Rb}_2^+$	37.7	170.7

$\text{Rb}^+$  ions from the string making use of the relatively weak inter-ionic coupling when exciting the ions radially.

4. Steps 1. and 2. are repeated to detect the number of remaining ions.
5. The  $\text{Rb}_2^+$  ions are destructively detected via modulation around  $2 \times \omega_{r,\text{Rb}2}/(2\pi) = 341$  kHz.

### 6.7.2 Ion detection method 2

We have also developed a second ion detection method that does not require an ion fluorescence signal. Instead, the trapped ions are detected via their interaction with an atomic sample. For this purpose, we produce a comparatively small atom cloud containing about  $1 \times 10^5$  atoms at a density of a few  $10^{12} \text{ cm}^{-3}$ . In addition, we set the frequency of the dipole trap laser to an off-resonant value so that the production of additional ions during the ion probing procedure becomes extremely unlikely. We now fully overlap the ion and atom traps for an interaction time  $\tau_{\text{int}} = 2$  s. By applying an external electric field of several V/m we set the ion excess micromotion energy to values on the order of tens of  $k_B \times \text{mK}$  [32, 74]. Consequently, if ions are present in the trap, strong atom losses occur due to elastic atom-ion collisions. Fig.6.7 shows a histogram of the atom numbers of the probe atom samples consisting of the outcome of about 1,000 experimental runs. The histogram displays several peaks which can be assigned to the discrete number of ions in the trap. Up to five ions were trapped simultaneously and detected with high fidelity. The atom loss rate increases nonlinearly with ion number mainly because the interionic repulsion prevents the ions from all occupying the trap center where the atomic density is maximal. While ion detection method 2 does not distinguish ionic masses, it has advantages in terms of experimental stability and does not require the trapping of ions amenable to laser cooling or other fluorescence based detection techniques.

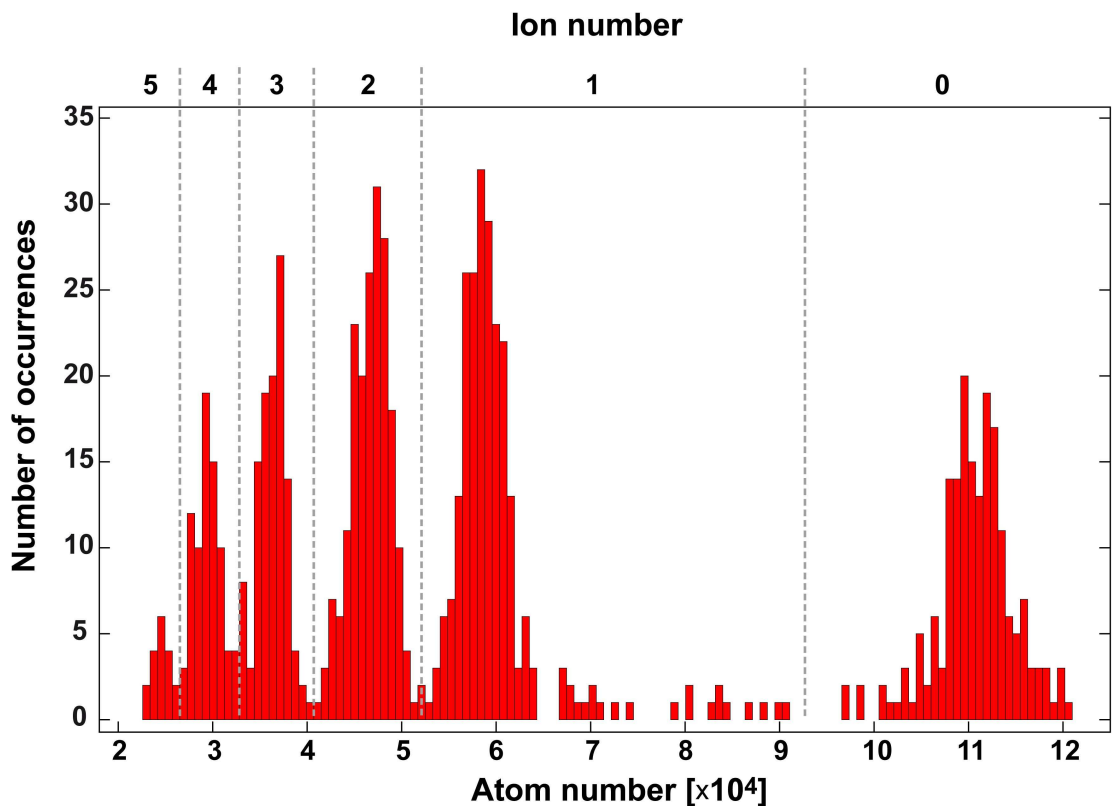


Figure 6.7: Ion detection method based on ion-induced atom loss. We overlap an ultracold atom cloud containing approximately 110,000 atoms with the center of the Paul trap. After an interaction time  $\tau = 2$  s we detect the ion-induced atom loss via absorption imaging of the atom cloud. The discrete number of trapped ions is clearly reflected in the displayed histogram of atom numbers.

# Chapter 7

## Outlook

Focussing on the results obtained in our group, this thesis gives an overview of experimental progress made in cold atom-ion physics over the course of the last few years. The experimental tools and the understanding of the observed physical phenomena have been tremendously improved in this relatively short period of time. However, the described development as a whole can only be seen as a starting point setting the stage for more advanced future investigations in this young field of research. In this final chapter, I will outline some possible routes towards such second generation atom-ion experiments.

### 7.1 Towards ultracold atom-ion experiments

While a plethora of interesting research topics can be explored at the currently accessible atom-ion collision energies, one of the main goals of the field will remain the realization of truly ultracold interactions. The technical possibilities of our apparatus seem well-suited to push the limits further into this direction. Before going into detail on how this can be done, I want to give a general notion of the type of physical processes that can be expected in such a regime.

As detailed in section 1.1, the atom-ion scattering cross section scales with the collision energy as  $E_{\text{col}}^{-\frac{1}{3}}$ . Similarly, we have shown that the three-body coefficient scales roughly as  $E_{\text{col}}^{-0.43}$  (see section 5.5). As this scaling can be expected to be valid down to collision energies of a few  $\mu\text{K}$ , the two-body and the three-body coefficients will increase by one to two orders of magnitude. Thus, the atom-ion system becomes

very strongly interacting, the typical experimentally relevant interaction timescales will decrease and few-body reactions will be of special importance. By tuning the interaction via atom-ion Feshbach resonances [39, 40] these characteristics could be made even more drastic. Predicted effects in this regime include the formation of strong coupling polarons [46] and mesoscopic molecular ions [13]. It may even be possible to realize a regime in which the atom-ion interaction range becomes comparable to the total size of the atomic system. In this scenario, truly many-body interactions depending on a single particle could be observed. Given the general complexity of the dynamics in such strongly interacting systems, further unexpected and fascinating effects seem probable.

## 7.2 An optical dipole trap for Ba<sup>+</sup> ions and Rb atoms

Despite the many advantages of Paul traps, they seem unsuitable for the quest to the lowest possible ionic energies [35]. They may still be of great value for the initial trapping of hot ions and subsequent pre-cooling with lasers or internal state manipulation. In this sense, the Paul trap can be a similar experimental tool for ions as the magneto-optical trap is for atoms. However, optical dipole traps seem the only currently available trapping technique to realize ion cooling beyond the  $\mu\text{K}$  scale. While these traps have been widely used for neutral atoms for more than two decades [138], their successful application to ions is a very recent development [139]. The main difficulty arises because the typically strong electric forces acting on ions have to be overcome by typically weaker dipole forces relying on the AC Stark effect. Hence, excellent control of electric fields at the position of the ion is required to keep the corresponding forces small. In our experiment, we have achieved field compensation down to 0.03V/m, so that the residual electric force acting on the ion is below  $10^{-20}\text{N}$ . Still, to reach dipole forces exceeding this value, strongly focussed laser light with comparatively small detuning  $\Delta_L$  to the ion's resonance frequency is needed.

Of all the ionic species commonly used in ion trapping experiments, Ba<sup>+</sup> ions seem ideally suited for the loading into optical dipole traps. This becomes clear when we compare the two most important trap parameters, namely the depth of the dipole potential  $U_{\text{dip}}$  and the trap-induced heating rate  $\dot{T}$ . With the laser intensity  $I_L$ , the natural linewidth of the atomic transition  $\Gamma$  and the corresponding frequency  $\omega_0$  we

Table 7.1: Comparison of commonly trapped ionic species with regard to their suitability for optical trapping. The parameters  $\kappa_{\text{ion}}$  are normalized to the corresponding value of  ${}^{40}\text{Ca}^+$ .

Ionic species	$\kappa_{\text{ion}}/\kappa_{\text{Ca}}$
${}^{40}\text{Ca}^+$	1.00
${}^{174}\text{Yb}^+$	4.22
${}^9\text{Be}^+$	0.16
${}^{199}\text{Hg}^+$	0.37
${}^{25}\text{Mg}^+$	0.16
${}^{88}\text{Sr}^+$	1.71
${}^{138}\text{Ba}^+$	7.80

find [138]

$$U_{\text{dip}} \propto \frac{\Gamma}{\omega_0^3 \Delta_L} I_L . \quad (7.1)$$

Thus, by reducing the laser detuning, the trap depth can in principle be increased further and further. However, the heating rate induced by photon scattering events will then increase as determined by

$$\dot{T} \propto \frac{\Gamma^2}{m_{\text{ion}} \omega_0 \Delta_L^2} I_L . \quad (7.2)$$

The ratio of the desired trapping potential and the unwanted heating effects consequently reads

$$\frac{U_{\text{dip}}}{\dot{T}} \propto \frac{m_{\text{ion}}}{\omega_0^2 \Gamma} \Delta_L =: \kappa_{\text{ion}} \Delta_L , \quad (7.3)$$

where  $\kappa_{\text{ion}}$  summarizes the suitability of the ion for optical trapping. Table 7.1 gives an overview over this parameter for ions commonly used in laser cooling experiments.

The  $6S_{1/2} \rightarrow 6P_{1/2}$  transition in  ${}^{138}\text{Ba}^+$  has a wavelength  $\lambda_0 \approx 493$  nm. This is an especially long wavelength compared to other ionic species amenable to laser cooling. The transition frequency  $\omega_0 \propto 1/\lambda_0$  is accordingly small, advantageous for optical trapping (see equation 7.3). Similarly, the large mass of 138 u and the relatively narrow linewidth  $\Gamma \approx 2\pi \times 15$  MHz are also in favour of optical trapping with manageable ion heating. It is encouraging that the group of Tobias Schätz [139] reported successful optical trapping of  ${}^{25}\text{Mg}^+$  ions which are among the least suited ionic species for this task (see table 7.1). For  ${}^{138}\text{Ba}^+$  ions, 1 W of laser power with a "red" detuning of  $\Delta_L = -2\pi \times 2$  THz focussed to a beam waist  $w_0 = 7 \mu\text{m}$  generates a trap depth of  $35 \text{ mK} \cdot k_B$  at a heating rate of  $3.5 \text{ mK/s}$  [140]. The maximal force exerted by this trap in radial direction is approximately  $F_{\text{dip}} \approx 8 \times 10^{-20} \text{ N}$ , clearly beating the electric forces in a well compensated configuration.  $F_{\text{dip}}$  depends critically

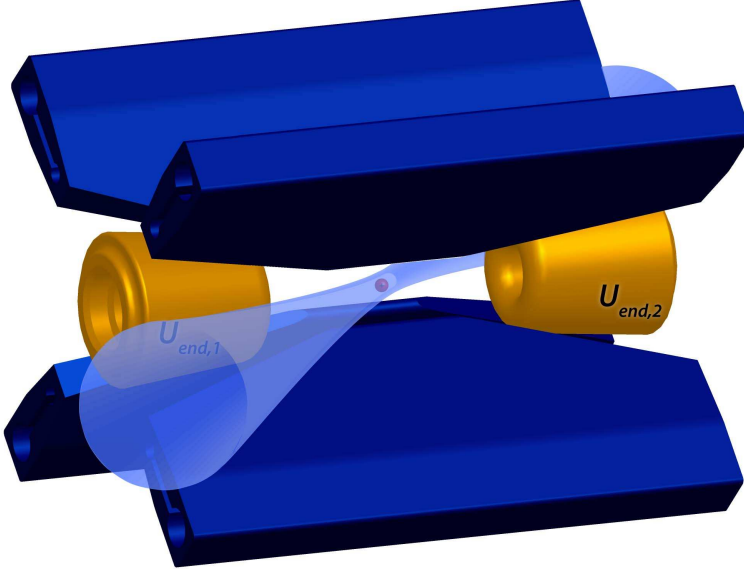


Figure 7.1: Possible configuration for a common dipole trap for atoms and ions. A "blue" detuned donut beam is aligned at a  $45^\circ$  angle to the Paul trap axis and focussed on the ion. Ion trapping in the dimension along the beam is achieved by applying appropriate static voltages to the endcap electrodes of the Paul trap.

on the beam waist ( $F_{\text{dip}} \propto 1/w_0^3$ ), making tight beam focussing mandatory in optical traps for ions.

To perform atom-ion collision experiments in a dipole trap, both species have to experience appropriate optical potentials. In the case outlined above with a "red" detuned trap for  $\text{Ba}^+$ , the Rb atoms would experience a "blue" detuned trap repelling them from the intensity maximum. The resulting potential barrier would have a height of about  $500 \mu\text{K} \cdot k_{\text{B}}$  and would completely shield the ion from the atoms [140]. To overcome this issue, the dipole trap should be "blue" detuned for both species, with a much smaller detuning for  $\text{Ba}^+$  than for Rb. In this way, a common trap for atoms and ions is generated. The trap depth and dipole force are two to three orders of magnitude larger for the ion, owing to the much smaller detuning. A possible dipole trap configuration realizable in our experimental apparatus is shown in Fig. 7.1.

Here, I consider the comparatively simple case of a spherically symmetric beam with an intensity minimum at its center, a so-called donut beam [141, 142]. It can be generated, e.g. by sending a Gaussian beam through a spiral phase plate. In this way, a light phase proportional to the azimuthal angle is imprinted on the beam leading to

destructive interference at the center. In our setup, due to geometrical considerations, such a beam would impinge on the ion at an angle of  $45^\circ$  to the Paul trap axis. Using similar laser power and beam waist as above but changing the sign of the detuning, a dipole trap of sufficient depth and confining force in radial direction is created. However, no confinement is achieved in the dimension along the donut beam. This can be mended by applying appropriate static voltages to the two endcap electrodes of the Paul trap, thereby "plugging" the beam electrostatically. An advantage of a "blue" detuned dipole trap is the lower photon scattering rate due to the lower laser intensity that the ion is exposed to. Depending on the ionic temperature and the degree of electric field compensation, it can be estimated that this scattering rate and consequently the heating rate is roughly an order of magnitude lower than for the "red" detuned case. Thus, ion heating rates below  $1 \text{ mK/s}$  seem reasonable and can be counteracted easily by collisional cooling with ultracold atoms. In the described scenario, the atoms experience a very deep potential of about  $200 \mu\text{K} \cdot k_{\text{B}}$  and would be tightly confined at trapping frequencies of about  $1 \text{ kHz}$ . Depending on the type of experiment to be performed, this may be advantageous or detrimental. If the detuning of the dipole trap with respect to the ionic transition frequency is reduced, tight ion trapping can be maintained while atom trapping is relaxed. A more detailed analysis should be done to determine an ideal configuration for specific experimental investigations. More details on possible optical trapping schemes can be found in the master's thesis by A. Krückow which extensively covers the topic of optical ion trapping in our setup [140].

### 7.3 An ideal choice of species

In order to reach novel regimes of atom-ion interaction in future experiments, the atomic and ionic species used should be considered very carefully. While the combination  $\text{Ba}^+ \text{-} \text{Rb}$  has shown a very rich and intriguing variety of interactions, it seems fairly unsuited for the envisaged ultracold and controlled atom-ion interactions (somewhat similar arguments also apply to  $\text{Rb}^+ \text{-} \text{Rb}$  which additionally suffers from the missing laser control of  $\text{Rb}^+$ ). This is partially due to the fact that the configuration  $\text{Ba}^+ + \text{Rb}$  is energetically unstable since the charge transfer reaction to  $\text{Rb}^+ + \text{Ba}$  is exothermic. While Feshbach control of this radiative decay may be achievable in future experiments (see section 1.3.2), this will ultimately be linked to simultaneous variations of the elastic interaction properties hampering the controlled engineering

of desired physical systems. Experimentally, the presence of the spontaneous decay channel of  $\text{Ba}^+$  not only requires a corresponding post-selection of interaction events but also makes frequent reloading of the ion trap necessary. This is time-consuming and detrimental, e.g. for local vacuum conditions or general experimental stability. In order to energetically close the described spontaneous decay channel, the initially ionized atomic species must feature a lower ionization energy than the neutral atoms it collides with. If we additionally constrain ourselves to species that have been trapped and laser cooled in standard lab setups, only about a dozen combinations remain. These include  $\text{Ba}^+ \text{-Ca}$ ,  $\text{Ba}^+ \text{-Li}$ ,  $\text{Sr}^+ \text{-Ca}$  or  $\text{Ca}^+ \text{-Yb}$ . The  $\text{Ba}^+ \text{-Ca}$  system has very recently been implemented experimentally in a combined magneto-optical and Paul trap [143].

It is generally difficult to realize atom-ion collision energies on the nK scale, even in the previously described optical trap for both species. Thus, an obvious question is which combination of species features s-wave interactions and therefore Feshbach control at realistic collision energies. Recapitulating formulas 1.3 and 1.4 we obtain for the characteristic energy

$$E^* = \frac{\hbar^4}{2\mu^2 C_4}, \quad (7.4)$$

where  $\mu$  is the reduced mass of the atom-ion system. Thus, light atomic species with small polarizabilities will yield the highest s-wave energies. Inspecting the possible combinations of species with energetically closed charge transfer channels,  $\text{Ba}^+ \text{-Li}$  turns out to clearly feature the highest s-wave energies. For fermionic  ${}^6\text{Li}$  we get  $E^* \approx 10 \mu\text{K} \cdot k_{\text{B}}$  which is about a factor of 200 higher than in the case of  $\text{Ba}^+ \text{-Rb}$ . An additional advantage of the  $\text{Ba}^+ \text{-Li}$  system is the large mass imbalance with a heavy ion and a light atom so that micromotion-induced heating mechanisms are maximally suppressed [19, 20, 35]. Thus, s-wave interactions may even be observable in a well-compensated Paul trap. Further, interatomic interactions in the Li gas can be precisely tuned by using a broad Feshbach resonance. This may be of great value as interatomic interactions can then effectively be switched off and the atoms can only interact with the ion. Additional usage of interspecies atom-ion Feshbach resonances may further increase the tunability of the system. In total,  $\text{Ba}^+ \text{-Li}$  may therefore offer the experimental tools to control those interactions that have been discovered and investigated in the  $\text{Ba}^+ \text{-Rb}$  system, thereby expanding the experimental terrain of atom-ion physics.

# Bibliography

- [1] F. Diedrich, J. C. Bergquist, W. M. Itano, and D. J. Wineland, “Laser Cooling to the Zero-Point Energy of Motion,” *Phys. Rev. Lett.*, vol. 62, pp. 403–406, Jan 1989.
- [2] J. I. Cirac and P. Zoller, “Quantum Computations with Cold Trapped Ions,” *Phys. Rev. Lett.*, vol. 74, pp. 4091–4094, May 1995.
- [3] F. Schmidt-Kaler, H. Häffner, M. Riebe, S. Gulde, G. P. T. Lancaster, T. Deuschle, C. Becher, C. F. Roos, J. Eschner, and R. Blatt, “Realization of the Cirac-Zoller controlled-NOT quantum gate,” *Nature*, vol. 422, p. 408, 2003.
- [4] T. Rosenband, D. B. Hume, P. O. Schmidt, C. W. Chou, A. Brusch, L. Lorini, W. H. Oskay, R. E. Drullinger, T. M. Fortier, J. E. Stalnaker, S. A. Didams, W. C. Swann, N. R. Newbury, W. M. Itano, D. J. Wineland, and J. C. Bergquist, “Frequency Ratio of  $\text{Al}^+$  and  $\text{Hg}^+$  Single-Ion Optical Clocks; Metrology at the 17th Decimal Place,” *Science*, vol. 319, no. 5871, pp. 1808–1812, 2008.
- [5] R. Blatt and C. F. Roos, “Quantum simulations with trapped ions,” *Nature Physics*, vol. 8, p. 277284, 2012.
- [6] M. H. Anderson, J. R. Ensher, M. R. Matthews, C. E. Wieman, and E. A. Cornell, “Observation of Bose-Einstein Condensation in a Dilute Atomic Vapor,” *Science*, vol. 269, no. 5221, pp. 198–201, 1995.
- [7] K. B. Davis, M. O. Mewes, M. R. Andrews, N. J. van Druten, D. S. Durfee, D. M. Kurn, and W. Ketterle, “Bose-Einstein Condensation in a Gas of Sodium Atoms,” *Phys. Rev. Lett.*, vol. 75, pp. 3969–3973, Nov 1995.

- [8] S. Inouye, M. R. Andrews, J. Stenger, H.-J. Miesner, D. M. Stamper-Kurn, and W. Ketterle, “Observation of Feshbach resonances in a Bose-Einstein condensate,” *Nature*, vol. 392, p. 151, 1998.
- [9] M. Greiner, O. Mandel, T. Esslinger, T. W. Hänsch, and I. Bloch, “Quantum phase transition from a superfluid to a Mott insulator in a gas of ultracold atoms,” *Nature*, vol. 415, p. 39, 2002.
- [10] P. Langevin, “Une formule fondamentale de théorie cinétique,” 1905.
- [11] R. Côté and A. Dalgarno, “Ultracold atom-ion collisions,” *Phys. Rev. A*, vol. 62, p. 012709, 2000.
- [12] R. Côté, “From Classical Mobility to Hopping Conductivity: Charge Hopping in an Ultracold Gas,” *Phys. Rev. Lett.*, vol. 85, p. 5316, 2000.
- [13] R. Côté, V. Kharchenko, and M. D. Lukin, “Mesoscopic Molecular Ions in Bose-Einstein Condensates,” *Phys. Rev. Lett.*, vol. 89, p. 093001, 2002.
- [14] A. T. Grier, M. Cetina, F. Oručević, and V. Vuletić, “Observation of Cold Collisions between Trapped Ions and Trapped Atoms,” *Phys. Rev. Lett.*, vol. 102, p. 223201, 2009.
- [15] C. Zipkes, S. Palzer, C. Sias, and M. Köhl, “A trapped single ion inside a Bose-Einstein condensate,” *Nature*, vol. 464, pp. 388–391, 2010.
- [16] S. Schmid, A. Härter, and J. Hecker Denschlag, “Dynamics of a Cold Trapped Ion in a Bose-Einstein Condensate,” *Phys. Rev. Lett.*, vol. 105, p. 133202, Sep 2010.
- [17] C. Zipkes, S. Palzer, L. Ratschbacher, C. Sias, and M. Köhl, “Cold heteronuclear atom-ion collisions,” *Phys. Rev. Lett.*, vol. 105, p. 12559, 2010.
- [18] F. G. Major and H. G. Dehmelt, “Exchange-collision technique for the rf spectroscopy of stored ions,” *Phys. Rev.*, vol. 170, p. 91, 1968.
- [19] R. DeVoe, “Power-law distributions for a trapped ion interacting with a classical buffer gas,” *Phys. Rev. Lett.*, vol. 102, p. 063001, 2009.
- [20] C. Zipkes, L. Ratschbacher, C. Sias, and M. Köhl, “Kinetics of a single trapped ion in an ultracold buffer gas,” *New. J. Phys.*, vol. 13, p. 053020, 2011.

- [21] F. H. J. Hall, M. Aymar, N. Bouloufa-Maafa, O. Dulieu, and S. Willitsch, “Light-Assisted Ion-Neutral Reactive Processes in the Cold Regime: Radiative Molecule Formation versus Charge Exchange,” *Phys. Rev. Lett.*, vol. 107, p. 243202, Dec 2011.
- [22] F. H. J. Hall and S. Willitsch, “Millikelvin Reactive Collisions between Sympathetically Cooled Molecular Ions and Laser-Cooled Atoms in an Ion-Atom Hybrid Trap,” *Phys. Rev. Lett.*, vol. 109, p. 233202, Dec 2012.
- [23] S. T. Sullivan, W. G. Rellergert, S. Kotochigova, K. Chen, S. J. Schowalter, and E. R. Hudson, “Trapping molecular ions formed via photo-associative ionization of ultracold atoms,” *Phys. Chem. Chem. Phys.*, vol. 13, pp. 18859–18863, 2011.
- [24] W. G. Rellergert, S. T. Sullivan, S. Kotochigova, A. Petrov, K. Chen, S. J. Schowalter, and E. R. Hudson, “Measurement of a Large Chemical Reaction Rate between Ultracold Closed-Shell  $^{40}\text{Ca}$  Atoms and Open-Shell  $^{174}\text{Yb}^+$  Ions Held in a Hybrid Atom-Ion Trap,” *Phys. Rev. Lett.*, vol. 107, p. 243201, Dec 2011.
- [25] L. Ratschbacher, C. Zipkes, C. Sias, and M. Köhl, “Controlling chemical reactions of a single particle,” *Nat. Phys.*, vol. 8, p. 649, 2012.
- [26] [www.alternativroute.de](http://www.alternativroute.de).
- [27] P. Zhang, A. Dalgarno, and R. Côté, “Scattering of Yb and  $\text{Yb}^+$ ,” *Phys. Rev. A*, vol. 80, p. 030703, Sep 2009.
- [28] M. Krych, W. Skomorowski, F. Pawłowski, R. Moszynski, and Z. Idziaszek, “Sympathetic cooling of the  $\text{Ba}^+$  ion by collisions with ultracold Rb atoms: Theoretical prospects,” *Phys. Rev. A*, vol. 83, p. 032723, Mar 2011.
- [29] P. K. Gosh, *Ion traps*. Clarendon Press, 1995.
- [30] D. Wineland, C. Monroe, W. Itano, D. Leibfried, B. King, and D. Meekhof, “Experimental Issues in Coherent Quantum-State Manipulation of Trapped Atomic Ions,” *J. Res. Natl. Inst. Stand. Technol.*, vol. 103, p. 259, 1998.
- [31] D. Leibfried, R. Blatt, C. Monroe, and D. J. Wineland, “Quantum dynamics of single trapped ions,” *Rev. Mod. Phys.*, vol. 75, p. 281, 2003.

- [32] A. Härter, A. Krükow, A. Brunner, W. Schnitzler, S. Schmid, and J. Hecker Denschlag, “Single Ion as a Three-Body Reaction Center in an Ultracold Atomic Gas,” *Phys. Rev. Lett.*, vol. 109, p. 123201, Sep 2012.
- [33] D. Hucul, M. Yeo, S. Olmschenk, C. Monroe, W. K. Hensinger, and J. Rabchuk, “On the transport of atomic ions in linear and multidimensional ion trap arrays,” *Quantum Info. Comput.*, vol. 8, pp. 501–578, July 2008.
- [34] C. Monroe, D. M. Meekhof, B. E. King, S. R. Jefferts, W. M. Itano, D. J. Wineland, and P. Gould, “Resolved-Sideband Raman Cooling of a Bound Atom to the 3D Zero-Point Energy,” *Phys. Rev. Lett.*, vol. 75, pp. 4011–4014, Nov 1995.
- [35] M. Cetina, A. T. Grier, and V. Vuletić, “Micromotion-Induced Limit to Atom-Ion Sympathetic Cooling in Paul Traps,” *Phys. Rev. Lett.*, vol. 109, p. 253201, Dec 2012.
- [36] D. Smith, “The ion chemistry of interstellar clouds,” *Chemical Reviews*, vol. 92, no. 7, pp. 1473–1485, 1992.
- [37] D. Gerlich and S. Horning, “Experimental investigation of radiative association processes as related to interstellar chemistry,” *Chemical Reviews*, vol. 92, no. 7, pp. 1509–1539, 1992.
- [38] D. Gerlich, E. Herbst, and E. Roueff, “ $H_3^+ + HD \rightarrow H_2D^+ + H_2$ : low-temperature laboratory measurements and interstellar implications,” *Planetary and Space Science*, vol. 50, no. 1213, pp. 1275 – 1285, 2002. Special issue on Deuterium in the Universe.
- [39] Z. Idziaszek, T. Calarco, P. S. Julienne, and A. Simoni, “Quantum theory of ultracold atom-ion collisions,” *Phys. Rev. A*, vol. 79, p. 010702, 2009.
- [40] Z. Idziaszek, A. Simoni, T. Calarco, and P. S. Julienne, “Multichannel quantum-defect theory for ultracold atom-ion collisions,” *New Journal of Physics*, vol. 13, no. 8, p. 083005, 2011.
- [41] Z. Idziaszek, *private communication*.
- [42] A. Alexandrov and J. Devreese, “Advances in polaron physics,” *Springer Verlag Springer Series on Solid State Sciences*, vol. 159, 2009.

- [43] A. Schirotzek, C.-H. Wu, A. Sommer, and M. W. Zwierlein, “Observation of Fermi Polarons in a Tunable Fermi Liquid of Ultracold Atoms,” *Phys. Rev. Lett.*, vol. 102, p. 230402, Jun 2009.
- [44] C. Kohstall, M. Zaccanti, M. Jag, A. Trenkwalder, P. Massignan, G. Bruun, F. Schreck, and R. Grimm, “Metastability and coherence of repulsive polarons in a strongly interacting Fermi mixture,” *Nature*, vol. 485, p. 615, 2012.
- [45] M. Koschorreck, D. Pertot, E. Vogt, B. Fröhlich, M. Feld, and M. Köhl, “Attractive and repulsive Fermi polarons in two dimensions,” *Nature*, vol. 485, p. 619, 2012.
- [46] F. M. Cuccietti and E. Timmermans, “Strong-Coupling Polarons in Dilute Gas Bose-Einstein Condensates,” *Phys. Rev. Lett.*, vol. 96, p. 210401, 2006.
- [47] R. M. Kalas and D. Blume, “Interaction-induced localization of an impurity in a trapped Bose-Einstein condensate,” *Phys. Rev. A*, vol. 73, p. 043608, Apr 2006.
- [48] J. Tempere, W. Casteels, M. K. Oberthaler, S. Knoop, E. Timmermans, and J. T. Devreese, “Feynman path-integral treatment of the BEC-impurity polaron,” *Phys. Rev. B*, vol. 80, p. 184504, Nov 2009.
- [49] W. Casteels, T. Cauteren, J. Tempere, and J. Devreese, “Strong coupling treatment of the polaronic system consisting of an impurity in a condensate,” *Laser Physics*, vol. 21, pp. 1480–1485, 2011.
- [50] Z. Idziaszek, T. Calarco, and P. Zoller, “Controlled collisions of a single atom and an ion guided by movable trapping potentials,” *Phys. Rev. A*, vol. 76, p. 033409, Sep 2007.
- [51] H. Doerk, Z. Idziaszek, and T. Calarco, “Atom-ion quantum gate,” *Phys. Rev. A*, vol. 81, p. 012708, Jan 2010.
- [52] L. H. Nguyêñ, A. Kalev, M. D. Barrett, and B.-G. Englert, “Micromotion in trapped atom-ion systems,” *Phys. Rev. A*, vol. 85, p. 052718, May 2012.
- [53] “Nature Insight on Ultracold Matter,” *Nature*, vol. 416, pp. 205–246, 2002.
- [54] M. Hawley and M. A. Smith, “Gas phase collisional quenching of NO<sup>+</sup>(v=1) ions below 5 K,” *The Journal of Chemical Physics*, vol. 95, no. 11, pp. 8662–8664, 1991.

- [55] D. Gerlich, “Probing the structure of  $\text{CH}_5^+$  ions and deuterated variants via collisions,” *Phys. Chem. Chem. Phys.*, vol. 7, pp. 1583–1591, 2005.
- [56] R. Otto, J. Mikosch, S. Trippel, M. Weidemüller, and R. Wester, “Nonstandard behavior of a negative ion reaction at very low temperatures,” *Phys. Rev. Lett.*, vol. 101, p. 063201, Aug 2008.
- [57] S. Willitsch, M. T. Bell, A. D. Gingell, S. R. Procter, and T. P. Softley, “Cold Reactive Collisions between Laser-Cooled Ions and Velocity-Selected Neutral Molecules,” *Phys. Rev. Lett.*, vol. 100, p. 043203, 2008.
- [58] M. Cetina, A. Grier, J. Campbell, I. Chuang, and V. Vuletić, “Bright source of cold ions for surface-electrode traps,” *Phys. Rev. A*, vol. 76, p. 041401, 2007.
- [59] K. Ravi, S. Lee, A. Sharma, G. Werth, and S. A. Rangwala, “Cooling and stabilization by collisions in a mixed ion-atom system,” *Nat. Comm.*, vol. 3, p. 1126, 2012.
- [60] M. Weidemüller and R. Wester, *private communication*.
- [61] C. Zipkes, L. Ratschbacher, S. Palzer, C. Sias, and M. Köhl, “Hybrid quantum systems of atoms and ions,” *J. Phys.: Conf. Ser.*, vol. 264, p. 012019, 2011.
- [62] P. F. Staanum, K. Hojbjerre, P. Skyt, A. Hansen, and M. Drewsen, “Rotational laser cooling of vibrationally and translationally cold molecular ions,” *Nat. Phys.*, vol. 6, p. 271, 2010.
- [63] T. Schneider, B. Roth, H. Duncker, I. Ernsting, and S. Schiller, “All-optical preparation of molecular ions in the rovibrational ground state,” *Nat. Phys.*, vol. 6, p. 275, 2010.
- [64] P. Massignan, C. J. Pethick, and H. Smith, “Static properties of positive ions in atomic Bose-Einstein condensates,” *Phys. Rev. A*, vol. 71, p. 023606, 2005.
- [65] Varian StarCell 751/s.
- [66] Varian UHV-24p.
- [67] Sigma-Aldrich Part-No 276332-1G.
- [68] Titanium Sublimation pump TSP (filament type) from Varian.

- [69] T. Esslinger, I. Bloch, and T. W. Hänsch, “Bose-Einstein condensation in a quadrupole-Ioffe-configuration trap,” *Phys. Rev. A*, vol. 58, pp. R2664–R2667, Oct 1998.
- [70] CEM-4823G from Burle.
- [71] M. G. Raizen, J. M. Gilligan, J. C. Bergquist, W. M. Itano, and D. J. Wineland, “Ionic crystals in a linear Paul trap,” *Phys. Rev. A*, vol. 45, pp. 6493–6501, May 1992.
- [72] Agilent 33220A.
- [73] Minicircuits ZHL-5W-1.
- [74] D. J. Berkeland, J. D. Miller, J. C. Bergquist, W. M. Itano, and D. J. Wineland, “Minimization of ion micromotion in a Paul trap,” *J. Appl. Phys.*, vol. 83, p. 10, 1998.
- [75] Alvasource from the company Alvatec.
- [76] DL-100 from Toptica.
- [77] R. W. P. Drever, J. L. Hall, F. V. Kowalski, J. Hough, G. M. Ford, A. J. Munley, and H. Ward, “Laser Phase and Frequency Stabilization Using an Optical Resonator,” *Appl. Phys. B*, vol. 31, pp. 97–105, 1983.
- [78] E. D. Black, “An introduction to Pound-Drever-Hall laser frequency stabilization,” *Am. J. Phys.*, vol. 69, p. 79, 2001.
- [79] D. J. McCarron, S. A. King, and S. L. Cornish, “Modulation transfer spectroscopy in atomic rubidium,” *Meas. Sci. Technol.*, vol. 19, p. 105601, 2008.
- [80] BoosTA from Toptica.
- [81] G. C. Bjorklund, M. D. Levenson, W. Lenth, and C. Ortiz, “Frequency Modulation (FM) spectroscopy,” *Meas. Sci. Technol.*, vol. 32, pp. 145–152, 1983.
- [82] M. Greiner, I. Bloch, T. W. Hänsch, and T. Esslinger, “Magnetic transport of trapped cold atoms over a large distance,” *Phys. Rev. A*, vol. 63, p. 031401, 2001.

- [83] M. Theis, G. Thalhammer, K. Winkler, M. Hellwig, G. Ruff, R. Grimm, and J. Hecker Denschlag, “Tuning the Scattering Length with an Optically Induced Feshbach Resonance,” *Phys. Rev. Lett.*, vol. 93, p. 123001, Sep 2004.
- [84] S. Schmid, G. Thalhammer, K. Winkler, F. Lang, and J. Hecker Denschlag, “Long distance transport of ultracold atoms using a 1D optical lattice,” *New. J. Phys.*, vol. 8, p. 159, 2006.
- [85] Mephisto from the company Innolight.
- [86] This is in fact the main reason for the vacuum chamber layout where the position of the science chamber is located above the BEC chamber. A horizontal transfer into the science chamber would have been plagued with compensating the gravitational force to prevent atomic losses.
- [87] C. Chin, R. Grimm, P. S. Julienne, and E. Tiesinga, “Feshbach resonances in ultracold gases,” *Rev. Mod. Phys.*, vol. 82, p. 1225, 2010.
- [88] R. Teachout and R. Pack, “Table of experimental and calculated static dipole polarizabilities for the electronic ground states of the neutral elements (in atomic units),” *Atomic Data*, vol. 3, p. 195, 1972.
- [89] G. Thalhammer, M. Theis, K. Winkler, R. Grimm, and J. Hecker Denschlag, “Inducing an optical Feshbach resonance via stimulated Raman coupling,” *Phys. Rev. A*, vol. 71, p. 033403, Mar 2005.
- [90] O. P. Makarov, R. Côté, and W. W. Smith, “Radiative charge-transfer lifetime of the excited state of  $(\text{NaCa})^+$ ,” *Phys. Rev. A*, vol. 67, p. 042705, 2003.
- [91] A. Brunner, “Excess Micromotion in Atom-Ionen-Experimenten,” Master’s thesis, Universität Ulm, 2012.
- [92] K. Singer, U. Poschinger, M. Murphy, P. Ivanov, F. Ziesel, T. Calarco, and F. Schmidt-Kaler, “Colloquium : Trapped ions as quantum bits: Essential numerical tools,” *Rev. Mod. Phys.*, vol. 82, pp. 2609–2632, Sep 2010.
- [93] S. Schmid, *Dynamics of a cold trapped ion in a Bose-Einstein condensate*. PhD thesis, Universität Ulm, 2012.
- [94] L. Deslauriers, S. Olmschenk, D. Stick, W. K. Hensinger, J. Sterk, and C. Monroe, “Scaling and Suppression of Anomalous Heating in Ion Traps,” *Phys. Rev. Lett.*, vol. 97, p. 103007, Sep 2006.

- [95] K. M. O'Hara, M. E. Gehm, S. R. Granade, and J. E. Thomas, "Scaling laws for evaporative cooling in time-dependent optical traps," *Phys. Rev. A*, vol. 64, p. 051403, Oct 2001.
- [96] S. Narayanan, N. Daniilidis, S. A. Möller, R. Clark, F. Ziesel, K. Singer, F. Schmidt-Kaler, and H. Häffner, "Electric field compensation and sensing with a single ion in a planar trap," *Journal of Applied Physics*, vol. 110, no. 11, p. 114909, 2011.
- [97] U. Tanaka, K. Masuda, Y. Akimoto, K. Koda, Y. Ibaraki, and S. Urabe, "Micromotion compensation in a surface electrode trap by parametric excitation of trapped ions," *Applied Physics B*, vol. 107, pp. 907–912, 2012.
- [98] K. Pyka, N. Herschbach, J. Keller, and T. Mehlstäubler, "A high-precision rf trap with minimized micromotion for an  $In^+$  multiple-ion clock," *arXiv:1206.5111*, Jun 2012.
- [99] M. Chwalla, *Precision spectroscopy with  $^{40}Ca^+$  ions in a Paul trap*. PhD thesis, Universität Innsbruck, 2009.
- [100] B. Hemmerling, *Towards Direct Frequency Comb Spectroscopy Using Quantum Logic*. PhD thesis, Gottfried Wilhelm Leibniz Universität Hannover, 2011.
- [101] Q. A. Turchette, Kielpinski, B. E. King, D. Leibfried, D. M. Meekhof, C. J. Myatt, M. A. Rowe, C. A. Sackett, C. S. Wood, W. M. Itano, C. Monroe, and D. J. Wineland, "Heating of trapped ions from the quantum ground state," *Phys. Rev. A*, vol. 61, p. 063418, May 2000.
- [102] J. Labaziewicz, Y. Ge, D. R. Leibrandt, S. X. Wang, R. Shewmon, and I. L. Chuang, "Temperature Dependence of Electric Field Noise above Gold Surfaces," *Phys. Rev. Lett.*, vol. 101, p. 180602, Oct 2008.
- [103] D. T. C. Allcock, L. Guidoni, T. P. Harty, C. J. Ballance, M. G. Blain, A. M. Steane, and D. M. Lucas, "Reduction of heating rate in a microfabricated ion trap by pulsed-laser cleaning," *New Journal of Physics*, vol. 13, no. 12, p. 123023, 2011.
- [104] D. A. Hite, Y. Colombe, A. C. Wilson, K. R. Brown, U. Warring, R. Jördens, J. D. Jost, K. S. McKay, D. P. Pappas, D. Leibfried, and D. J. Wineland,

“100-Fold Reduction of Electric-Field Noise in an Ion Trap Cleaned with *In-Situ* Argon-Ion-Beam Bombardment,” *Phys. Rev. Lett.*, vol. 109, p. 103001, Sep 2012.

- [105] “<http://www.quantum.gatech.edu/heatingData.shtml>.”
- [106] H. F. Hess, D. A. Bell, G. P. Kochanski, R. W. Cline, D. Kleppner, and T. J. Greytak, “Observation of Three-Body Recombination in Spin-Polarized Hydrogen,” *Phys. Rev. Lett.*, vol. 51, pp. 483–486, Aug 1983.
- [107] B. D. Esry, C. H. Greene, and J. P. Burke, “Recombination of Three Atoms in the Ultracold Limit,” *Phys. Rev. Lett.*, vol. 83, pp. 1751–1754, Aug 1999.
- [108] E. A. Burt, R. W. Ghrist, C. J. Myatt, M. J. Holland, E. A. Cornell, and C. E. Wieman, “Coherence, Correlations, and Collisions: What One Learns about Bose-Einstein Condensates from Their Decay,” *Phys. Rev. Lett.*, vol. 79, pp. 337–340, Jul 1997.
- [109] N. Spethmann, F. Kindermann, S. John, C. Weber, D. Meschede, and A. Widera, “Dynamics of Single Neutral Impurity Atoms Immersed in an Ultracold Gas,” *Phys. Rev. Lett.*, vol. 109, p. 235301, Dec 2012.
- [110] S. Schmid, A. Härtter, A. Frisch, S. Hoinka, and J. Hecker Denschlag, “An apparatus for immersing trapped ions into an ultracold gas of neutral atoms,” *Rev. Sci. Instrum.*, vol. 83, p. 053108, 2012.
- [111] to be published.
- [112] Due to the non-thermal energy distribution of the ion immersed in the atom cloud we use the median as an energy measure.
- [113] J. Söding, D. Guéry-Odelin, P. Desbiolles, F. Chevy, H. Inamori, and J. Dalibard, “Three-body decay of a Rubidium Bose-Einstein condensate,” *Applied Physics B*, vol. 69, pp. 257–261, 1999.
- [114] H. Suno and B. D. Esry, “Three-body recombination in cold helium-helium-alkali-metal-atom collisions,” *Phys. Rev. A*, vol. 80, p. 062702, Dec 2009.
- [115] Y. Wang, J. P. D’Incao, and B. D. Esry, “Cold three-body collisions in hydrogen-hydrogen-alkali-metal atomic systems,” *Phys. Rev. A*, vol. 83, p. 032703, Mar 2011.

- [116] N. L. Guevara, Y. Wang, and B. D. Esry, “New Class of Three-Body States,” *Phys. Rev. Lett.*, vol. 108, p. 213202, May 2012.
- [117] P. O. Fedichev, M. W. Reynolds, and G. V. Shlyapnikov, “Three-body recombination of ultracold atoms to a weakly bound  $s$  level,” *Phys. Rev. Lett.*, vol. 77, pp. 2921–2924, Sep 1996.
- [118] P. F. Bedaque, E. Braaten, and H.-W. Hammer, “Three-body recombination in Bose gases with large scattering length,” *Phys. Rev. Lett.*, vol. 85, pp. 908–911, Jul 2000.
- [119] V. Efimov, “Energy levels arising from resonant two-body forces in a three-body system,” *Physics Letters B*, vol. 33, no. 8, pp. 563 – 564, 1970.
- [120] E. Braaten and H.-W. Hammer, “Three-body recombination into deep bound states in a Bose gas with large scattering length,” *Phys. Rev. Lett.*, vol. 87, p. 160407, Oct 2001.
- [121] T. Kraemer, M. Mark, P. Waldburger, J. Danzl, C. Chin, B. Engeser, A. Lange, K. Pilch, A. Jaakkola, H.-C. Nägerl, and R. Grimm, “Evidence for Efimov quantum states in an ultracold gas of caesium atoms,” *Nature*, vol. 440, pp. 315–318, 2006.
- [122] D. R. Bates, A. E. Kingston, and R. W. P. McWhirter, “Recombination between electrons and atomic ions. I. Optically thin plasmas,” *Proceedings of the Royal Society of London. Series A. Mathematical and Physical Sciences*, vol. 267, no. 1330, pp. 297–312, 1962.
- [123] D. R. Flower and G. J. Harris, “Three-body recombination of hydrogen during primordial star formation,” *Monthly Notices of the Royal Astronomical Society*, vol. 377, no. 2, pp. 705–710, 2007.
- [124] J. Lozeille, A. Fioretti, C. Gabbanini, Y. Huang, H. K. Pechkis, D. Wang, P. L. Gould, E. E. Eyler, W. C. Stwalley, M. Aymar, and O. Dulieu, “Detection by two-photon ionization and magnetic trapping of cold  $\text{Rb}_2$  triplet state molecules,” *Eur. Phys. J. D*, vol. 39, pp. 261–269, 2006.
- [125] M. Aymar, S. Azizi, and O. Dulieu, “Model-potential calculations for ground and excited  $\Sigma$  states of  $\text{Rb}_2^+$ ,  $\text{Cs}_2^+$  and  $\text{RbCs}^+$  ions,” *J. Phys. B: At. Mol. Opt. Phys.*, vol. 36, p. 4799, 2003.

- [126] A. Fioretti, D. Comparat, A. Crubellier, O. Dulieu, F. Masnou-Seeuws, and P. Pillet, “Formation of Cold  $\text{Cs}_2$  Molecules through Photoassociation,” *Phys. Rev. Lett.*, vol. 80, pp. 4402–4405, May 1998.
- [127] Y. Huang, J. Qi, H. K. Pechkis, D. Wang, E. E. Eyler, P. L. Gould, and W. C. Stwalley, “Formation, detection and spectroscopy of ultracold  $\text{Rb}_2$  in the ground  $\text{X}^1\Sigma_g^+$  state,” *Journal of Physics B: Atomic, Molecular and Optical Physics*, vol. 39, no. 19, p. S857, 2006.
- [128] W. Salzmann, T. Mullins, J. Eng, M. Albert, R. Wester, M. Weidmüller, A. Merli, S. M. Weber, F. Sauer, M. Plewicki, F. Weise, L. Wöste, and A. Lindinger, “Coherent transients in the femtosecond photoassociation of ultracold molecules,” *Phys. Rev. Lett.*, vol. 100, p. 233003, Jun 2008.
- [129] M. Mudrich, P. Heister, T. Hippler, C. Giese, O. Dulieu, and F. Stienkemeier, “Spectroscopy of triplet states of  $\text{Rb}_2$  by femtosecond pump-probe photoionization of doped helium nanodroplets,” *Phys. Rev. A*, vol. 80, p. 042512, Oct 2009.
- [130] C. Strauss, T. Takekoshi, F. Lang, K. Winkler, R. Grimm, J. Hecker Denschlag, and E. Tiemann, “Hyperfine, rotational, and vibrational structure of the  $a^3\Sigma_u^+$  state of  $^{87}\text{Rb}_2$ ,” *Phys. Rev. A*, vol. 82, p. 052514, Nov 2010.
- [131] T. Takekoshi, C. Strauss, F. Lang, J. H. Denschlag, M. Lysebo, and L. Veseth, “Hyperfine, rotational, and Zeeman structure of the lowest vibrational levels of the  $^{87}\text{Rb}_2$  (1)  $^3\Sigma_g^+$  state,” *Phys. Rev. A*, vol. 83, p. 062504, Jun 2011.
- [132] A. Drozdova. PhD thesis, Université de Lyon and Lomonosov State University, 2012.
- [133] to be published.
- [134] T. P. Dinneen, C. D. Wallace, K.-Y. N. Tan, and P. L. Gould, “Use of trapped atoms to measure absolute photoionization cross sections,” *Opt. Lett.*, vol. 17, pp. 1706–1708, Dec 1992.
- [135] C. Gabbanini, S. Gozzini, and A. Lucchesini, “Photoionization cross section measurement in a Rb vapor cell trap,” *Optics Communications*, vol. 141, no. 12, pp. 25 – 28, 1997.

- [136] D. Ciampini, M. Anderlini, J. H. Müller, F. Fuso, O. Morsch, J. W. Thomsen, and E. Arimondo, “Photoionization of ultracold and Bose-Einstein-condensed Rb atoms,” *Phys. Rev. A*, vol. 66, p. 043409, Oct 2002.
- [137] G. Morigi and H. Walther, “Two-species Coulomb chains for quantum information,” *Eur. Phys. J. D*, vol. 13, pp. 261–269, 2001.
- [138] R. Grimm, M. Weidemüller, and Y. Ovchinnikov, “Optical dipole traps for neutral atoms,” *Adv. At. Mol. Opt. Phys.*, vol. 42, p. 95, 2000.
- [139] C. Schneider, M. Enderlein, T. Huber, and T. Schätz, “Optical trapping of an ion,” *Nat. Photonics*, vol. 4, p. 772, Oct 2010.
- [140] A. Krükow, “Verbesserte und neuartige Fallenkonfigurationen im BaRbI-Experiment,” Master’s thesis, Universität Ulm, 2011.
- [141] T. Kuga, Y. Torii, N. Shiokawa, T. Hirano, Y. Shimizu, and H. Sasada, “Novel Optical Trap of Atoms with a Doughnut Beam,” *Phys. Rev. Lett.*, vol. 78, pp. 4713–4716, Jun 1997.
- [142] A. Mawardi, S. Hild, A. Widera, and D. Meschede, “ABCD-treatment of a propagating doughnut beam generated by a spiral phase plate,” *Opt. Express*, vol. 19, pp. 21205–21210, Oct 2011.
- [143] S. Sullivan, W. Rellergert, S. Kotochigova, and E. Hudson, “The role of electronic excitation in cold atom-ion chemistry,” *arXiv:1205.4286*, 2012.

## **Erklärung**

Ich versichere hiermit, dass ich die Arbeit selbständig angefertigt habe und keine anderen als die angegebenen Quellen und Hilfsmittel benutzt sowie die wörtlich oder inhaltlich übernommenen Stellen als solche kenntlich gemacht habe.

Ulm, den

.....  
Vorname Nachname / Unterschrift



# **Erklärung über individuellen Beitrag zur Dissertation**

Teile dieser kumulativen Dissertation sind in Ko-Autorenschaft mit anderen Wissenschaftlern entstanden. Dies bezieht sich auf die Kapitel 2,3,5 und 6, die deckungsgleich mit den an entsprechender Stelle aufgeführten wissenschaftlichen Publikationen sind.

- Kapitel 2: Ich habe in wesentlichem Maße zum Aufbau der beschriebenen wissenschaftlichen Apparatur in enger Kooperation mit dem Hauptautor, Stefan Schmid, beigetragen. Ich war bei der Ausarbeitung der Messmethoden sowie der Aufnahme der gezeigten Messdaten in wesentlichem Maße beteiligt und habe beim Schreiben der Publikation assistiert.
- Kapitel 3: Ich war bei der Ausarbeitung der Messmethoden sowie der Aufnahme der gezeigten Messdaten in wesentlichem Maße beteiligt, habe Teile der Datenanalyse durchgeführt und habe beim Schreiben der Publikation assistiert.
- Kapitel 5: Ich war bei der Ausarbeitung der Messmethoden sowie der Aufnahme der gezeigten Messdaten in hauptverantwortlichem Maße in enger Kooperation mit dem Zweitautor, Artjom Krükow, beteiligt. Ich habe große Teile der Datenanalyse durchgeführt und war hauptverantwortlich für das Schreiben der Publikation.
- Kapitel 6: Ich war bei der Ausarbeitung der Messmethoden sowie der Aufnahme der gezeigten Messdaten in hauptverantwortlichem Maße in enger Kooperation mit dem Zweitautor, Artjom Krükow, beteiligt. Ich habe Teile der Datenanalyse durchgeführt und war hauptverantwortlich für das Schreiben der Publikation.

Ulm, den .....

Vorname Nachname / Unterschrift

Bestätigung der Richtigkeit der Angaben durch den Betreuer der Dissertation:

Ulm, den .....

Vorname Nachname / Unterschrift



Der Inhalt dieser Seite wurde aus Gründen des Datenschutzes entfernt.



Der Inhalt dieser Seite wurde aus Gründen des Datenschutzes entfernt.